Hubertus Schlagheck

Collective Flow Phenomena in $33\,\mathrm{TeV}$ $\mathrm{Pb} + \mathrm{Pb}$ Reactions

— 1998 —

Experimentelle Physik

Collective Flow Phenomena in $33\,\mathrm{TeV}$ $\mathrm{Pb} + \mathrm{Pb}$ Reactions

Inaugural-Dissertation
zur Erlangung des Doktorgrades
der Naturwissenschaften im Fachbereich Physik
der Mathematisch-Naturwissenschaftlichen Fakultät
der Westfälischen Wilhelms-Universität Münster

vorgelegt von
Hubertus Schlagheck
aus Seppenrade

— 1998 —

Dekan:	Prof. Dr. N. Schmitz
Erster Gutachter:	Prof. Dr. R. Santo
Zweiter Gutachter:	Prof. Dr. D. Frekers
Tag der mündlichen Prüfung:	28.01. & 09.02.1999
Tag der Promotion:	09.02.1999

pantha rhei

Contents

1 Introduction 5

1.1 Quark Gluon Plasma 6

1.2 Collective Flow 8

2 The WA98 Experiment 11

2.1 Calorimeter 12

2.2 Charged Particle Tracking 12

2.2.1 First Tracking Arm 12

2.2.2 Second Tracking Arm 13

2.3 Multiplicity Detectors 13

2.3.1 Silicon Drift Detector 13

2.3.2 Silicon Pad Multiplicity Detector 14

2.3.3 Photon Multiplicity Detector 14

2.3.4 Charged Particle Veto 14

2.4 The Photon Spectrometer LEDA 15

2.4.1 Mode of Operation 15

2.4.2 Detector Design 15

2.5 The Plastic Ball Spectrometer 17

2.6 Trigger 19

3 Data Reduction 21

3.1 Event Classification 21

3.2 LEDA γ and π^0 Measurement 23

3.2.1 Calibration and Corrections 23

3.2.2 Photon Identification 24

3.2.3 π^0 Meson Reconstruction 25

3.3 Plastic Ball 26

3.3.1 Module Check . . . 26
3.3.2 Particle Identification . . . 27
3.3.3 Acceptance . . . 29

4 Azimuthal Event Shape 33
4.1 Reaction Plane Event by Event . . . 33
4.1.1 Sphericity Method . . . 34
4.1.2 Transverse Momentum Method . . . 35
4.1.3 Fourier Analysis Method . . . 35
4.2 Results . . . 36
4.2.1 Φ Distribution . . . 36
4.2.2 Subevent Analysis . . . 37
4.2.3 Dependence of χ on Centrality . . . 40
4.2.4 Reaction Plane Resolution . . . 42
4.2.5 Auto Correlation . . . 46

5 Average Transverse Momentum 47
5.1 Dependence of $\langle p_x \rangle$ on Rapidity . . . 49
5.2 Dependence of $\langle p_x \rangle$ on Centrality . . . 53
5.3 Dependence of $\langle p_x \rangle$ on Beam Energy . . . 54

6 Azimuthal Correlation Analysis 57
6.1 Dependence on Transverse Momentum . . . 58
6.2 Dependence on Rapidity . . . 64
6.3 Dependence on Centrality . . . 68
6.4 Comparison with the $\langle p_x \rangle$ Method . . . 71

7 Summary and Conclusions 75

A Kinematical Variables 79

B Plastic Ball Mapping 81

C Event Selection 83

D Plastic Ball Particle Identification 85
D.1 The Applied Cuts . . . 85

D.2 Influence of cuts on $\langle p_x \rangle$ 85
D.3 Linearization Method 85

E Background Contamination 87

F Photon Flow Cross Checks 89

Bibliography 91

Acknowledgements 99

1. Introduction

Particle physicists today believe that the standard model of elementary particles describes the fundamental building of matter along with their interactions. It comprises the theories of the electroweak and the strong interactions. The standard model includes two groups of elementary particles, leptons and quarks. The Leptons can only interact electroweak, i.e. by the unified electromagnetic and weak interaction. They are not subject to the strong force mediated by the gluons. The quarks, however, interact strongly, weakly, and electromagnetically. The three types of interactions included in the standard model are all mediated by the exchange of gauge bosons. The mediator of the electromagnetic force is the photon, those of the weak force are the $W^{\pm}$ and the Z^0, and the strong force is mediated by the gluons. While the photon carries no charge, and is therefore not subject to the electromagnetic force itself, the gluons actually carry colour charge and thus interact with each other. The gluons and the photons are presumably mass-less, but the $W^{\pm}$ and the Z^0 bosons are rather heavy. Therefore, the range of the weak interaction is very short, about 10^{-18}m. The strong interaction has a limited effective range of 10^{-15}m due to colour-screening effects.

Quarks

Experimentally, one has found evidence of six quarks they obey as fermions the Pauli principle, which caused difficulties when the Δ^{++} resonance was discovered. The Δ^{++} resonance is a particle consisting of three up quarks with parallel spins. This situation contradicts the Pauli principle. This problem could be solved by introducing the colour charge [Gel73]. The colour quantum number can take three basic values, i.e. *red*, *green*, and *blue* as well as the respective anti-colours. Since the three quarks in the Δ^{++} resonance have different colours, its wave function is anti-symmetric and therefore the Pauli principle is obeyed. When the quark concept was invented in the mid 1960s the physicists were able to categorize and describe most of the particles discovered in accelerator experiments.

The observed particles that are made out of quarks are called hadrons, strongly interacting particles. Hadrons consisting out of three quarks, such as the proton and the neutron, are named baryons, while mesons consist out of one quark and one anti-quark. Single free quarks can not be observed since the strength of the strong force increases with the distance of the interacting particles. Hence the quarks are confined inside the hadrons. Observable particles are therefore colour-neutral objects and the quarks forming this object must have a colour combination rendering a colour-less particle.

Gluons

The force that binds quarks together, the strong interaction, is mediated by its exchange particles, the gluons. The gluons carry both colour and anti-colour and since 3×3 combinations exist, they form two multiplets

of states, an octet and a singlet. It is possible to construct all colour states from the octet and therefore there are eight different gluons. The ninth state is the totally symmetric state ($r\bar{r} + g\bar{g} + b\bar{b}$), which is colour-less, and therefore plays no role in the strong interaction. Since gluons themselves carry colour they can interact with each other. This is the main difference between the strong and the electromagnetic interaction, since photons carry no electric charge. The strong interaction is flavour independent, i.e., all sorts of quarks have identical strong interactions.

One consequence of the properties of the strong force is that the strength of the force decreases when the quarks are close to each other. This property gives the quarks what is called the asymptotic freedom at small inter-quark distances. The interaction potential of two quarks can be described by:

$$V(r) = -\frac{4}{3}\frac{\alpha_s}{r} + kr$$

The coupling constant α_s has a direct dependence on the squared four-momentum transfer in the quark quark process [Won94]:

$$\alpha_s(Q) = \frac{12\,\pi}{(33 - 2N_f)\ln(Q^2/\Lambda^2)}$$

where N_f is the number of quark flavours involved, Q^2 the four-momentum transfer, and Λ is a scaling parameter, $\Lambda = 0.2 \pm 0.1$ GeV [Qui83]. From this expression one can directly derive that α_s decreases with increasing momentum transfer, which is equivalent with a decreasing quark distance. Hence, the asymptotic freedom at small distances is indicated by the expression for the strength of the interaction. The colour confinement at large distances is caused by the linear component in the interaction potential $V(r)$.

1.1 Quark Gluon Plasma

In analogy to the theory of the electromagnetic interaction, the quantum electrodynamics [Fey61], the gauge theory of quark interaction is called quantum chromodynamics (QCD) [Kap79, Shu95]. The QCD predicts at sufficiently high temperatures and densities an entirely new form of matter. This matter is analogous to the plasma phase of ordinary atomic matter called quark gluon plasma (QGP). In such a QGP quarks and gluons are no longer confined in hadrons, but are 'released' into a larger region, the plasma, where they are free single particles. These single particles are in contrast to normal matter not colour-less.

Theoretically, the phase transition from hadronic matter to a possible QGP has been studied in lattice QCD calculations. This allows to estimate the critical temperature of $150 \sim 200$ MeV [Lae96] at which this phase transition might occur. It is commonly believed that such high temperatures and thus a QGP existed right after the *big bang*, the believed origin of our present universe. Today a QGP is expected to exist, due to high particle densities, in neutron stars. One of the major goals of high energy physics is the creation of such conditions in the laboratory. By means of high energy heavy ion collisions it is expected that a sufficiently large particle density and temperature can be established to form a QGP.

Contrary to the ordinary plasma phase the QGP characteristics are not directly observable. However, there are several different probes suggested as signatures. Recent reviews of the different possible QGP

signatures can be found for example in [Bas98, Har96]. The probes can be categorized into probes of the initial state, probes of chiral symmetry restoration, probes of deconfinement, and probes of the collision dynamics.

Probes of the Initial State

As signal of the QGP an excess of produced photons and lepton pairs was predicted [McL85]. They are not subject to the strong force and therefore probe the earliest and hottest phase of the evolution of the QGP without being affected by final state interactions. The expected signal from the direct photons and the lepton pairs compete with the background of several hadronic reactions [Fei76], thus it is difficult to disentangle. Moreover, a thermal hadron gas is also a source of photons of comparable intensity [Kap93]. However, a clear signal of photons from a QGP is believed to be visible for high transverse momenta if a very hot plasma is formed initially [Sri92]. Thorough studies in heavy ion collisions are currently in progress [Agg98f] and an upper limit of the thermal photon production could already be obtained [Alb91].

Probes of Chiral Symmetry Restoration

The phase transition would also restore the broken chiral symmetry, i.e., make the quarks behave as though they are mass-less. This could result in the formation of so-called disoriented chiral condensates (DCC) [Bjø92]. The DCC would decay into neutral and charged pions, favouring a neutral-to-charged ratio different from the value expected from isospin symmetry. Such events that virtually violate the isospin symmetry have been observed in the so-called Centauro events from cosmic ray interactions [Lat80] and is currently studied in high energy heavy ion collisions [Agg98a, Ste98, Wys98].

Probes of Deconfinement

The production of hadrons with strange quarks is normally suppressed in nuclear reactions. The yield of multi-strange baryons is predicted to be strongly enhanced in the presence of a QGP [Raf82]. However, several calculations have been presented [Lie91] which show the copious production of strangeness in hadronic reactions. Nevertheless the strangeness abundance can be a useful trigger for other signals of a QGP. Additionally it is commonly believed that compared to a hadronic process, the J/Ψ production is suppressed in the collision of two nuclei forming a QGP [Mat86]. Although there are several hadronic mechanisms that could explain a J/Ψ suppression [Gav94], it is still believed to be good signature of the QGP formation.

Hard partons, i.e. quarks or gluons with very high energies, might be formed during the early stage of the phase transition. When such a parton traverses deconfined matter it can interact with harder gluons than in confined matter, where gluons are constrained by the hadronic parton distribution. Fast partons lose more energy per unit length in a QGP than in hadronic matter, hence the energy loss might be a signal of a QGP existing or not. On the other hand a suppression of hard partons might be difficult to disentangle from the average transverse momentum of hadrons, which is expected to be enhanced in a QGP [Sat98].

Probes of the Collision Dynamics

These probes are based on the energy density ϵ, the pressure P, and the entropy density s of ultradense hadronic matter as a function of the temperature T and baryochemical potential μ_B. As a signature of a QGP the rapid rise in the number of degrees of freedom within a small temperature range is predicted. In heavy ion experiments the average transverse momentum $\langle p_T \rangle$, the hadron rapidity distribution dN/dy[1], and the transverse energy dE_T/dy are commonly identified with the variables T, s, and ϵ, respectively. Therefore a rapid change in the $\langle p_T \rangle$ dependence on dN/dy or dE/dy could serve as probe for possible phase transition.

The space-time evolution of the system can be measured via identical particle interferometry, which is also referred to as HBT[2] effect [Han54]. It was predicted that a phase transition, which is changing the expansion dynamic, would show up in the studied $\pi\pi$, KK, or pp correlation functions and could therefore be a measurable signature of the QGP [Pra86].

The high particle density of the reaction zone leads to the formation of a collective outward flow during the expansion of the dense matter. The excitation function of the transverse collective flow is the earliest predicted signal for probing the nuclear matter [Sch68]. The excitation function is sensitive to the equation of state (EOS) of nuclear matter, i.e. the relationship specifying how the pressure, or alternatively the energy per particle, depends on density and temperature. And the excitation function can be used to search for abnormal matter and phase transitions [Hof76, Sto86]. In high energy collisions two heavy nuclei can be compressed and heated to much more than in ground state. Thus a flow pattern will develop as the system subsequently expands. Hence the observation of collective flow phenomena is of high interest for both, the search of a phase transition to a QGP and the study of the nuclear collision dynamics.

1.2 Collective Flow

The existence of shock waves and the collective flow was predicted already 30 years ago [Sch69]. Experimentally, the first evidence of the occurrence of sideward flow was obtained 15 years later in the Plastic Ball experiment at the Bevalac in Berkley [Gus84]. By now the flow analysis is one of the well established methods to extract information about the EOS and the transport properties of the hot nuclear matter [Cse94]. Three different types of transverse flow are distinguished, radial, directed, and elliptic flow. Isotropic expansion in the transverse direction is called radial flow, which is studied by means of inclusive transverse momentum spectra. The comparison of these spectra with thermodynamic models provides the temperature T and the transverse flow velocity β_x [Sch93]. The obtained quantitative values, however, depend on the used model and are therefore difficult to determine [Agg98e]. The radial flow can even be measured in central events and does not depend on the determination of the reaction plane, i.e. defined by the beam

[1] For a definition of the rapidity see appendix A
[2] Hanbury-Braun, Twiss

axis and the line joining the two centres of the colliding nuclei (see figure 1.1 and chapter 4 for a detailed explanation).

Anisotropic expansion in non-central events is described by the directed and elliptic flow components. Figure 1.1 displays a non-central collision of two nuclei in the participant-spectator model. The projectile

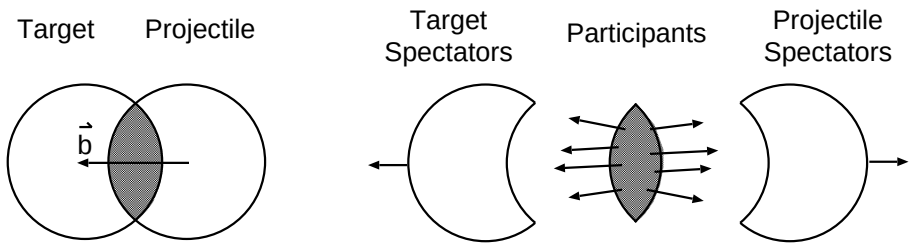

Figure 1.1: Schematic view of two colliding nuclei in the participant-spectator model. The collision is shown in the centre-of-mass frame. The beam axis, i.e. the direction of the projectile, points into the drawing plane. The distance of projectile and target is named impact parameter $\vec{b}$.

is flying into the drawing plane, while the target is coming out of this plane. The beam axis points into the drawing plane and defines together with the impact parameter $\vec{b}$ the reaction plane. In the participant-spectator model the nucleons interact only in the overlap region of both nuclei. This interaction zone is due to the expected high temperature also named fireball. Hence this model is also referred to as fireball model. In non-central collisions the overlap region has an azimuthal anisotropic geometrical shape (see left figure panel). Thus the pressure gradient in the fireball is steeper along the impact parameter than perpendicular to it. And a collective motion of the particles emitted from the fireball is expected to develop in the direction parallel to $\vec{b}$. The spectators are deflected by the emitted particles, hence they will show transverse flow effects in addition to their movement parallel to the beam axis (right figure panel).

Directed Flow

The directed flow is based on the fact that a reaction plane can be determined. At low beam energies the *side-splash* [Gus84] of participant nucleons near midrapidity was detected. By side-splash is meant the azimuthal anisotropy of the emission of produced particles. In other words particles near midrapidity are preferentially emitted in the reaction plane and transverse to the beam axis rather than emitted isotropically. Spectator fragments are deflected from the participants, thus they also show an anisotropic emission pattern. This *bounce-off* of the spectators results also in the reaction plane and transverse to the beam axis [Bec87].

In high energy collisions directed flow is essentially a pressure gradient effect, due to the azimuthal anisotropy of the hot central region in non-central nucleus-nucleus collisions. The denotation *directed flow* comprises both the side-splash effect, and the bounce-off effect. This means the particles are preferentially emitted in a direction transverse to the beam axis. In such a collective sideward flow the particles emitted in forward and backward hemispheres in the centre-of-mass frame are, due to momentum conservation, found on opposite sides of the beam in the reaction plane. Thus directed flow can be equated with the transverse

momentum transfer in the reaction plane. The magnitude depends on the centrality of the collision. For central collisions the directed flow vanishes due to the symmetry, and for very peripheral collisions the flow effect is expected to be weak, because the compressional effects are low. The different methods to extract the directed flow signal from the measured data are described in chapter 4 – 6.

Elliptic Flow

In addition to the directed flow in the reaction plane an out-of-plane flow component, the *squeeze-out*, was observed at Bevalac energies [Gut89a, Gut90]. In the overlap region of the two colliding nuclei the matter is rather compressed and partly it is squeezed out perpendicular to the reaction plane. In other words, the particles emitted from the central hot region are shadowed in the reaction plane by spectator fragments. Perpendicular to the reaction plane there are no spectators, thus particles might escape preferentially in this direction. In collisions at ultrarelativistic energies the spectator matter is expected to leave the interaction zone after such a short time that shadowing is small. This would lead to an isotropic emission pattern for all particles emitted after this time. However, if partial thermalization occurs, pressure will drive them along the lines of the pressure gradient. Since the overlap region between target and projectile has a smaller size in the reaction plane than perpendicular to it, the pressure gradient is larger in-plane. This consequently produces in-plane elliptic flow [Oll92]. The utility of the elliptic flow excitation function as a probe for the stiffness of the EOS of nuclear matter and for the onset of a possible QGP is recently under investigation [Dan98]. A recent overview of collective flow phenomena observed in heavy ion collisions can be found in [Rei97]. The analysis method will be described in chapter 6.

Since the measurement of collective flow phenomena provides a unique tool for studies of the dynamics of a heavy ion collision as well as for the properties of hadronic matter, this thesis concentrates on the analysis of flow phenomena in high energy heavy ion collisions. The analyzed data are Pb + Pb collisions measured in the WA98 experiment at the CERN[3] SPS[4] at a beam energy of $33\ \mathrm{TeV}$.

The setup of the WA98 experiment will be described in chapter 2. Chapter 3 deals with the data reduction which provides the event characterization as well as the necessary variables for the flow analysis. Observation of collective flow requires that a reference plane exists. Different methods of extracting this reaction plane, are discussed in chapter 4, along with results on the reaction plane determination and its resolution. Chapter 5 presents the results of the directed flow analysis by means of the average transverse momentum $\langle p_x \rangle$ method. The analysis using azimuthal particle correlations in chapter 6 provides results on elliptic and directed flow and comparisons to the $\langle p_x \rangle$ method. Finally in chapter 7 the results of the observed collective flow phenomena are briefly summarized.

[3] Conseil Européene pour la Recherche Nucléaire
[4] Super Proton Synchrotron

2. The WA98 Experiment

The WA98 experiment uses a variety of large acceptance detectors to take into account, that only the simultaneous measurement of several observables and their correlations allows to obtain a complete picture of the heavy ion reaction. Unlike other CERN experiments WA98 does not focus on one particular aspect, but tries to reveal a more global view of high energy collisions. The WA98 experiment is the successor of WA80 and WA93 and therefore the completion of a series of heavy ion experiments at the CERN SPS accelerator searching for signatures of the QGP. As it can be seen in figure 2.1 the WA98 experiment consists of a large acceptance hadron and photon calorimeter [WA98a, WA98b, WA98c, WA98d]. It is a fixed-target experiment with a $33\,\mathrm{TeV}$ beam of lead ions (^{208}Pb). The targets used most, are lead foils of 210 and $410\,\mu$m thickness.

The following sections give a brief overview over the different detector systems and their operating principles. The subset of detectors used for the analysis presented in this thesis is described in more detail.

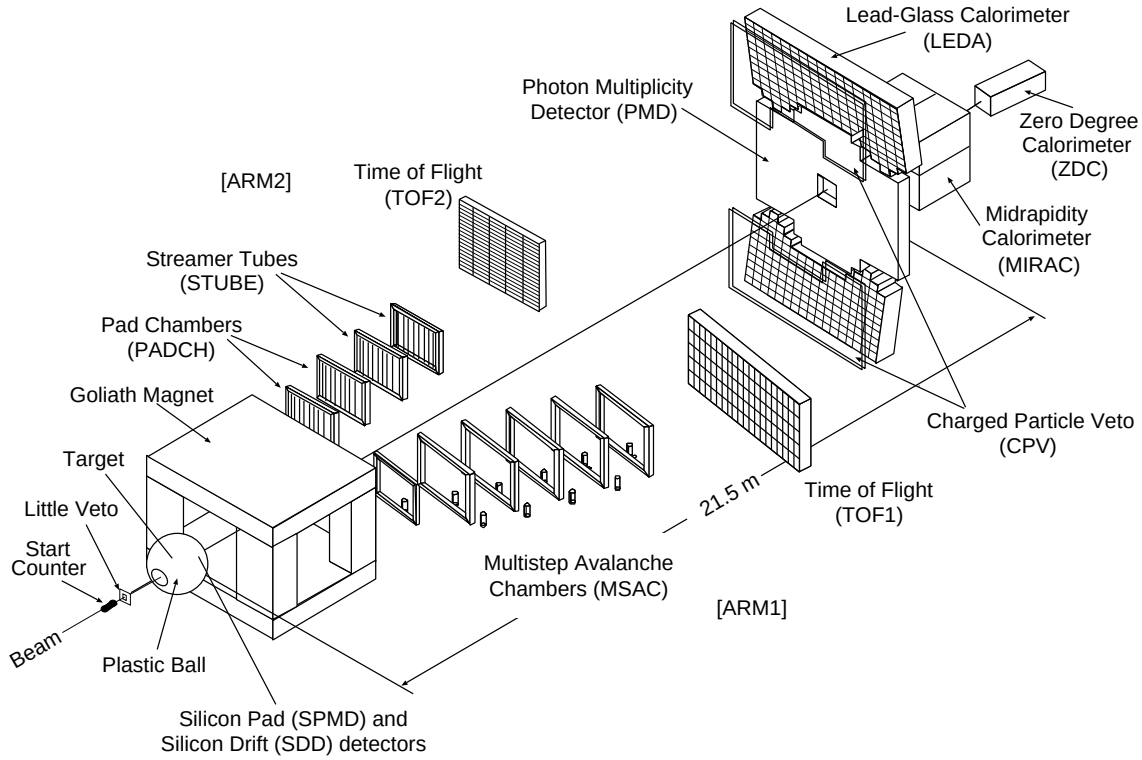

Figure 2.1: The WA98 experimental setup in 1996. Since the Inner and Outer Halo counters are $\approx 6\,\mathrm{m}$ upstream from the target, which is located in the centre of the Plastic Ball, they are outside the plotting range.

2.1 Calorimeter

To characterize the collision it is mandatory to determine the fraction of the incident energy which is dissipated for particle production. In the WA98 experiment this is realized by measuring, on the one hand, the forward energy carried by the projectile spectator fragments and on the other hand the transverse energy of the emitted particles.

The Zero Degree Calorimeter (ZDC) measures the energy of projectile spectator fragments. It covers the pseudorapidity[1] region $\eta \geq 5.9$ which corresponds to an opening angle of $\theta \leq 0.3$ around the beam axis. The ZDC is a sampling calorimeter built of 7×5 modules consisting of layers of lead and plastic scintillator. The intensity of the scintillation light that is produced by hadronic showers is proportional to the hadron energy and is guided by a wavelength shifter to photomultipliers [Awe93, Vod93a].

The Mid Rapidity Calorimeter (MIRAC) located 24 m downstream from the target is used to measure the flow of energy emanating transversely from the collisions. The covered pseudorapidity range is $3.5 \leq \eta \leq 5.5$. It is segmented transversely, enabling it to determine the transverse energy of the produced particles. The transverse energy is defined as:

$$E_T = \sum_{i=1}^{N} E_i \, \sin\theta_i \tag{2.1}$$

The sum runs over all detector modules N with E_i the energy deposited in the module at the polar angle θ_i. The MIRAC is also segmented longitudinally into an electromagnetic section and a hadronic section. Iron and plastic scintillator plates constitute the hadronic section of 6.1 absorption lengths and an energy resolution of $46.1\%/\sqrt{E/\mathrm{GeV}}$. The electromagnetic section consists of lead and plastic scintillator plates of 15.6 radiation lengths total depth. Its energy resolution is $17.9\%/\sqrt{E/\mathrm{GeV}}$. The scintillators in the electromagnetic and in the hadronic segment are read out by wavelength shifters and photomultipliers [Awe89, Idh93].

2.2 Charged Particle Tracking

Together with the large aperture magnet Goliath two tracking arms allow the spectrometry of charged particles. In addition two time-of-flight walls measure the velocity to provide the mass of each particle. Goliath is centred 3.28 m downstream of the target, with a gap size of 1.60 m. It is a 1.6 Tm dipole magnet bending the positively charged particles to the second tracking arm side, which is defined as the positive x-axis.

2.2.1 First Tracking Arm

The first tracking arm spectrometer (ARM1) consists of six Multi Step Avalanche Chambers (MSAC) and a Time-of-flight wall (TOF1). Negatively charged particles are, according to their momentum, deflected by the magnetic field of Goliath to the side of the first tracking arm. When they pass one of the MSAC

[1] For a definition of the pseudorapidity see appendix A

planes, they ionize the gas along their path through the chamber. With several amplifying steps an electron avalanche is produced, which excites the triethylamine molecules in the gas chambers to emit photons. These photons are absorbed and reemitted by wavelength shifter exit windows which are viewed by CCD[2] cameras. From the CCD signals particle hits in each plane are constructed, which in turn allow the track reconstruction and finally the determination of the incident particle momentum [Iży91, Iży94, Rub95, Sol92].

By measuring the particle velocity with the TOF1, which consists of 4×120 plastic scintillators each read out from both sides with photomultipliers, one can reconstruct the particle mass and therefore the particle identity. The TOF1 has a time resolution of ≈ 120 ps [Kur96, Vod93b].

2.2.2 Second Tracking Arm

The measurement of positively charged particles in the second tracking arm (ARM2) is analogous to the tracking of negatively charged particles. Four tracking planes are used, two Pad Chambers (PADCH) and two Streamer Tube detectors (STUBE). The Pad Chambers are similar to the MSACs, except for the readout. In the Pad Chambers the electron avalanche induces charge on pads outside the chamber. Instead of measuring the secondary produced photons with a CCD camera, these pads are read out directly. The spatial resolution is 1.7 mm in the vertical and 0.5 mm in the horizontal axis [Car98a, Car98b].

The design of the Streamer Tube detectors is adopted from the Charged Particle Veto detector (CPV) as described in section 2.3.4. In order to achieve a good track reconstruction the spatial resolution is improved by reducing the vertical dimension of the readout pads compared to the CPV. For the particle identification the positive tracking arm is also equipped with a Time-of-Flight wall (TOF2). It is made of 5×96 plastic scintillators, each read out by two photomultipliers, and achieves a time resolution of ≈ 80 ps [Eno97, Kiy97].

2.3 Multiplicity Detectors

In the following subsections the multiplicity detectors are presented. The measurement of the charged particle multiplicity is realized by the Silicon Drift Detector (SDD) and the Silicon Pad Multiplicity Detector (SPMD) near the target, and with the CPV further downstream. The photon multiplicity is determined with the Photon Multiplicity Detector (PMD).

2.3.1 Silicon Drift Detector

The SDD is a circular silicon wafer of 4 inch diameter and $280\,\mu$m thickness with a 15 mm diameter hole in the centre, which allows the non-interacting beam particles to pass through. It covers the pseudorapidity range of $2.0 \leq \eta \leq 3.4$ and is located 125 mm downstream from the target. An energetic charged particle traversing the wafer creates a cloud of electric charges which, due to the applied voltages, drift radially

[2] Charged-Coupled Device

towards the outer edge of the wafer. By measuring the drift time one can reconstruct the radial distance of the traversal point of the energetic particle. The azimuthal angle is determined by the centre of gravity of the responding anodes, which are arranged around the outer edge of the wafer. The resolution is $25\,\mu$m along the drift direction and 35 μm in the azimuthal direction. [Nie94, Ras96, Reh90, Ste94]

2.3.2 Silicon Pad Multiplicity Detector

The SPMD, which is located 328 mm downstream from the target, covers a pseudorapidity range of $2.35 \leq \eta \leq 3.75$. It is a circular 4 inch silicon wafer. A traversing charged particle creates free charge which is read out directly via small pads. The SPMD is made of four quadrants with 1012 pads each. Because of the high particle multiplicity in a heavy ion collision the probability of double hits is not negligible. They can, however, be disentangled by the analysis of the signal height [Lin97, Ste98].

2.3.3 Photon Multiplicity Detector

In the PMD, photons are detected via electromagnetic showers to which they convert in the 3 radiation lengths thick lead converter plates. The produced shower particles give rise to a large signal in 3 mm thick scintillator pads. These pads are read out by wavelength shifting optical fibers coupled to image intensifiers and CCD cameras. Hadrons, due to their large nuclear interaction length, will mainly traverse the converter without showering. Thus they will give only a small signal in the scintillator (as minimum ionizing particle), which gives a handle to discriminate them. Situated 21.5 m downstream from the target the PMD allows the counting of photons in the pseudorapidity range $2.4 \leq \eta \leq 4.4$ [Agg96, Agg98c].

2.3.4 Charged Particle Veto

On the one hand the CPV is used as a multiplicity detector for charged particles and on the other hand it is used as a veto detector for the Lead Glass Detector Array (LEDA), which measures photons and neutral mesons (see section 2.4). The CPV is built in two walls of 86 streamer tubes each. A single streamer tube is divided into 8 chambers with a $100\,\mu$m thick anode wire in each. The high voltage applied to the anode forms an electric field, in which a traversing charged particle creates a spatially limited charged streamer. This charge induces a signal on the pads outside the tube.

In total 49,120 pads are read out in groups of 16 by digitizing chips, which are a completely new development. The digitized signals are then handled by Digital Signal Processors (DSP), also a new design for this experiment. They reduce the data volume by rejecting pad signals below certain thresholds. Since the CPV is used as a veto detector for LEDA it covers the whole LEDA pseudorapidity range and is installed directly in front of it, i.e. within a distance of about 800 mm. A spatial resolution of 20 mm in the horizontal and 24 mm in the vertical direction is achieved [Bat97, Bar98a, Fra95, Rey95].

2.4 The Photon Spectrometer LEDA

One of the main goals of the WA98 experiment is the measurement of direct thermal photons. For this purpose the lead glass detector LEDA was built. It detects photons in the pseudorapidity region $2.28 \leq \eta \leq 2.96$. It is positioned at a distance of $21.5\,\mathrm{m}$ to the target.

2.4.1 Mode of Operation

Energetic electromagnetically interacting particles such as electrons and positrons lose their kinetic energy in material via Bremsstrahlung. Photons lose their energy by electron-positron pair production. The secondary particles then interact in the same way so that an electromagnetic shower is created. The further extension of the shower is stopped as soon as the kinetic energy of the particles falls below the critical energy E_c. The longitudinal dimension of a shower is described by the radiation length X_0, after which distance the primary electron or positron has lost $63\,\%$ of its energy.

The transverse dimension is determined by the Molière radius:

$$R_M = \frac{21\,\mathrm{MeV} \cdot X_0}{E_c} \tag{2.2}$$

where $95\,\%$ of the primary energy is deposited in a cylindric volume with the radius $2\,R_M$ around the shower axis.

Hadrons, however, have a larger mean free path, such that only $\approx 63\%$ build a shower in LEDA. The hadron shower is unlike an electromagnetic shower since it consists not only of electrons, positrons, and photons but contains hadrons as well. Therefore the lateral shower dimension is larger and can be used to distinguish between photons and hadrons (see section 3.2.2). The remaining $\approx 37\%$ of the hadrons traverse the detector material decreasing their energy by ionization. They are known as minimum ionizing particles and can be identified by their low energy signal [Fab87, Kle92, Leo87].

Since all charged shower particles with a velocity of $\beta\,c > c/n$, where c/n is the speed of light in the detector medium with the refraction index n, emit Čerenkov photons in the lead glass, the total energy of a shower can be determined by measuring the number of produced photons [Čer37, Jel58, Per87].

2.4.2 Detector Design

The LEDA detector consists of 10,080 single lead glass modules sized $40 \times 40 \times 400\,\mathrm{mm}^3$, which corresponds to 14.4 radiation lengths. 6×4 modules are combined to stand-alone subdetectors, so-called supermodules. A detailed description of the construction and calibration of LEDA can be found in reference [Sch94b]. The concept of a modular construction allows a variable detector geometry and therefore the use of the detector in other experimental setups.

This is necessary, because the LEDA detector – after its operation in WA98 – is presently included in

the electromagnetic calorimeter of the PHENIX[3] experiment at RHIC[4] [Mor98], where the supermodules are stacked in a different geometry [PHE93].

The LEDA setup in the WA98 experiment is displayed in the left part of figure 2.2. Every rectangle represents one supermodule as shown in the right half of the figure.

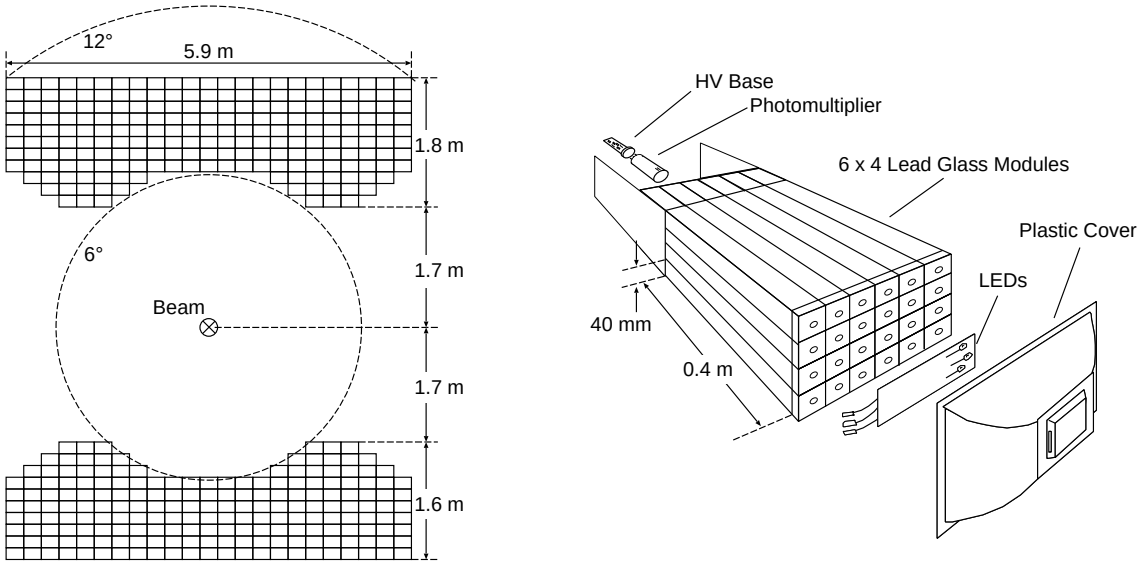

Figure 2.2: Schematic view of the LEDA setup on the left, where each of the 420 supermodules is represented by a single rectangle. The construction of such a supermodule is displayed in the right part.

To make the supermodule a stand-alone detector each one is equipped with an independent monitoring system. Variations in the detector response, caused by fluctuations of the temperature or the high voltage, are detected by this reference system and thus allows to correct for these effects. This is realized by a newly designed LED[5] based monitoring system, which is described in detail in the references [Pei96, Sch94a].

The produced Čerenkov light is detected and amplified by photomultipliers, which are equipped with newly developed active high voltage bases. Active bases have the important advantage of producing less heat and being more stable and easier to control than passive bases. The description of the operation and the control of this high voltage system can be found in [Hub92, Hub93, Neu95].

A completely new readout system is constructed to process the photomultiplier signals. The improvements over standard integrating ADCs[6] are an implemented analog memory, which eliminates costly delay cables for each channel, and two digitization channels for the anode charge with different amplification. In addition, high resolution measurement of the signal timing and a module cluster based trigger with adjustable energy threshold, to trigger on rare events with very energetic photons, is included on the ADC board [All91, You94].

[3] Pioneering High Energy Nuclear Ion eXperiment
[4] Relativistic Heavy Ion Collider
[5] Light Emitting Diode
[6] Analog to Digital Converter

LEDA is highly granulated and hence achieves a good resolution in space and energy which is mandatory for the photon measurement. The energy resolution can be parameterized by [Pei96]:

$$\frac{\sigma(E)}{E} = \frac{(5.5 \pm 0.6)\%}{\sqrt{E}} + (0.8 \pm 0.2)\%$$

While the spatial resolution can be described as [Cla96]:

$$\sigma = \frac{(8.35 \pm 0.25)\text{mm}}{\sqrt{E}} + (0.15 \pm 0.07)\text{mm}$$

More detailed information about the LEDA detector and its specific features can be found in several recent theses [Blu98, Boh96, Cla96].

2.5 The Plastic Ball Spectrometer

The Plastic Ball detector, originally built for experiments at the Bevalac in Berkeley [Gut89b], measures particles in the target fragmentation region. It provides coverage in the polar angle region of $160^\circ \leq \theta \leq 30^\circ$; with full coverage in the azimuthal direction. Therefore the Plastic Ball surrounds the target nearly completely. It consists of 655 detector modules, that provide particle identification via $\Delta E - E$ measurement. Due to the increased particle multiplicity at the SPS the 160 most forward modules of the original Bevalac design [Bad82] are not used in the WA98 setup. The detector geometry and the construction of a single module is shown in figure 2.3.

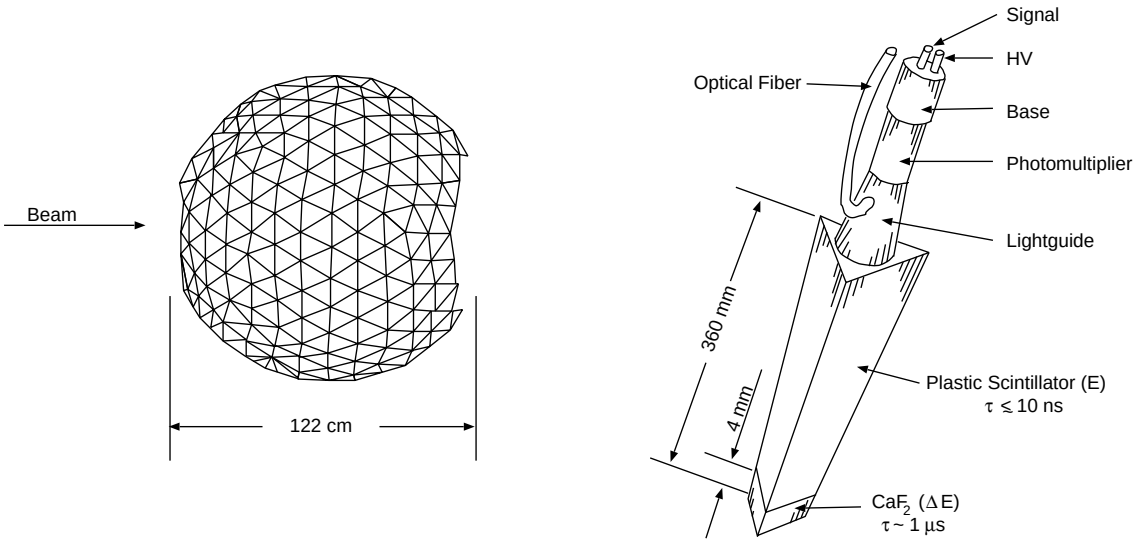

Figure 2.3: Schematic view of the Plastic Ball geometry on the left. The particular arrangement of every module can be seen in figure B.1. Every triangle represents a single $\Delta E - E$ telescope. The construction of such a module is shown in the right part with the 4 mm thick ΔE crystal and on top the E section.

Every $\Delta E - E$ module consists of two scintillator types with very different timing constants. The inner scintillator section is a 4 mm thick Eu-doped CaF_2 crystal measuring the energy loss signal ΔE. For the

emission of the scintillation light the CaF_2 has a characteristic decay time of $\approx$ 1 μs and is read out by using the E counter as a lightguide.

The E counter is a plastic scintillator of 356 mm length. The timing constant is approximately two orders of magnitude smaller, so that 90% of the scintillation light is gathered within 10 ns. The plastic scintillator has also components with longer decay times (120 ns). Hence the analysis of the pulse shape allows the measurement of both signals with one photomultiplier. The $\Delta E - E$ resolution has been found to reach an optimum when integrating the ΔE signal over 1.5 μs after a delay of 240 ns. The scintillator light is read out through a conical light guide which is coupled to a photomultiplier. The gain of the photomultiplier is monitored by a laser signal, which is connected through an additional optical fiber to the light guide.

The dimensions of the CaF_2 crystal are chosen in such a way that protons up to 40 MeV are stopped, while in the plastic scintillator protons up to 240 MeV are stopped. This permits a very good proton identification in this energy range with negligible influence of e.g. deuterons. Positively charged pions are additionally identified by their decay. With a mean time of 26 ns the stopped π^+ decays into a μ^+. The μ^+ decays after 2.2 μs into a positron e^+:

$$\pi^+ \xrightarrow{26\,\mathrm{ns}} \mu^+ \nu_\mu \xrightarrow{2.2\,\mu\mathrm{s}} e^+ \nu_e \bar{\nu}_\mu \nu_\mu$$

This positron causes a delayed signal in the plastic scintillator and a TDC[7] measures the corresponding delay time. About 90% of all decays can be detected in the TDC range 250 ns $\leq t \leq$ 10 μs.

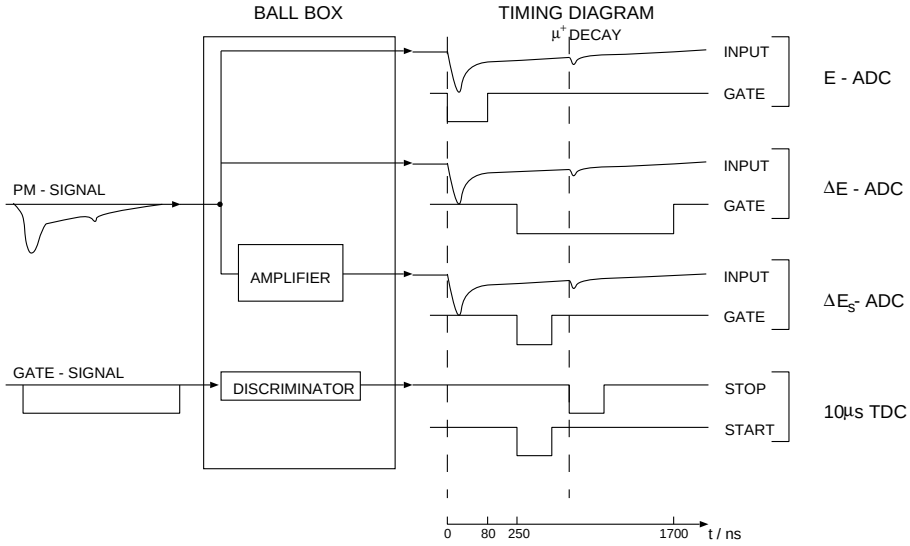

Figure 2.4: Scheme of the pulse shape analysis for the identification of π^+ in the Plastic Ball.

The scheme of the necessary pulse shape analysis for π^+ identification is shown in figure 2.4. It also includes a third ADC depicted as ΔE_s. As can be seen the μ^+ decay peak lies in the integration range of the ΔE signal, which might lead to a distortion of the latter one. Therefore alternatively the ΔE_s or a combination of both signals can be used to determine the true ΔE signal.

[7] Time to Digital Converter

Since π^- are promptly absorbed by a nucleus and the pion rest mass is released as kinetic energy this particle identification method is not possible for the negatively charged pions. The identification method for π^+, p, and heavier fragments like deuterons and tritons is presented in section 3.3.2. Since the Plastic Ball acceptance varies for different particle species it will be discussed in detail in section 3.3.3.

2.6 Trigger

The start and veto counters belong to the subsystem of the trigger detectors. The start counter is a gas Čerenkov detector which measures the incoming beam particles 3.5 m upstream of the target. Only beam particles, i.e. 158 AGeV lead ions, are accepted based on signal pulse height and give the start signal for the data acquisition. A very good timing resolution of approximately 27 ps is achieved [Chu96].

The Inner and Outer Halo counters are two scintillator walls 5.7 and 6.0 m upstream from the target. Since they are further upstream they are not shown in figure 2.1. The Inner and Outer Halo reject secondary particles, produced by possible upstream reactions of beam particles with rest gas in the vacuum beam pipe, as well as the halo of the beam consisting mainly of muons. Reactions in the start counters can also produce secondaries. These are rejected by a scintillator, the Little Veto, 3.0 m downstream of the target. The Little Veto has a hole of 3.0 mm which allows to select only very well centred beam particles.

Together with this detector subset the MIRAC, and the Plastic Ball are integrated in the trigger. While the MIRAC characterizes the centrality of the event (see section 3.1), the Plastic Ball is used to exclude events with downstream interactions. The complete trigger [Lee94] allows a very good selection of ^{208}Pb $+$ ^{208}Pb collisions as well as the definition of the collision centrality.

3. Data Reduction

The most important corrections and cuts necessary for the flow analysis are described here. The first section will deal with the transverse and forward energy production. It is described how these observables can be used to characterize the collision and how the particular centrality classes are defined. While section two presents the calibration and particle identification of LEDA, section three refers to the analysis of the Plastic Ball data.

3.1 Event Classification

The available centre-of-mass energy for particle production between two participants for the $\mathrm{Pb} + \mathrm{Pb}$ system at the SPS energy can be written as $\sqrt{s} - 2m_p$ where $\sqrt{s}$ is 17.2 GeV/nucleon and m_p is the rest mass of a nucleon in the colliding nuclei. Therefore the available energy per participant is:

$$E_{cm}^{p} = \frac{1}{2}(\sqrt{s} - 2m_p) = 7.67\,\mathrm{GeV} \tag{3.1}$$

and thus for the whole $^{208}\mathrm{Pb} + ^{208}\mathrm{Pb}$ system:

$$E_{cm} = 7.67\mathrm{GeV} \times 2 \times 208 = 3.19\,\mathrm{TeV} \tag{3.2}$$

Assuming that the E_T production is isotropic in the centre-of-mass frame, the maximum possible transverse energy of all particles can be calculated by integrating over the solid angle:

$$E_T^{max} = \frac{\int E \sin\theta d\Omega}{\int d\Omega} = E\frac{\int \sin^2\theta d\theta d\phi}{4\pi} = \frac{\pi}{4}E \tag{3.3}$$

where $E = E_{cm} = 3.19\,\mathrm{TeV}$. Thus for $^{208}\mathrm{Pb} + ^{208}\mathrm{Pb}$ collisions at SPS energy E_T^{max} is $2.50\,\mathrm{TeV}$. The maximum measured transverse energy is $\approx 460\mathrm{GeV}$, this fraction corresponds to $18.4\,\%$ of E_T^{max}. This is partly due to the fact, that the MIRAC covers only $29.5\,\%$ of the integrated $dE_T/d\eta$ distribution, which is assumed to be Gaussian [Agg97b]. The remaining discrepancy can be explained by the fact that the energy available for the particle production will be reduced by an incomplete stopping of the nucleons. This can therefore provide information to study the nuclear stopping power as done for example in the references [Alb87, Geu98, Kam93].

Furthermore the $dE_T/d\eta$ distribution allows to estimate, in terms of the Bjørken picture [Bjø83], the energy density ϵ_{BJ}:

$$\epsilon_{BJ} = \frac{dE_T/d\eta|_{max}}{\pi R_0^2 \tau_0 c} \tag{3.4}$$

Where τ_0 is the formation time taken as $1\,\mathrm{fm}/c$ and R_0 the projectile radius calculated as $R_0/\mathrm{fm} = 1.2A^{1/3}$. For a detailed description see [Agg97b, Cla96].

In figure 3.1 the forward energy E_{ZDC} is shown as a function of the transverse energy E_T. It shows the expected linear anti-correlation between the two observables. This can be understood in light of the

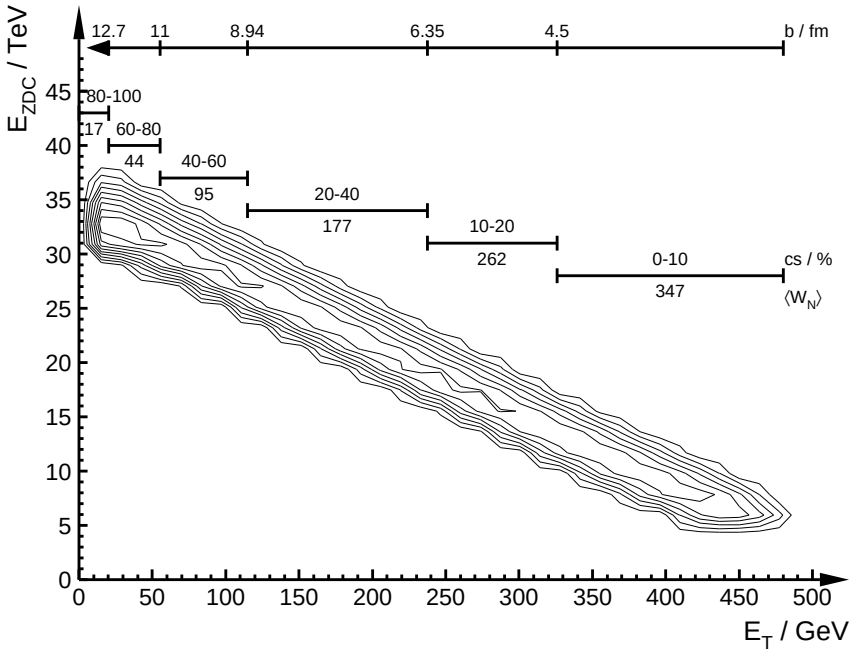

Figure 3.1: The forward energy E_{ZDC} as function of the transverse energy E_T, which is translated in an impact parameter (b) axis on the top. Also shown are the used centrality classes in terms of percentage of the minimum bias cross section (cs) and as average number of participants $\langle W_N \rangle$.

participant-spectator picture. In a peripheral collision, where the two lead nuclei just graze each other many nucleons in the colliding nuclei do not interact. This leads to both a strong forward energy flow in the projectile fragmentation region and to a low E_T production. The more the overlap of the two nuclei increases, the more transverse energy is produced and fewer spectators are emitted to the projectile fragmentation region. Hence - as described in section 2.6 - one important tool to understand the heavy ion collision is the measurement of the energy flow parallel and transverse to the beam axis.

In addition in figure 3.1 the different centrality classes used in this analysis are given as percentages of the minimum bias cross section. This is shown for the data set of the Pb + Pb beam time in 1996 where the magnetic field of Goliath was on. The magnetic field slightly changes the measured total transverse energy, which changes the transformation from E_T into percentage of the minimum bias cross section slightly compared to the magnet-off data. The shown data are corrected for pile-up events as well as for events with downstream interactions detected with the Plastic Ball. These two corrections are briefly described in appendix C. In the following analysis the mentioned cuts are always applied and the above centrality classes are used.

In addition, the relation between the cross section and the impact parameter b, as well as the average

number of wounded nucleons, i.e. the number of participants, $\langle W_N \rangle$ are given in this plot. The latter are derived from the impact parameter in Monte Carlo simulations [Pei98] inspired by the Glauber model [Gla70]. This simulation, which is mainly based on geometry, is a multiple scattering theory. It uses a Woods-Saxon nucleon density profile. In the Glauber formalism the number of participants in the collision of two nuclei A and B can be written as:

$$\begin{aligned} W_N(b) &\approx \int \left\{ N_A(\vec{x}) \left(1 - e^{-\sigma_{nn} N_B(|\vec{b}+\vec{x}|)}\right) + N_B(|\vec{b}+\vec{x}|) \left(1 - e^{-\sigma_{nn} N_A(\vec{x})}\right) \right\} d^2\vec{x} \\ &\approx 2\sigma_{nn} \int N_A(\vec{x}) N_B(|\vec{b}+\vec{x}|)\, d^2\vec{x} \end{aligned} \tag{3.5}$$

where $\sigma_{nn} = 32\,\text{mb}$ is the inelastic nucleon-nucleon reaction cross section and $N_{A,B}(\vec{x}) \equiv \int \rho_{A,B}(z,\vec{x})\, dz$ is the number of nucleons per unit area with the nuclear density function $\rho_{A,B}(z,\vec{x})$. $\vec{b}$ is the impact parameter and z is the coordinate in the direction of the beam axis, while $\vec{x}$ is the integration variable perpendicular to the beam axis. The integral in the second row in equation (3.5) shows that the number of wounded nucleons W_N is an overlap of the densities of the projectile and the target nuclei separated by their distance $\vec{b}$ [Sor90].

3.2 LEDA γ and π^0 Measurement

The LEDA data analysis is very thoroughly described in recent LEDA related theses (see the subsections for references), thus this section will only briefly note the main strategy to extract the physics observables. The first section deals with the calibration and the necessary corrections and the second section presents the photon identification method. Section three summarizes the neutral meson reconstruction.

3.2.1 Calibration and Corrections

Prior to the physics beamtime with Pb nuclei a calibration beamtime with electrons of known incident energy was performed. In 1993 and 1994 the detector response to $10\,\text{GeV}$ electrons was recorded for each single lead glass module [Sch94a, Sch94b]. Since electrons create an electromagnetic shower in the lead glass like photons (see section 2.4.1), these results are used to translate the ADC channels into energy. To evaluate the actual gain factors an iterative procedure was used. This procedure provides the energy calibration on a single module basis. Small differences on a 1% level between the photon and the electron response have been found by simulations [Büs97] and are corrected for.

Since the experiment, including the calibration beam time, lasts for several years, fluctuations in the high voltage or photomultiplier aging effects are possible reasons for changes in the light amplification. Thus the calibration has to be monitored and, if necessary, modified continuously. Therefore the monitoring system (see section 2.4.2) provides a time dependent control of the gain factors. The strategy is to regularly measure a calibrated LED signal in each lead glass module. The time variation of the response to the LED pulse is used as reference to correct the gain factor [Boh96, Cla96].

Moreover some well studied corrections have to be applied to the LEDA data. These are the suppression of suspicious modules, the handling of readout errors, the adjusting of the two digitizing ADC channels, the ADC pedestal correction, as well as the correction for the incident angle. These corrections are documented in detail in [Blu98].

3.2.2 Photon Identification

After applying all corrections the energy and the position information of every hit detected with LEDA are known. Since the behaviour of photons and electrons on the one hand and hadrons on the other is known, their different behaviour can be used to identify the hit with a particular particle type. The main purpose is to study photons which leads to the necessity of an optimized hadron suppression.

Most of the hadrons traverse the detector material losing only a part of their energy by ionization (see section 2.4.1). These hadrons can be identified by their small energy deposition; a 750 MeV energy cut is applied to eliminate these minimum ionizing particles (MIPs). However one also loses low energy photons by this method. This can be improved by suppressing charged particles with the use of the CPV [Rey99].

For all particles which create a shower in the lead glass, the shower dimensions are used to distinguish between electromagnetic and hadronic showers [Ber92]. The lateral shower extension can be quantified by the dispersion:

$$\begin{aligned} D_x &\equiv \frac{\sum_i E_i\, x_i^2}{\sum_i E_i} - \left(\frac{\sum_i E_i\, x_i}{\sum_i E_i}\right)^2 = \left\langle x^2 \right\rangle - \left\langle x \right\rangle^2 \\ D_y &\equiv \frac{\sum_i E_i\, y_i^2}{\sum_i E_i} - \left(\frac{\sum_i E_i\, y_i}{\sum_i E_i}\right)^2 = \left\langle y^2 \right\rangle - \left\langle y \right\rangle^2 \end{aligned} \tag{3.6}$$

Where the sum runs over the i modules contributing to the shower of the particular hit and x_i, y_i are the transverse distances from the shower centre. $\langle x \rangle$ and $\langle y \rangle$ are then the energy weighted first moments of the hit. Since the detector is of modular granularity the x and y coordinates are in module units. The dispersions D_x and D_y are limited by the parabolic functions $D_{x,min}$ and $D_{y,min}$, respectively:

$$\begin{aligned} D_{x,min} &= \left|\langle x \rangle\right| - \langle x \rangle^2 \\ D_{y,min} &= \left|\langle y \rangle\right| - \langle y \rangle^2 \end{aligned} \tag{3.7}$$

The corrected dispersion D as defined in equation 3.8, however, is independent of the incident coordinates. It is used to distinguish between hadrons and photons, since hadrons have a relatively large dispersion while electromagnetic showers show a small value of D.

$$\begin{aligned} D_{x,corr} &= D_x - D_{x,min} \\ D_{y,corr} &= D_y - D_{y,min} \\ D &= \max\left(D_{x,corr}, D_{y,corr}\right) \end{aligned} \tag{3.8}$$

The applied threshold for hadron discrimination D_c, given in equation 3.9, rejects about 75% of hadrons. However one has to accept a 1% photon loss.

$$D \leq D_c \equiv \begin{cases} 0.267 & ; E/\text{GeV} \leq 10\,\text{GeV} \\ 0.167 + E/100\,\text{GeV} & ; E/\text{GeV} > 10\,\text{GeV} \end{cases} \tag{3.9}$$

This threshold is the same as used in former analyses [Cle93, Höl93].

3.2.3 π^0 Meson Reconstruction

The reconstruction procedure is presented here in a rough outline since like the photon identification, it has been studied and thoroughly described in the theses [Blu98, Höl95, Stü99]. Most of the photons detected in LEDA originate from neutral meson decays. The dominant yield is the $\pi^0 \longrightarrow \gamma\gamma$ decay with a branching ratio of $\approx 98.8\%$. The mean life time of a π^0 is $\tau = 8.4 \cdot 10^{-17}$s [Bar96], which means the decay occurs in the target. Therefore the emission point of the decay photons is approximately known and the high precision γ energy measurement and the high spatial resolution of the LEDA detector allow the reconstruction of the original π^0 meson.

Because of the high particle multiplicity it is not possible to find the two corresponding photons of one particular pion decay. Instead all $\gamma\gamma$ pairs are constructed and the pion spectra are evaluated on a statistical basis. For each pair the invariant mass $m_{\gamma\gamma}$ is determined from the four-momentum $p^\mu_{1,2} = (E_{1,2}, \vec{p}_{1,2})$ of the two photons:

$$m_{\gamma\gamma} = \sqrt{(p^\mu_1 + p^\mu_2)^2} = \sqrt{2E_1E_2(1 - \cos\psi)} \tag{3.10}$$

where ψ is the opening angle between the two photons in the laboratory frame and $E_{1,2}$ their energy. The second part of equation 3.10 results since photons have no rest mass. In the $dN_{\gamma\gamma}/dm_{\gamma\gamma}$ distribution, there will be a peak at the π^0 mass $m_{\pi^0} = 134.98\,\text{MeV}/c^2$. Unfortunately this peak is superimposed on the huge combinatorial background of non-correlated photon pairs. In figure 3.2 the foreground and the background distributions are shown for the transverse mass region $0.9\,\text{GeV}/c^2 < m_T - m_0 < 1.0\,\text{GeV}/c^2$. The transverse mass is defined in equation 3.11 where m_0 is the π^0 rest mass.

$$\begin{aligned} m_T &\equiv \sqrt{m_0^2 + p_T^2} \qquad \text{with} \\ p_T &\equiv \sqrt{p_x^2 + p_y^2} \end{aligned} \tag{3.11}$$

To extract the π^0 peak content one has to subtract the combinatorial background which can be obtained from the event-mixing method. With this method photons from different events are combined. Since they cannot result from real meson decays, they simulate the combinatorial background. Differences in the phase space distribution are taken into account by only mixing events from the same centrality class. The mixed-event background is scaled to the foreground and then subtracted from the latter one. The inset in figure 3.2 shows the result. The peak is integrated to obtain the number of pions within the particular m_T range. The resulting pion spectra then have to be corrected for the acceptance and the efficiency as described in [Agg98d, Alb98, Blu98, Buc99].

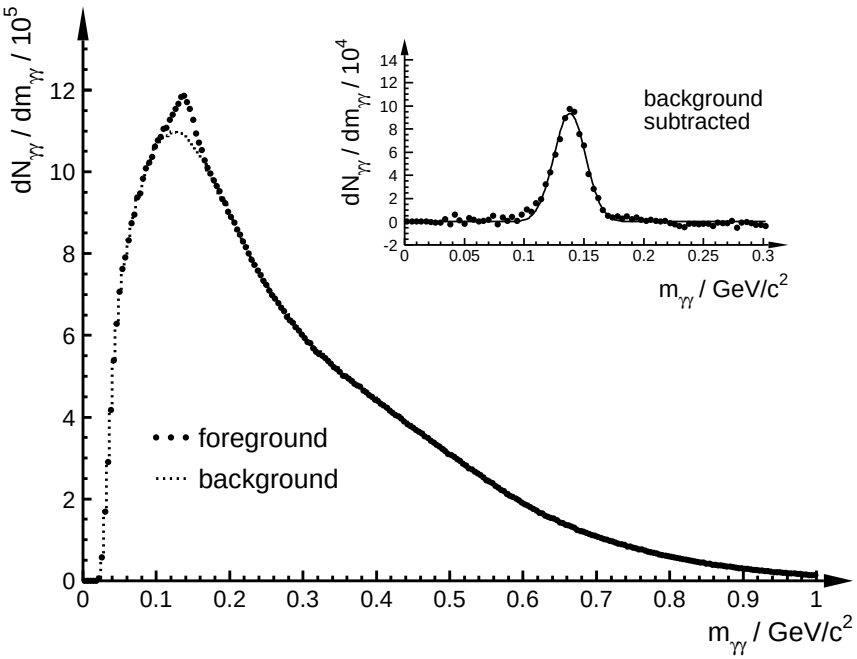

Figure 3.2: The invariant mass distribution for the transverse mass region $0.9\,\mathrm{GeV}/c^2 < m_T - m_0 < 1.0\,\mathrm{GeV}/c^2$. Shown is the mixed-event background distribution, which is scaled to the foreground $dN_{\gamma\gamma}/dm_{\gamma\gamma}$. The inset shows the difference of both distributions, the solid line represents a Gaussian fit. The data are from [Blu98].

3.3 Plastic Ball

Since most of the presented data are measured by the Plastic Ball detector, this section provides a brief introduction in the data analysis. In particular the checks on possibly suspicious modules and the particle identification method are described.

3.3.1 Module Check

In the left part of figure 3.3 the number of hits per event for each single Plastic Ball module $M_i|_{1\leq i\leq 655}$ is shown. The high particle multiplicity per event becomes evident.

Because WA98 is a fixed target experiment most of the particles, when viewed in the laboratory frame, carry after the collision still a large forward momentum. This leads to a higher hit multiplicity in the forward modules than in the backward modules, as displayed in figure 3.3. The polar angle θ increases with the module number i (see appendix B). The distribution is fitted with a second order polynomial. One can see at once that three modules have a large deviation from this fit function.

To get a closer view the distribution is projected onto the y-axis after straightening by the fit function. The right plot in figure 3.3 shows this projected distribution ζ, which is fitted with a Gaussian. Four single modules happen to be out of the 4σ cut applied on this distribution, consequently these modules are not used in the further analysis. The reason for this deviation might be the aging of the crystal scintillator or the

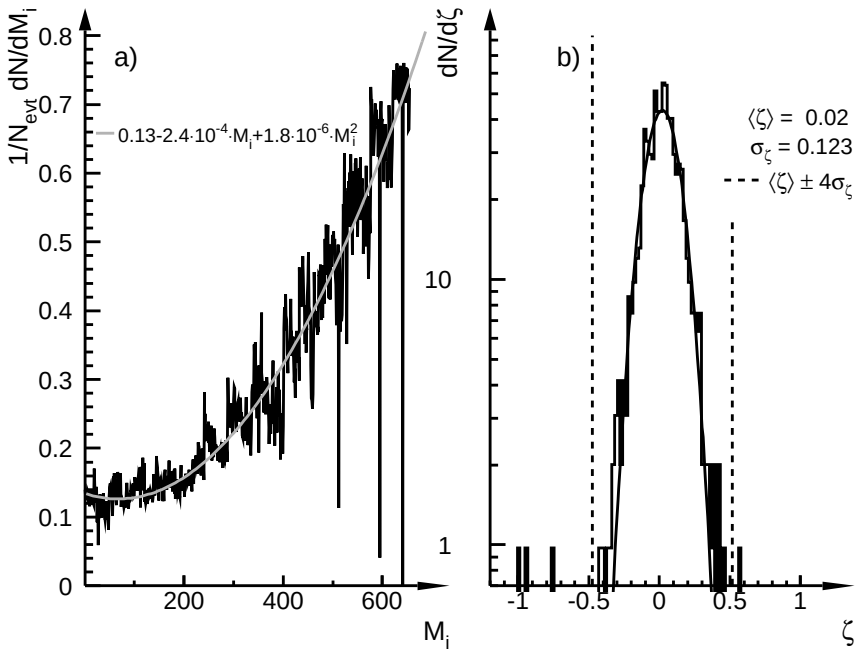

Figure 3.3: Number of hits per event for each Plastic Ball module M_i a). The solid grey line represents a second order polynomial fit. To reject suspicious modules the difference of the distribution and the fit function is projected on the y-axis. This projection ζ is shown in b). A Gaussian fit to the ζ distribution is given by the solid curve. The dashed lines show the applied 4σ cut.

photomultiplier, a wrong calibration, or problems with the high voltage.

Since two of these modules are in the most forward region these are not used for the flow analysis. The two remaining bad modules mean a loss of $0.38\,\%$ of the full coverage due to the applied cut.

3.3.2 Particle Identification

The particle identification strategy is based on the simultaneous measurement of the energy E and the energy loss ΔE signal as described in section 2.5. To identify the positively charged pions the TDC signal is additionally used. Fragments with the same energy but an different number of nucleons, such as protons, deuterons, and tritons (p, d, and t), can be distinguished by their different energy loss ΔE. Figure 3.4 indicates the analytic method.

For the modules in the $\theta \geq 60^\circ$ region the ADC signal of the energy loss ΔE is plotted versus the ADC signal from the E counter. The band for protons, deuterons, and tritons can clearly be seen, while the pions accumulate below the proton band.

A graphical cut on the two dimensional distribution can be applied to distinguish between the particle species or, to simplify the analysis method, one can project the linearized ΔE-E distribution on the y-axis. This has been done in figure 3.5 where the projection is denoted as ξ.

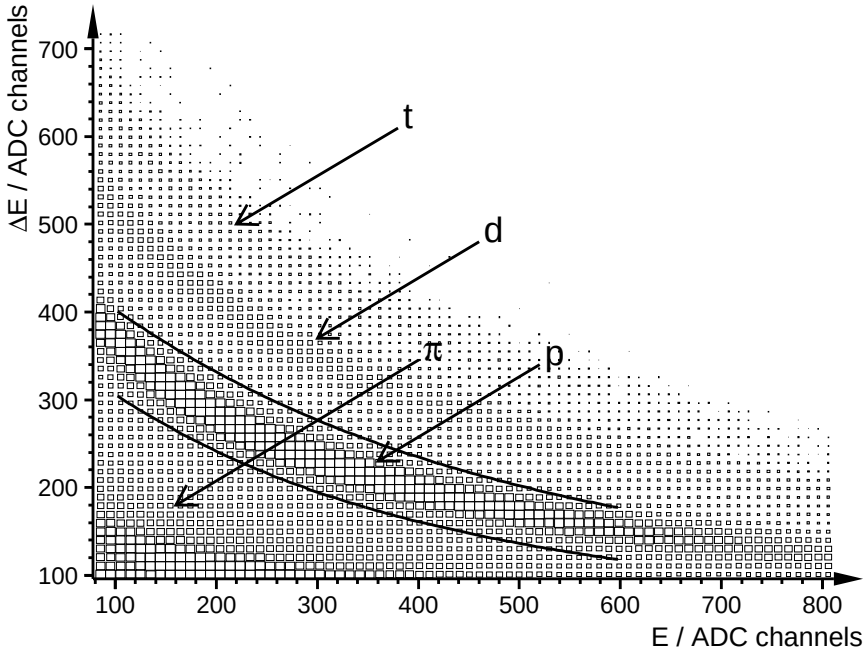

Figure 3.4: The energy loss versus the energy of all hits in the 520 backward modules of the Plastic Ball. The bands for p, d, and t are clearly visible; the π accumulate below the proton band. The solid lines indicate a graphical cut for the protons.

The linearization function used is:

$$\xi = \log(1.95 * \Delta E) + 0.95 * \log(E + 0.5 * \Delta E) - 11.122605 \tag{3.12}$$

Clear peaks are visible for p, d, and π hits in the resulting spectrum. A Gaussian is fitted to the ξ distribution and a 3σ cut is applied to distinguish the particles, as shown for example for the protons in figure 3.5. The positively charged pions are identified by their additional decay signal as described in section 2.5.

All particle cuts are given in table D.1. They are optimized for the flow analysis with fragments. In order to gain as many protons as possible a 3σ cut is used. To examine the influence of possible background contamination stronger cuts of 1σ, 1.5σ, and 2σ are studied. For the flow analysis no influence from the background of misidentified particles was detectable (see appendix D.2).

Alternatively different linearization functions could be used, e.g. to optimize the π^+ identification. Thus in former studies with the Plastic Ball in the WA80 experiment for azimuthal correlations [Awe96, Lis94] as well as for two particle correlations [Awe95, Blu93] another method of straightening the particle bands was used. This method has also been tested within this work but did not improve the results (see appendix D.3).

The resulting number of identified protons per event N_p in the Plastic Ball backward region is given in figure 3.6. The right part (b) shows the spectrum for minimum bias events. On average the number of protons is $\langle N_p \rangle \approx 6.5$. The distribution is nearly Gaussian but with a small tail to higher N_p. Only rare events have

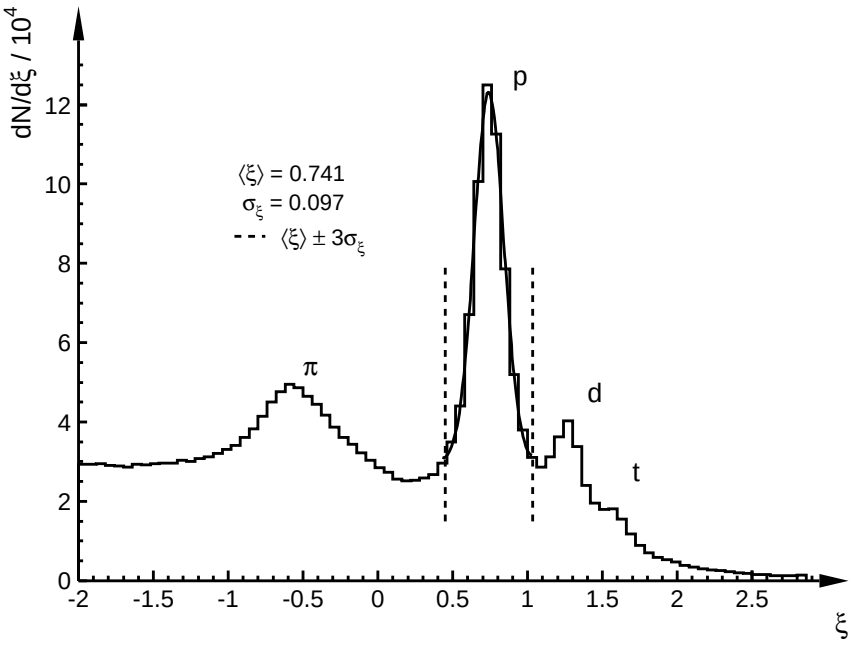

Figure 3.5: The linearized ΔE-E distribution ξ. Visible are the peaks for π, p, d, and t. The solid curve is a Gaussian fit on top of an exponential distribution with the denoted parameters. The dashed lines represent the applied proton cuts.

a number of about 20 identified protons. This could be due to not completely eliminated pile-up events, but since this is less then $0.04\,\%$ they do not influence the flow analysis. The left part of figure 3.6 reflects the centrality dependence of $\langle N_p \rangle$. In events with few participants the expected number of detected protons is low. Going to more central collisions $\langle N_p \rangle$ increases with the number of participants W_N. For nearly head-on collisions the double hit probability becomes large and thus the particle identification efficiency decreases. This can be seen in figure 3.6 a), where $\langle N_p \rangle$ saturates for large W_N values. Since the detector efficiency is not known exactly the given proton multiplicity corresponds to an effective and not to the true number of protons. This effective number of protons is used in the analysis. The average number of identified π^+, d, and t per event is $\approx$ 6.5, 2.7, and 1.4 respectively. Due to the background of unidentified or misidentified hits the absolute particle multiplicity is not exactly known.

3.3.3 Acceptance

Figure 3.7 shows the Plastic Ball acceptance, that is the region covered by the detector in which particle hits can be measured, for the four different particle species π^+, p, d, and t. Since the Plastic Ball measures in the target rapidity region, the rapidity is centred around 0. The shape of the p_T versus y distribution is similar for all particles types. Protons can be detected in a larger y range but with smaller transverse momentum p_T than e.g. deuterons.

The energy spectra for the four particle species are displayed in figure 3.8. The uncorrected dN/dE

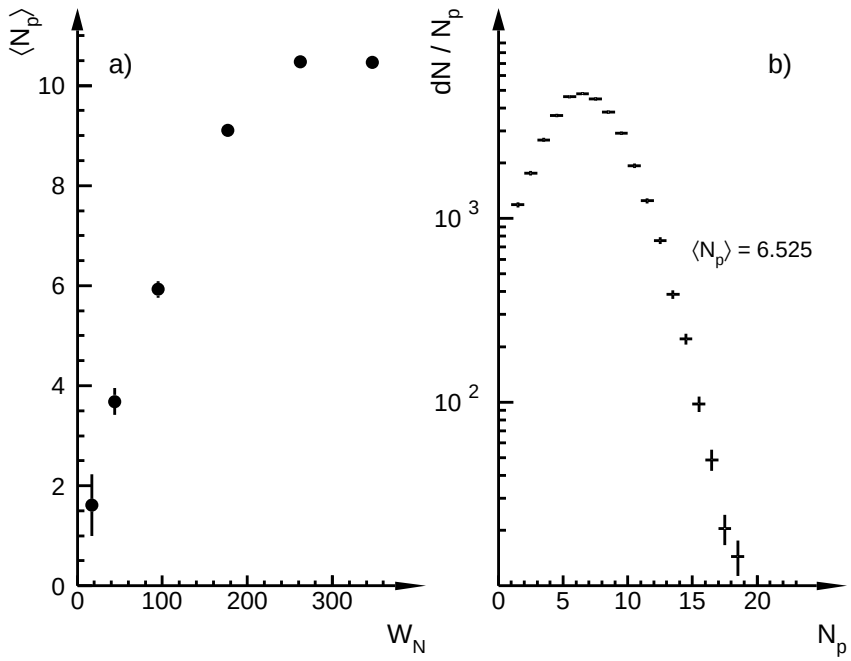

Figure 3.6: The average number of identified protons per event $\langle N_p \rangle$ as function of the number of wounded nucleons W_N a). The minimum bias distribution of N_p is given in b).

distribution is given for identified particles without additional energy cut. The energy cuts are, together with the particle identification cuts, listed in table D.1.

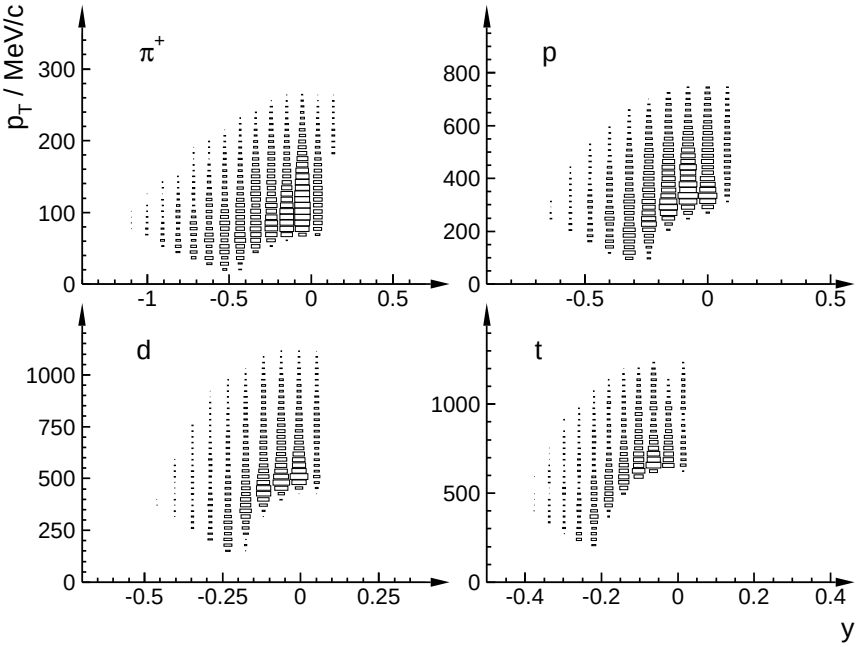

Figure 3.7: The Plastic Ball acceptance for pions (top left), protons (top right), deuterons (bottom left), and tritons (bottom right). Given is the transverse momentum p_T of every identified particle versus its rapidity y.

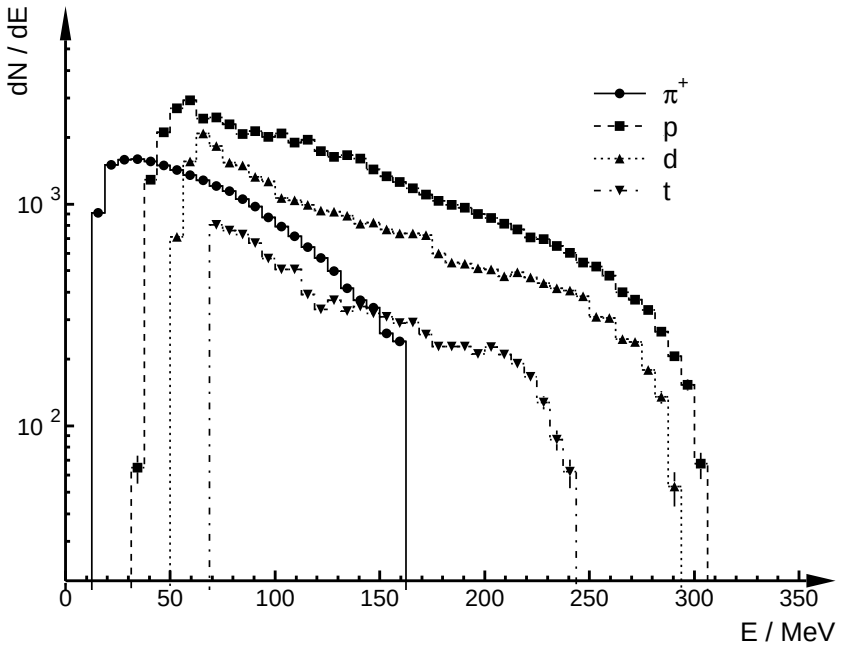

Figure 3.8: The Plastic Ball energy spectra for pions, protons, deuterons, and tritons.

4. Azimuthal Event Shape

While chapter 3 was providing the physics variables, this chapter will describe how the Plastic Ball is used to determine the reaction plane on an event-by-event basis. Since the Plastic Ball detector provides full azimuthal coverage in the target fragmentation region it is ideal for the event shape analysis. The definition and different evaluation methods for the event plane are presented in section 4.1. Section 4.2 will discuss the results on the determination of the reaction plane.

4.1 Reaction Plane Event by Event

In a heavy ion collision as shown in figure 4.1 two nuclei hit each other with the distance $|\vec{b}|$, where $\vec{b}$ is called the impact parameter. The figure reflects the collision in the centre-of-mass frame. The projectile is flying into the drawing plane, i.e. in positive $\vec{z}$ direction, while the target is coming out of this plane, i.e. in direction opposite to $\vec{z}$. Thus the axis denoted by $\vec{z}$ is the beam axis. The magnitude of the impact parameter varies between zero and the maximum distance R of the two nuclei. Here is $R = R_t + R_p$, where R_t and R_p are, in this picture of simple solid spheres, the radii of the target and the projectile nucleus, respectively.

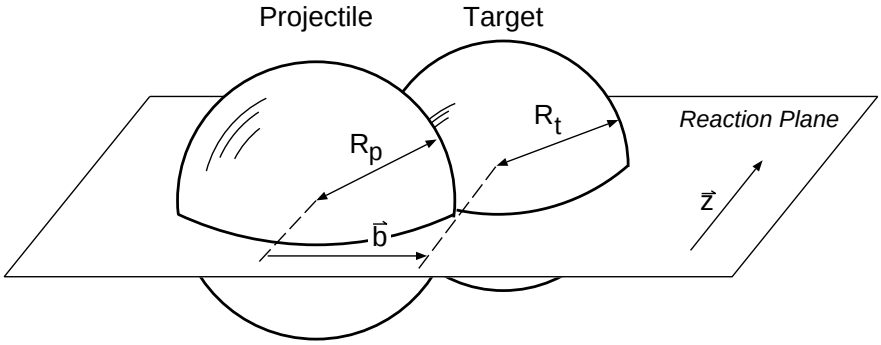

Figure 4.1: A sketch of a semi-central collision in the centre-of-mass frame. The beam axis, denoted as $\vec{z}$, and the the impact parameter $\vec{b}$ span the reaction plane.

The sketch represents a semi-central collision and the reaction plane is defined by the impact parameter $\vec{b}$ and the beam axis $\vec{z}$. In the limit of a head-on collision, where $|\vec{b}| \to 0$, the reaction plane is not defined. For distances $|\vec{b}| \geq R$ the reaction plane is defined but no collision takes place.

In actual $\mathrm{Pb} + \mathrm{Pb}$ collisions the direction of the impact parameter $\vec{b}$ varies from event to event. The orientation of the reaction plane in the laboratory frame can be determined by the measurement of the direction of the target spectator fragments since they tend to remain in the plane. This information is provided by the Plastic Ball since it detects the fragments in the target rapidity region. Since pions measured in the Plastic

Ball preferentially come from the hot source of participants instead of the spectator region they are not used for the determination of the plane. In the following subsections different methods, which can provide the reaction plane orientation, are presented.

4.1.1 Sphericity Method

Historically, the reaction plane was determined by the three-dimensional sphericity method. In this case the kinetic energy flow tensor F_{ij} was calculated according to equation 4.1 for each event separately.

$$F_{mn} = \sum_{i=1}^{N} p_i^m \, p_i^n \, w_i \qquad m,n = x,y,z \tag{4.1}$$

The sum runs over all N identified particles in the event. $p_i^{m,n}$ are the components of the momentum vector of each particle i, and m, n are the Cartesian coordinates in the centre-of-mass frame. w_i is a weight factor chosen in such a way that composite particles have the same weight per nucleon as the individual nucleons in the composite particle. The weight has most commonly been chosen as $1/p_i$ as in reference [Cug82], or $1/2m_i$ for the kinetic energy flow tensor, e.g. in [Gut90, Gyu82]. The tensor F_{mn} is symmetric by definition, thus it reduces the four-momenta information of all particles to six independent variables. These are the three eigenvalues and three Euler angles, obtained by diagonalizing the tensor. They describe the

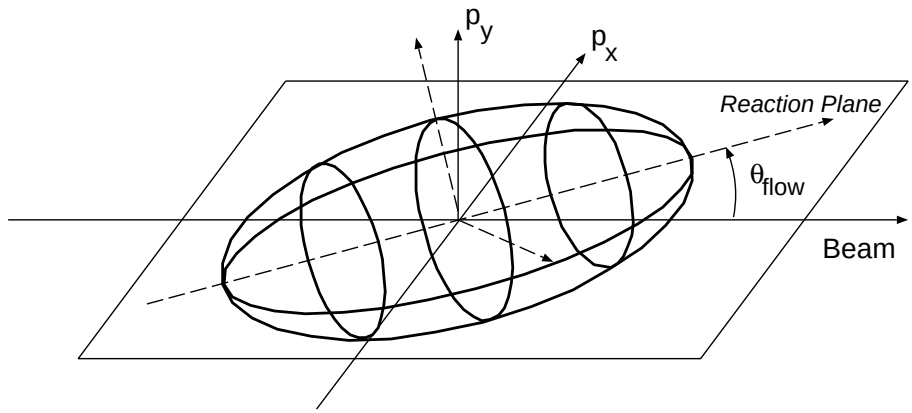

Figure 4.2: The reaction plane and the flow angle θ_{flow} defined by the beam axis and the major axis of the three-dimensional momentum flow ellipsoid. Figure adopted from [Gut90]

shape and the absolute orientation of an ellipsoid, respectively [Kam89].

This ellipsoid is schematically shown in figure 4.2. The flow angle θ_{flow} is defined by the beam axis, which is the $\vec{z}$ direction in the laboratory frame, and the eigenvector $\vec{e}_3$, the direction of the largest eigenvalue of the ellipsoid. The reaction plane is defined in this picture by the eigenvector $\vec{e}_3$ and the beam axis. Hence θ_{flow}, defining the major axis of the ellipsoid, lies in the reaction plane.

At ultrarelativistic energies, the flow angle will be approximately $\theta_{flow} \approx 0°$, due to the high forward momentum. Thus we are only interested in the transverse direction. For the azimuthal analysis the use of

the two-dimensional sphericity tensor $F^{\perp}_{mn}$ was suggested [Oll92]. In the transverse plane it is defined as:

$$F^{\perp}_{mn} = \sum_{i=1}^{N} p^{m}_{T,i}\, p^{n}_{T,i}\, w_i \tag{4.2}$$

The sum runs again over all N identified particles in the event and $p^{m,n}_{T,i}$ are the components of the transverse momentum vector $p_{T,i}$ of each particle i. The weight w_i is chosen in [Oll93] as the transverse energy $E_{T,i}$, since collective flow usually results not only in a larger number of particles, but also in a higher energy per particle in the flow direction. However, in [Vol96] $w_i = r_i/p^2_{T,i}$ is used, i.e. without the transverse energy weight. Note that here the azimuthal component of the energy of each particle $E_{T,i} = E_i \sin\theta_i$ is meant which is different from the global transverse energy E_T as defined by equation 2.1.

4.1.2 Transverse Momentum Method

The transverse momentum method was introduced in [Dan85]. It assumes that the reaction plane is defined by the beam axis and the vector $\vec{Q}$, which is defined as the sum of the transverse momenta $p_{T,i}$ of all N particles indexed by i:

$$\vec{Q} = \sum_{i=1}^{N} p_{T,i}\, w_i \tag{4.3}$$

The most common choice for the weight factor w_i is:

$$w_i = \begin{cases} +1 & y > y_{cm} + \delta \\ 0 & y_{cm} - \delta \le y \le y_{cm} + \delta \\ -1 & y < y_{cm} - \delta \end{cases} \tag{4.4}$$

The δ parameter has been introduced to avoid including particles near midrapidity y_{cm} which have small event plane signal but would add random fluctuations to the calculation [Cha97, Cro97, Gut89a]. However, other weights with $\delta = 0$ [Awe96, Wil92] or $w_i = y - y_{cm}$ [Fai87] have also been used, where the latter one gives greater weight to particles at higher rapidity. Momentum conservation requires that there is no absolute flow in momentum, hence the negative weight of the below midrapidity particles is mandatory so that the above midrapidity signal is not canceled out. Thus $\vec{Q}$ is a measure for the transverse momentum transfer between the forward and backward hemispheres.

4.1.3 Fourier Analysis Method

Both, the sphericity and the transverse momentum method achieve comparable results in extracting the reaction plane information [Gut90]. More generally, event shapes are parameterized in terms of the Fourier coefficients of the azimuthal particle distribution [Oll95, Vol96]. For each event, one defines the n^{th} Fourier coefficient $\vec{Q}_n$ as:

$$\vec{Q}_n = \sum_{i=1}^{N} w_i\, e^{in\phi_i} \tag{4.5}$$

N is the total particle multiplicity and ϕ_i is the azimuthal angle of the particle i. The weight w_i is most commonly taken as the transverse energy $E_{T,i}$ of the particle [Bar94, Hem96] or as the transverse momentum $p_{T,i}$ [Tsa93]. However, studies of particle number flow, i.e. choosing the weight factor $w_i = 1$, were also performed [Agg97a, Hee96, Woo98]. When taking a weight of $w_i = p_i^2/2m_i$, where p_i and m_i are the momentum and the mass of the particle i respectively, the analysis of the second coefficient $\vec{Q}_2$ becomes equivalent to the above discussed kinetic flow tensor F_{mn}.

In the analysis presented here the weight $w_i = E_{T,i}$ is applied to determine the reaction plane. However, another independent analysis of the WA98 Plastic Ball data using $w_i = p_{T,i}$ found the same result [Agg98b]. The Fourier coefficients can then be written as:

$$\begin{aligned} \vec{Q}_n &= (Q_n^x, Q_n^y) \qquad \text{with} \\ Q_n^x &= \sum_{i=1}^{N} E_{T,i} \cos(n\phi_i) \\ Q_n^y &= \sum_{i=1}^{N} E_{T,i} \sin(n\phi_i) \end{aligned} \tag{4.6}$$

The orientation of the reaction plane in space, given by the azimuthal angle Φ, can then be calculated from the data for each event separately:

$$\Phi = \arctan\left(\frac{Q_1^y}{Q_1^x}\right) \tag{4.7}$$

This corresponds to the dipole moment ($n = 1$) of the transverse energy distribution and $\vec{Q}_0$ is within this description the transverse energy vector $\vec{E}_T$. The azimuthal angle Φ and the magnitude of the transverse energy vector $|\vec{E}_T| = \sqrt{(Q_0^x)^2 + (Q_0^y)^2}$ define the azimuthal event shape and are therefore often referred to as directivity [Bar97a, Hua97], although slightly other definitions for the directivity exist [Ala92, Bec87, Boc88, Vol96]. The quadrupole moment corresponds to the values for $n = 2$, it describes the elliptical deformation of the particle distribution. It has been found that the contribution of higher moments is compatible with zero at lower energies [Bar97b, Rei97]. At SPS energies the authors of [Pos98] emphasize that higher harmonics could play an important role since there are physics processes like shadowing of the produced pions by co-moving fragments which could result in higher moments of the distribution. Because in this analysis mainly spectator fragments are used to determine the reaction plane, moments larger than $n = 2$ are assumed to negligible and thus not studied.

4.2 Results

4.2.1 Φ Distribution

The distribution of the reaction plane angle Φ is shown in figure 4.3 a). All identified fragments, i.e. p, d, and t, are used for the event plane determination. According to equations 4.6 the transverse energy weighted

Fourier coefficients $Q_n^{x,y}$ are calculated. A minimum number of four fragments per event is required because, although the physical event shape might be isotropic, events with low multiplicity will obviously appear anisotropic. This finite multiplicity effect has to be taken into account when estimating quantitative results. In section 4.2.4 this will be discussed by estimating the reaction plane resolution [Agg98b, Oll98]. Φ is derived from the Fourier coefficients as described in equation 4.7. Detector effects, which would result in preferred directions of Φ, can be excluded on a $2\,\%$ level. This is indicated in the figure by the dashed lines, which represent $2\,\%$ deviations from a flat distribution.

4.2.2 Subevent Analysis

How well Φ, and thus the reaction plane, is defined is analyzed with the subevent method [Dan85, Oll97, Pos98]. For this method each event is randomly divided into two subevents. One event means here all particles N, which are used for the reaction plane determination, as for example all fragments. The N particles are randomly rearranged into two subevents (A, B) of $N/2$ particles each[1]. For both subevents the reaction plane angles Φ_A and Φ_B are determined in the same manner as Φ is calculated. Since the statistic in the subevents is naturally less than in the full event the required minimum number of particles in each subevent is decreased from four to three. This means for the subevent reaction plane determination

[1] For odd numbers N the number of particles in the two subevents are $(N+1)/2$ and $(N-1)/2$.

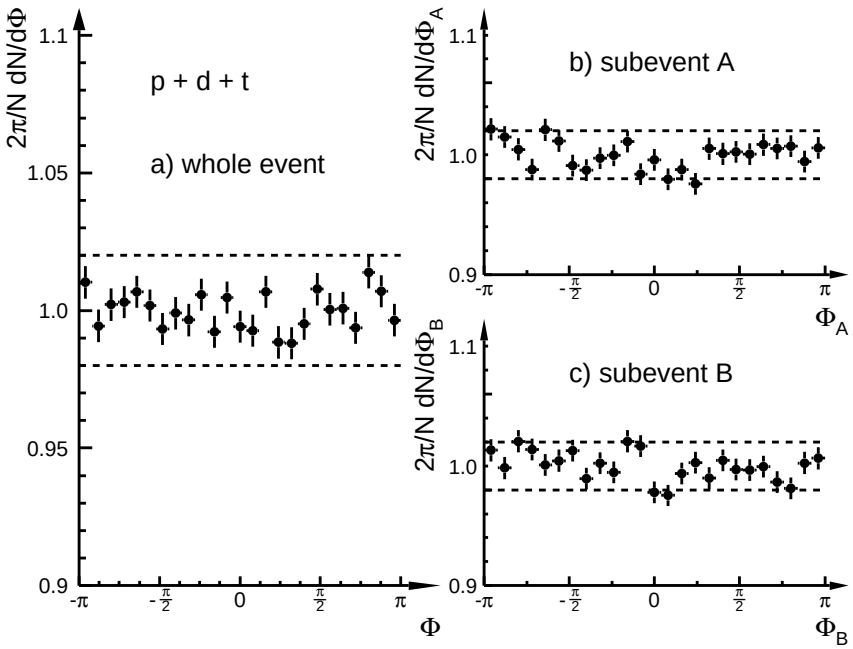

Figure 4.3: The distribution of the reaction plane angle Φ, calculated from all fragments (a). The right part (b + c) of the figure shows the $2\pi/NdN/d\Phi$ distributions for the two randomly selected subevents (see text for explanation). The dashed lines represent a deviation of $2\,\%$.

a minimum number of six fragments per event is necessary. The distribution of Φ_A and Φ_B is displayed in figure 4.3 b) and c), respectively. The $2\pi/N dN/d\Phi$ distribution for both subevents is also flat on a $2\,\%$ level.

To check the quality of the reaction plane definition, correlations between the two subevent angles are studied. If Φ really reflects the azimuthal shape of the event, the two subevent angles should be correlated. This is seen to be the case in figure 4.4. The two dimensional correlation qualitatively displays the fact that

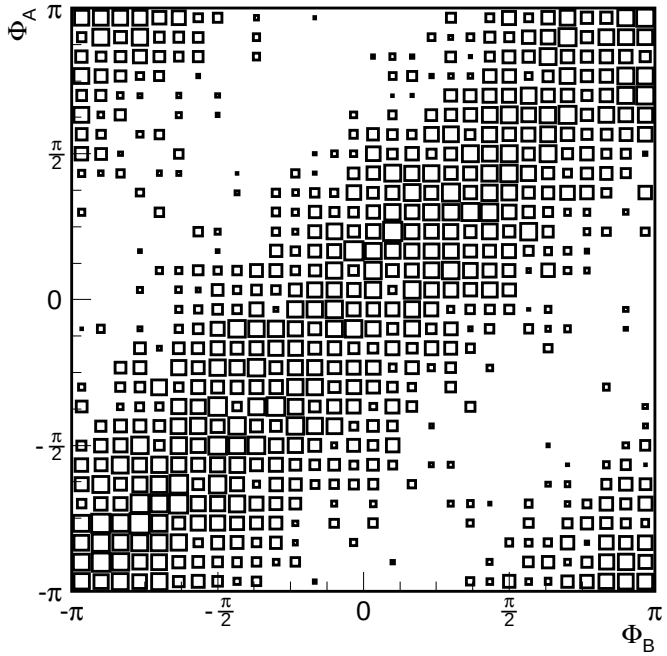

Figure 4.4: The reaction plane angle Φ_A of subevent A versus the angle Φ_B of subevent B. The correlation is shown for semi-central events, i.e. $20-40\,\%\,cs$ (see section 3.1).

the event plane can be measured using equation 4.7.

A more quantitative way to describe the correlation between the two subevents is to look at the distribution of the difference angle $\Delta\Phi = \Phi_A - \Phi_B$ between the two *subplane* angles. In figure 4.5 the $2\pi/N dN/d\Delta\Phi$ distribution is presented for two centrality classes, for semi-central ($20-40\,\%\,cs$) and for central events ($0-10\,\%\,cs$). The distribution is symmetric and centred around a maximum at zero. A strong correlation is evident for semi-central events while for central events the effect is weak. In other words, the fragments are emitted in a preferred direction relative to the reaction plane in not so central events, while central collisions seem to emit fragments mostly isotropically. This measured anisotropy is a signature of collective sideward flow in Pb on Pb collisions at SPS energies.

The data are fitted with the function [Kur98, Nis97]:

$$\frac{2\pi}{N}\frac{dN}{d\Delta\Phi} = 1 + \chi\cos\Delta\Phi \tag{4.8}$$

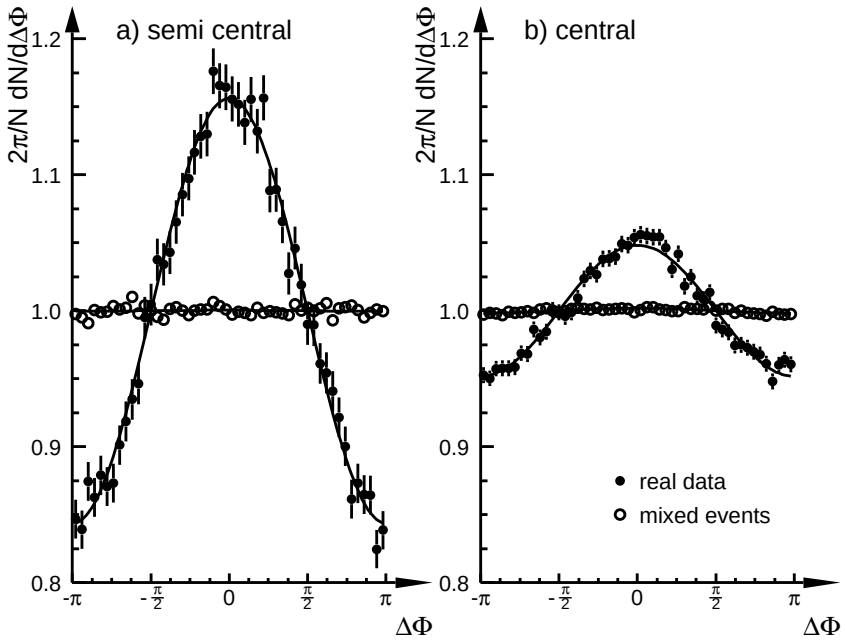

Figure 4.5: The difference angle $\Delta\Phi = \Phi_A - \Phi_B$ of the two subevents for semi-central (a) and central (b) events. The solid curve represents a cosine fit according to equation 4.8. The open symbols are obtained from mixed events.

For semi-central events the correlation strength is of the order of $15\,\%$ ($\chi = 0.156 \pm 0.37 \cdot 10^{-3}$). For pure correlations a Gaussian shape is expected, however, for correlations of this magnitude, this fit form is valid [Agg98b]. The dependence on centrality of the fit parameter χ will be discussed in section 4.2.3.

Additionally, figure 4.5 includes the result for mixed events, which are constructed to check for possible detector effects distorting the signal. We assume that the correlation between two randomly selected subevents is only due to the azimuthal event shape. Detector effects like incorrectly calibrated or singer modules, however, could mimic an azimuthal anisotropy. This anisotropy would show up in every event as well as in every subevent. Therefore the difference angle $\Delta\Phi$ would show a correlation for subevents from different real events. To check this, mixed events are created by using subevents from different real events. Differences in the phase space distributions are taken into account by only mixing equal size subevents from events of the same centrality class. The result, given in figure 4.5 as open symbols, is compatible with zero, which confirms that detector effects are negligible. An effect of the finite detector granularity is that in the real data two identified particles cannot be found in the same module. In mixed events this is a priori not forbidden. Thus the artificial anti-correlation due to an excluded module in real data is not taken into account by the above described mixed events. If mixed events are evaluated with the requirement of the excluded module a weak anti-correlation in the $\Delta\Phi$ distribution is observed [Agg98b]. However, this effect is small, typically of the order of $1 - 2\,\%$, and is assumed to be negligible.

Instead of using all fragments the same analysis was also performed for only protons, as shown in figure

4.6. As expected, the subevents are also strongly correlated for semi-central events, though the effect is

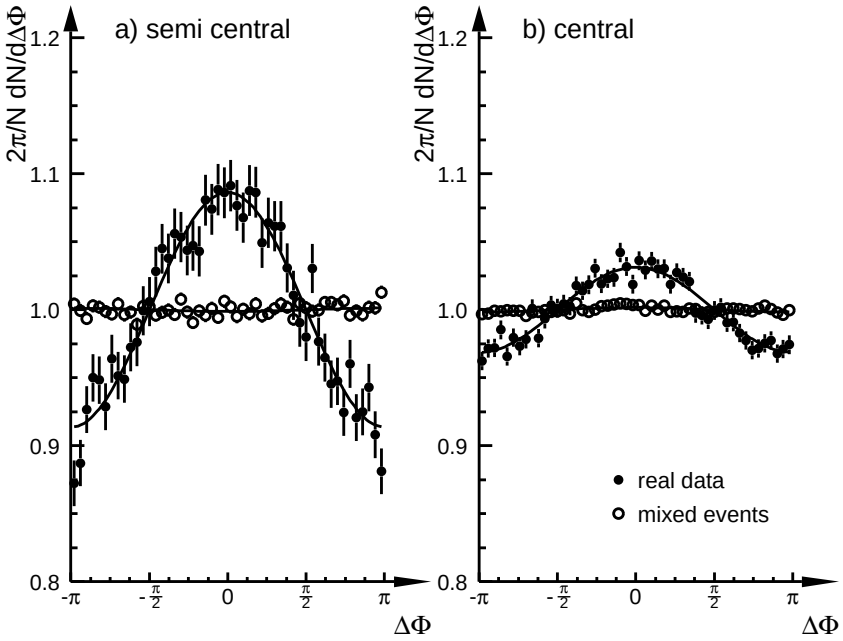

Figure 4.6: Same as figure 4.5, but for only protons instead of all identified fragments.

significantly smaller than for subevents using all fragments (see figure 4.5). Thus it was decided to use all fragments for the determination of the reaction plane angle Φ.

Alternatively, subevents can be constructed in a way that defines one subevent as all identified protons and the other one as all identified pions. The result of the pion to proton correlation is shown in figure 4.7. This is evidently a different behaviour, since the $\Delta\Phi$ distribution is still centred and symmetric around zero, but the maximum appears at $\pm\pi$. This means the angle of the pion subplane is anti-correlated to the one of the protons. Or, in other words, the pions are preferentially emitted in the opposite direction to the protons. This effect, termed anti-flow [Jah94], is discussed in more detail in the following chapters.

4.2.3 Dependence of χ on Centrality

In figure 4.5 it was already evident, that the strength of the correlation between the two subplane angles depends on the centrality of the event. This in turn means that the strength of the directed flow effect is a function of centrality. The strength is here described in terms of the fit parameter χ as defined in equation 4.8.

The evaluation of χ was done for all six centrality classes as defined in section 3.1. The same analysis was also performed for the mixed events. Figure 4.8 shows the strength of the correlation χ as a function of centrality in number of wounded nucleons W_N. The centrality has also been converted to an impact parameter scale as shown on the top of the figure. For the real data χ increases from peripheral events up to

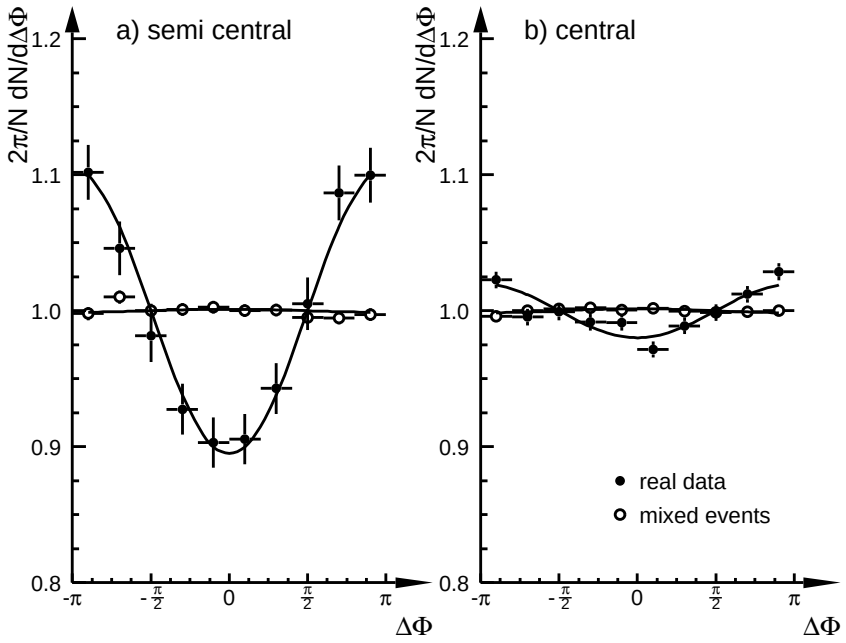

Figure 4.7: Same as figure 4.5, but for the correlation of the proton with the pion subplane. The centrality classes displayed here are $40-60\,\%\,cs$ (a) for semi-central and $10-20\,\%\,cs$ (b) for central events.

a maximum of $\chi = (0.156 \pm 0.37 \cdot 10^{-3})$ for semi-central collisions at $b \approx 8$ fm, which corresponds to a number of participants of $W_N \approx 180$. For central collisions χ decreases again to values less than 0.05. The result for mixed events is compatible with zero without any dependence on the centrality of the collision. The largest directed flow effect is therefore observed in semi-central collisions. At lower incident energies the same tendency of the impact parameter dependence is reported, but the maximum effect is observed to be at $b \approx 4$ fm [Cro97, Rei98], even though comparable symmetric systems (Au + Au) were studied.

Additionally, predictions from the Relativistic Quantum Molecular Dynamics model (RQMD), version 2.3 [Sor95], for the correlation strength are included in figure 4.8. For this comparison the RQMD data were filtered through the Plastic Ball acceptance and the same subevent analysis as for real and mixed events was performed [Agg98b]. Although the same functional dependence is obtained for RQMD data, the model overpredicts the absolute magnitude of the correlation strength by a factor of approximately 2. The measured data have not been corrected for the reaction plane resolution (see section 4.2.4).

As expected the dependence of the proton correlation on centrality is comparable with the result for all fragments (figure 4.9). For semi-central collisions, where again the maximum is found, χ increases to a value of $(0.086 \pm 0.36 \cdot 10^{-2})$. Thus the correlation is not as strong as the correlation for all fragments, where the effect is greater than $15\,\%$.

A different functional relation between the fit parameter χ and the number of participants W_N is observed for the π^+ to p correlation (figure 4.10). The maximum anti-correlation of $\chi = (-0.131 \pm 0.86 \cdot 10^{-2})$

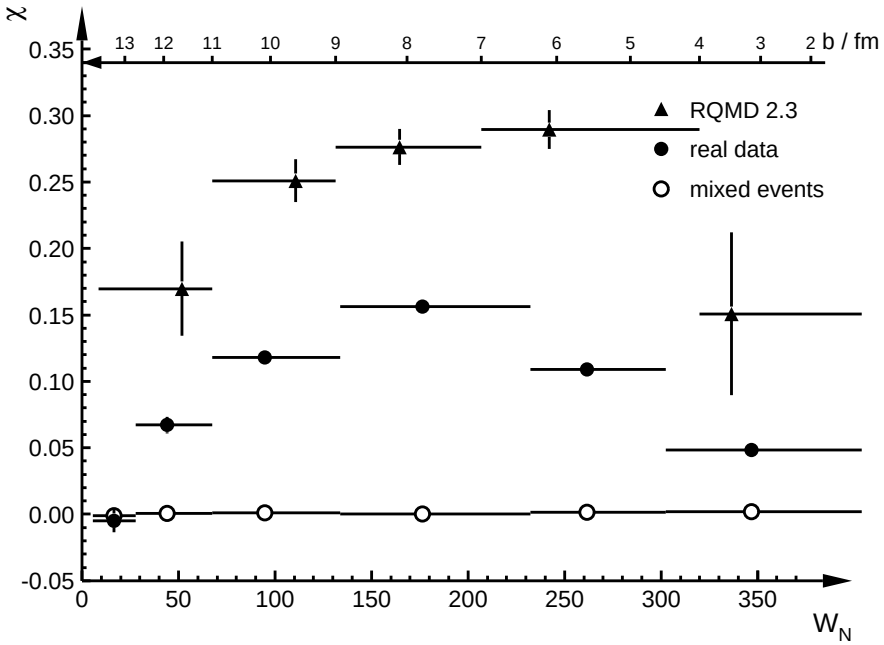

Figure 4.8: The dependence of the correlation strength χ on the centrality in number of participants W_N. The filled circles represent the real data, open symbols are for event mixing and the triangles are derived from RQMD predictions as shown in [Agg98b].

is of the same order of magnitude as the correlation of the fragments. However, this maximum is reached in more peripheral events for impact parameters of $b > 10\,\mathrm{fm}$. Contrary to the fragment correlation, the strength of this effect does not decrease when going to even larger impact parameters, even here a $10\,\%$ effect is still observable. Again RQMD 2.3 data are compared to the real data and the tendency is reproduced but the absolute value is also overpredicted by a factor of 2.

4.2.4 Reaction Plane Resolution

The flow measurements with respect to the reaction plane that will be presented in the following chapters assume a perfect event plane determination, i.e. that the angle Φ could be obtained from the data exactly. In reality, the finite number of detected particles produces a limited resolution in the measurement of the reaction plane angle. All observables $\mathcal{O}'$ that refer to the reaction plane must be corrected up to what they would be relative to the true event plane [Oll97].

This correction is done by dividing the observable $\mathcal{O}'$ by the event plane resolution defined as [Dan85]:

$$\sigma_{plane} = \langle \cos(\Phi - \Psi) \rangle \tag{4.9}$$

with the measured event plane angle Φ and the true angle Ψ. The true observable therefore is obtained as $\mathcal{O} = \mathcal{O}'/\sigma_{plane}$. The distribution of $(\Phi - \Psi)$ and thus the resolution can be written as a function of a single dimensionless parameter κ [Oll98]. The definition of κ is based on the fact that the central limit theorem

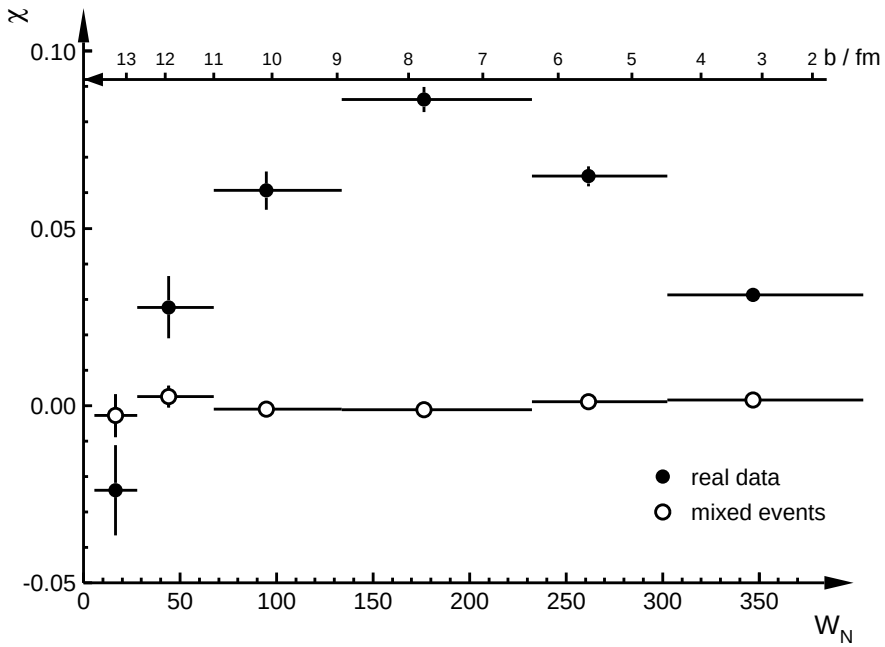

Figure 4.9: Same as figure 4.8, but for only protons instead of all identified fragments.

requires that the fluctuations of the event plane vector Q_1 form a Gaussian distribution. The average of this Gaussian is $\langle Q_1 \rangle$ and the width shall be denoted by σ. The ratio of these define the parameter $\kappa \equiv \langle Q_1 \rangle / \sigma$. In terms of κ the resolution becomes [Oll97]:

$$\sigma_{plane} = \langle \cos(\Phi - \Psi) \rangle = \frac{\sqrt{\pi}}{2} \kappa e^{-\kappa^2/2} \left[I_0(\frac{\kappa^2}{2}) + I_1(\frac{\kappa^2}{2}) \right] \tag{4.10}$$

where I_0, I_1 are the modified Bessel functions of the order of $0, 1$ respectively.

The value κ can be obtained from the data by comparing events with $|\Delta\Phi| > \pi/2$ to all events, where $\Delta\Phi$ is the difference of the two subevent angles [Bar94]:

$$\frac{N_{|\Delta\Phi| > \pi/2}}{N} = \frac{1}{2} e^{-\kappa^2/2} \tag{4.11}$$

This equation is valid for small κ.

Alternatively the reaction plane resolution can be estimated from the subevent correlation (section 4.2.2) as follows [Vol96]:

$$\begin{aligned} \langle \cos(\Delta\Phi) \rangle &= \langle \cos(\Phi_A - \Phi_B) \rangle \\ &= \langle \cos((\Phi_A - \Psi) - (\Phi_B - \Psi)) \rangle \\ &= \langle \cos(\Phi_A - \Psi) \cos(\Phi_B - \Psi) + \sin(\Phi_A - \Psi) \sin(\Phi_B - \Psi) \rangle \end{aligned}$$

When taking the average value the sine terms cancel out, because of the reflection symmetry of the Φ distribution. Therefore one obtains:

$$\langle \cos(\Delta\Phi) \rangle = \langle \cos(\Phi_A - \Psi) \rangle \langle \cos(\Phi_B - \Psi) \rangle$$

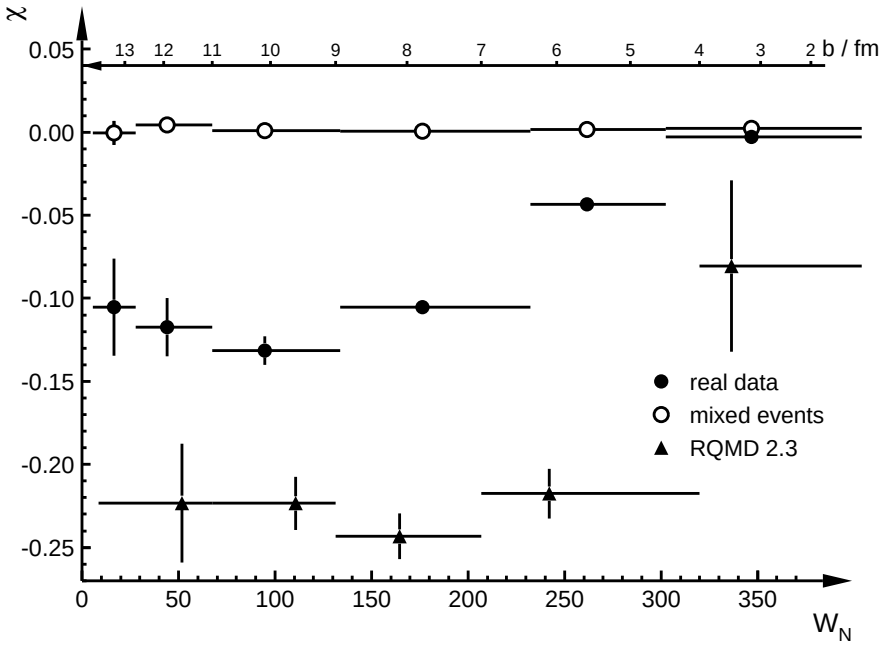

Figure 4.10: Same as figure 4.8, but for the strength of the correlation of the proton to pion subplanes.

$$= \langle \cos(\Phi_A - \Psi) \rangle^2$$
$$= \sigma^2_{subplane} \tag{4.12}$$

The second equation is valid since we assume, that for the subevents there are no other correlations except the ones due to directed flow. Then both subplanes are independent and provide the same resolution. The subplane resolution $\sigma_{subplane}$ is defined similarly according to equation 4.9. The resolution scales with the particle multiplicity like $\sqrt{N}$ and thus one obtains the resolution for the full event, which is twice as large as the subevents, as $\sigma_{plane} = \sqrt{2}\,\sigma_{subplane}$. Combining this with equation 4.12, the event plane resolution can be calculated directly from the experimental data, by applying the following equation to the subevent correlation distributions (as e.g. in figure 4.5):

$$\sigma_{plane} = \sqrt{2\,\langle \cos(\Delta\Phi) \rangle} \tag{4.13}$$

The definition of the fit parameter χ in equation 4.8 leads to:

$$\begin{aligned}
\frac{dN}{d\cos(\Delta\Phi)}\frac{d\cos(\Delta\Phi)}{d\Delta\Phi} &= 1+\chi\cos(\Delta\Phi) \\
\Rightarrow \quad \frac{dN}{d\cos(\Delta\Phi)} &= -\frac{1+\chi\cos(\Delta\Phi)}{\sqrt{1-\cos^2(\Delta\Phi)}} \\
\Rightarrow \quad \langle\cos(\Delta\Phi)\rangle &= \frac{-\int_{-1}^{1}\frac{\cos(\Delta\Phi)+\chi\cos^2(\Delta\Phi)}{\sqrt{1-\cos^2(\Delta\Phi)}}\,d\cos(\Delta\Phi)}{-\int_{-1}^{1}\frac{1+\chi\cos(\Delta\Phi)}{\sqrt{1-\cos^2(\Delta\Phi)}}\,d\cos(\Delta\Phi)} \\
\Rightarrow \quad \langle\cos(\Delta\Phi)\rangle &= \frac{\chi/2\,\pi}{\pi} \\
\Rightarrow \quad \sigma^2_{subplane} &= \chi/2
\end{aligned} \tag{4.14}$$

Hence the resolution of the subplanes is also provided by the fit to the $\Delta\Phi$ distribution. Thus one can obtain the resolution from the fit results in section 4.2.2 as $\sigma_{plane} = \sqrt{\chi}$, which in turn gives a consistency check on the resolution determined above. In reference [Pos98] an iterative method to solve equation 4.10 once the subplane resolution is known is proposed. To obtain the accurate correction factor this iteration

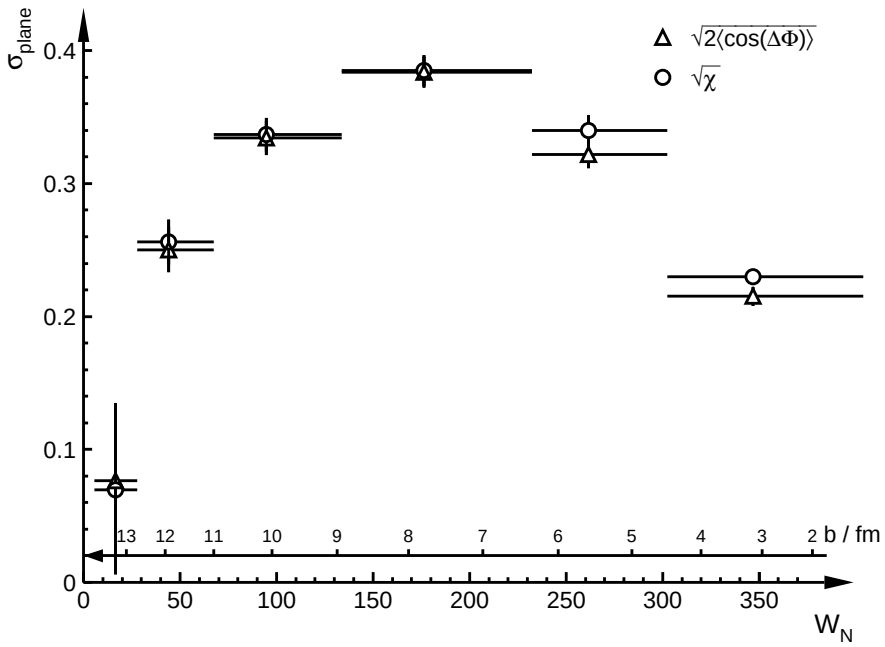

Figure 4.11: The event plane resolution dependence on centrality in terms of the number of wounded nucleons. The result of the average $\cos(\Delta\Phi)$ distribution is represented by the triangles. The circles display the result of the fit method.

(equation 23 in reference [Pos98]) is adopted and applied to the present data. The correction of flow values corresponding to the second moment is accordingly given by $\langle\cos(2\,\Delta\Phi)\rangle$. This requires the determination of the plane of the second harmonic, which corresponds to $n = 2$ in equation 4.6. The evaluated reaction

plane resolution σ_{plane}, however, provides also the correction factor for higher harmonics. The method to obtain this correction is given in [Pos98], typical values of this correction for $n = 2$ are of the order of 10.

In figure 4.11 the strong dependence of the event plane resolution σ_{plane} for $n = 1$ on the centrality is shown. As expected the behaviour is the same as for the fit parameter χ in figure 4.8. The event plane can be determined best for semi-central collisions. Here the flow effect is largest and the resolution has found to be $\sigma_{plane} = (0.384 \pm 0.018)$. The more isotropic the azimuthal event shape is, that is for more peripheral or more central collisions, the more difficult is the extraction of the reaction plane and the resolution gets worse. The figure presents the result for both above described methods. The triangles represent the resolution obtained from the average value of the $\cos(\Delta\Phi)$ distribution. These are in a good agreement with the result provided by the fit method, which is denoted by the circles in the plot.

4.2.5 Auto Correlation

Another effect of the finite multiplicity, which is taken into account, is the auto correlation effect. Naturally, there is a correlation between the azimuthal angle of a particle with respect to the reaction plane, if this particle is included in the evaluation of Φ according to equations 4.6 and 4.7. This correlation due to the finite particle multiplicity is of the order of $1/\sqrt{N}$ [Dan85], where the total particle multiplicity is denoted with N.

On the other hand, if particles which were not used in the event plane determination are studied, there would be no auto correlation effect. Therefore the auto-correlation can be avoided by calculating for each particle i the event plane angle of the remaining $N - 1$ particles [Awe97, Dan85]:

$$\begin{aligned}
\vec{Q}_n(i) &= (Q_n^x(i), Q_n^y(i)) && \text{with} \\
Q_n^x(i) &= \sum_{j=1, j\neq i}^{N} E_{T,j}\ \cos(n\phi_j) \\
Q_n^y(i) &= \sum_{j=1, j\neq i}^{N} E_{T,j}\ \sin(n\phi_j) && \text{and} \\
\Phi(i) &= \arctan\left(\frac{Q_1^y(i)}{Q_1^x(i)}\right) && (4.15)
\end{aligned}$$

The applied event plane resolution mentioned above is calculated for the subplanes according to equations 4.15 instead of equations 4.6 and 4.7, which means avoiding an auto correlation, the observable is then a true value. Therefore in the following this effect has always been taken into account.

5. Average Transverse Momentum

After the determination of the reaction plane, a directed flow analysis is performed, in which the average transverse momentum with respect to the reaction plane for different particle species is evaluated [Dan85]. The two dimensional distributions $d^2N/dp_{x'}dp_{y'}$ are obtained by decomposing the transverse momentum p_T of each identified particle into components with respect to the measured reaction plane:

$$p_{x'} = p_T \cos(\phi') \qquad p_{y'} = p_T \sin(\phi') \tag{5.1}$$

Here ϕ' is the azimuthal emission angle of the particle relative to the measured reaction plane. The measured reaction plane angle Φ consequently defines the positive x' direction.

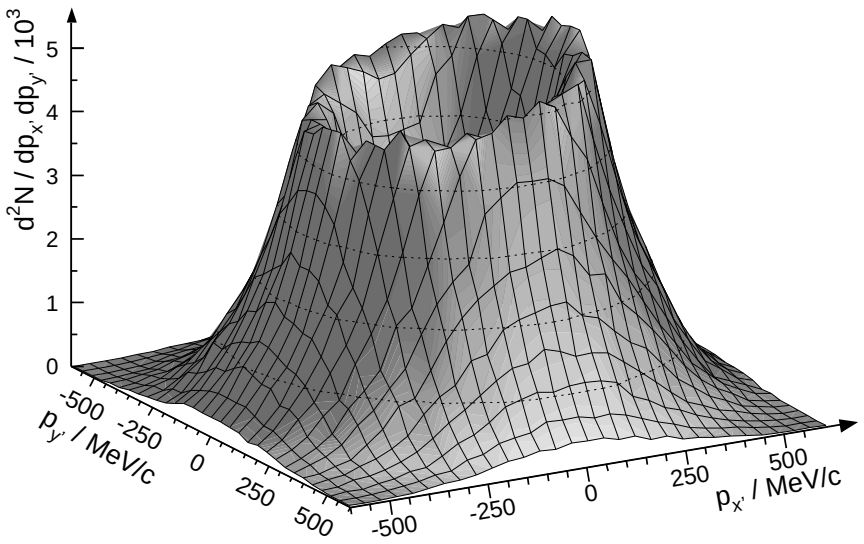

Figure 5.1: Surface plot of the $d^2N/dp_{x'}dp_{y'}$ distribution for protons detected in the Plastic Ball at the rapidity $y = -0.35 \pm 0.15$. The result is obtained for the centrality bin $20 - 40\,\%cs$.

The three dimensional distribution is displayed in figure 5.1. It shows $d^2N/dp_{x'}dp_{y'}$ for protons detected in the Plastic Ball at the rapidity $y = -0.35 \pm 0.15$. A clear azimuthal anisotropy is visible for the depicted result in the centrality range $20 - 40\,\%cs$. In the positive $p_{x'}$ direction, the yield of the momenta in the reaction plane is higher than in the opposite direction. This directed flow confirms the observation from the subevent analysis. The hole in the centre of the distribution reflects the detector acceptance as described in section 3.3.3.

In order to perform systematic studies of these $p_{x'}$ versus $p_{y'}$ distributions, they are evaluated for different centrality and rapidity bins and for all identified particle species. The left panel of figure 5.2 shows for instance the $d^2N/dp_{x'}dp_{y'}$ distributions for protons detected in the Plastic Ball at the rapidity

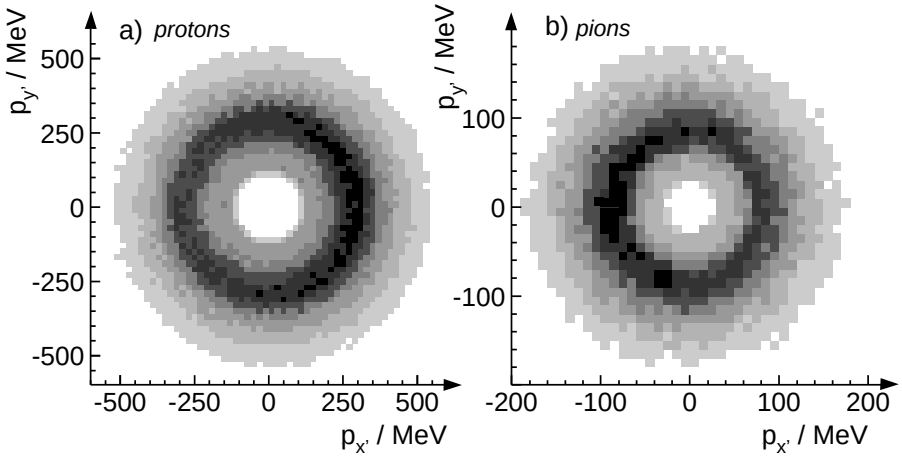

Figure 5.2: The differential cross section $d^2N/dp_{x'}dp_{y'}$ at the rapidity $y = -0.35 \pm 0.15$ for protons in the centrality range $20 - 40\,\%cs$ (a). And for pions at the rapidity $y = -0.2 \pm 0.2$ for π^+ within $60 - 80\,\%cs$ (b).

$y = -0.35 \pm 0.15$. For these semi-central collisions ($20 - 40\,\%cs$) an azimuthal anisotropy is visible. The yield is higher for momenta in the reaction plane in positive x-direction. I.e. the same direction observed for the fragment flow in the subevent analysis. The right part of figure 5.2 shows the same representation for π^+ identified in the Plastic Ball at the rapidity $y = -0.2 \pm 0.2$, in the centrality bin $60 - 80\,\%cs$. Again an azimuthal anisotropy is visible, however, contrary to the protons, the pions show a higher yield in the direction opposite to the fragment flow direction. The in-plane anti-flow of positively charged pions in the target fragmentation region, which was observed in the subevent correlation analysis (section 4.2.2), is confirmed. Comparable results have been reported for Au + Au collisions at AGS[1] energies [Ahl98], although the anisotropic pion emission could not be seen there with this method [Zha95].

Figure 5.3 displays the $d^2N/dp_{x'}dp_{y'}$ distribution for deuterons at rapidity $y = -0.3 \pm 0.2$ (a) and for tritons at rapidity $y = -0.1 \pm 0.3$ (b). The results were obtained for semi-central events ($20 - 40\,\%cs$). For the deuterons a clear azimuthal anisotropy is visible. The emission of these fragments is preferred in the same direction as the observed proton flow. If there is any anisotropy for tritons, which will be studied in the following, it is not easily perceivable at this level.

The observed directed flow is quantified by the transverse momentum transfer $\langle p_{x'} \rangle$. To obtain the average transverse momentum transfer in the reaction plane $\langle p_{x'} \rangle$ from the above described differential cross sections the experimental distributions are fitted with a two dimensional Gaussian. Since the momentum distribution obeys the Poisson statistics this approximation by a Gaussian distribution is valid. The true

[1] Alternating Gradient Synchrotron

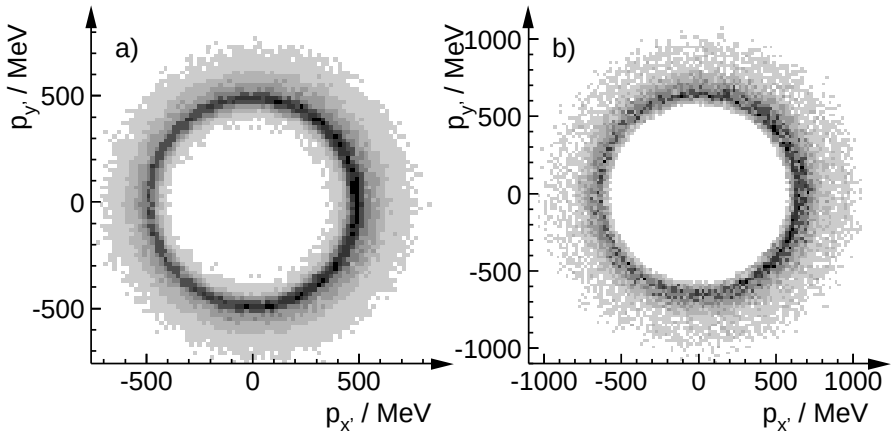

Figure 5.3: Same as figure 5.2. The $d^2N/dp_{x'}dp_{y'}$ distribution at rapidity $y = -0.3 \pm 0.2$ for deuterons (a) and $y = -0.1 \pm 0.3$ for tritons (b), both at the centrality $20 - 40\,\%cs$.

$\langle p_x \rangle$ is then derived from $\langle p_{x'} \rangle$, which is determined relative to the measured reaction plane, after making the event plane resolution correction according to (see section 4.2.4):

$$\langle p_x \rangle = \langle p_{x'} \rangle / \sigma_{plane} \tag{5.2}$$

The dependence of $\langle p_x \rangle$ for the different particle species on the rapidity as well as on the collision centrality and the incident beam energy E_{in} are presented in the following sections.

5.1 Dependence of $\langle p_x \rangle$ on Rapidity

As described above the transverse momenta of the fragments point to the same side as the flow angle Φ, thus the two dimensional Gaussian fit results in positive $\langle p_x \rangle$ values. By convention this same side emission gets a positive sign at projectile and a negative sign at target rapidities. For symmetric reaction systems like Pb + Pb the flow value of particles backward of midrapidity can be obtained by changing the sign of $\langle p_x \rangle$. This allows to compare the results measured forward of midrapidity to the values from the target fragmentation region. Consequently the average transverse momentum for π^+, which is negative from the fit result, is transformed to positive values.

Figure 5.4 displays the rapidity dependence of the average transverse momentum in the reaction plane for fragments (a) and pions (b). The error given includes the fit error as well as the error in the determination of the reaction plane. To study the systematic error of the fitting routine a simple Monte Carlo simulation has been performed, in which the double differential cross section with and without the typical acceptance hole in the centre was calculated. The error was found to be $11\,\%$. Furthermore possible effects due to background contamination, i.e. misidentified particles, are studied within the Monte Carlo simulation. The contribution of this effect is estimated to be $8.5\,\%$. Thus a total systematic error of less than $20\,\%$ was

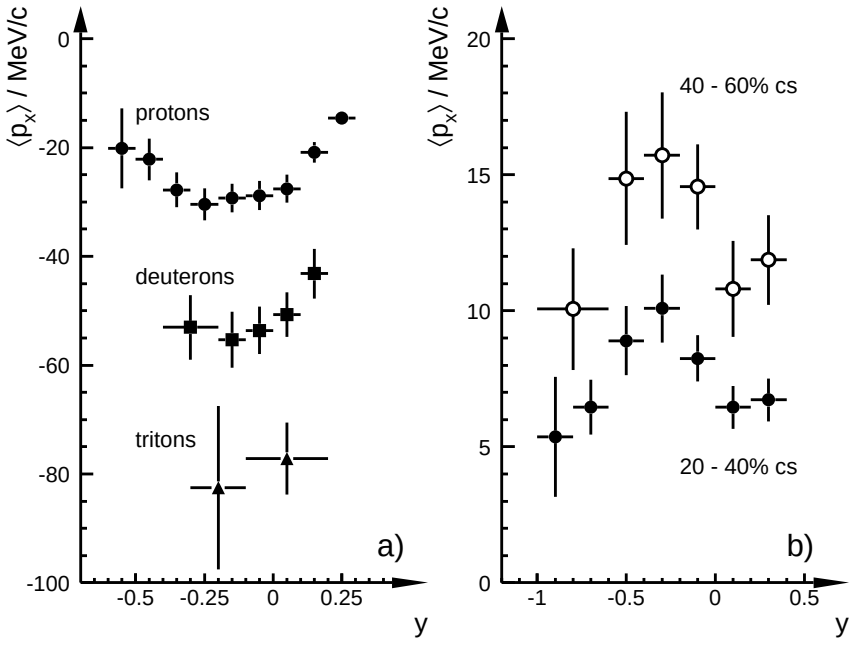

Figure 5.4: The average transverse momentum transfer $\langle p_x \rangle$ as function of the rapidity for the fragments p, d, and t (a) and pions (b) in the centrality class 20 - 40 $\%cs$. For pions additionally the centrality class 40 - 60 $\%cs$ is shown (open symbols).

obtained (see appendix E). This systematic error has not been included in this figure.

For protons the absolute magnitude of the average transverse momentum transfer increases with rapidity to a maximum of $|\langle p_x \rangle| \approx 30\,\mathrm{MeV}/c$ at $y \approx -0.25$ and decreases again for larger rapidities. The Plastic Ball acceptance also permits the determination of $\langle p_x \rangle$ of deuterons and tritons at rapidities of $-0.4 < y < 0.2$ and $-0.3 < y < 0.2$, respectively. Assuming that the directed flow of the fragments is only due to collective motion, one would expect that the average transverse momentum scales with the fragment mass. And in fact it has been found that the value for deuterons is approximately twice the value for protons in the same centrality and rapidity regions. Also the tritons have a maximum $\langle p_x \rangle$, which is slightly less than three times that of the proton $\langle p_x \rangle$. This behaviour is very similar to the one reported for 200 AMeV [Dos87, Gut89b] and 10 - 11 AGeV [Ahl98, Bar98b] incident energy collisions. There it was found that the mean transverse momentum projected onto the reaction plane of the light fragments scales with mass A for $A \leq 2$ very well, while the mass dependence gets slightly weaker for larger A. However, the maximum absolute $|\langle p_x \rangle|$ for protons in 158 AGeV Pb + Pb collisions turns out to be much smaller than found for Au + Au collisions (120 - 130 MeV/c) at incident energies of 200 AMeV [Gus88, Kam86] and 1 - 11 AGeV [Par95, Bar98b].

The observed pion signal however, is of about the same magnitude as reported for 11 AGeV Au + Au collisions [Bar97b]. It results, as mentioned above, in positive values for $\langle p_x \rangle$. The absolute magnitude is smaller than for protons by a factor of about three. The mean transverse momentum in the reaction plane

increases with rapidity up to a maximum at $y \approx -0.3$ with $\langle p_x \rangle \approx 10\,\mathrm{MeV}/c$. In contrast to protons even larger average transverse momentum transfers are observed in more peripheral events. This is displayed in figure 5.4 b) by the open symbols.

Comparison with RQMD

In figure 5.5 the average transverse momentum in the reaction plane of protons and pions is compared

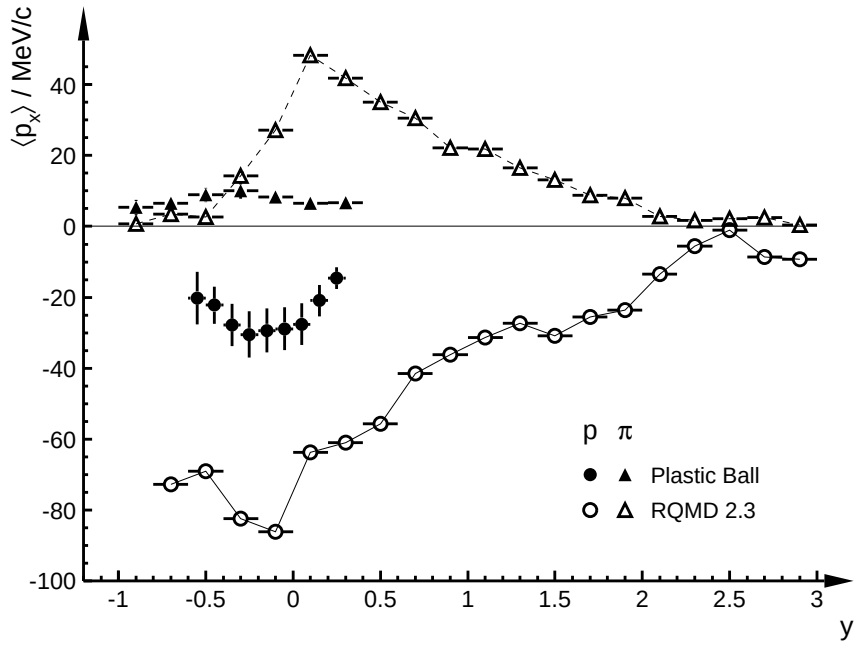

Figure 5.5: The average transverse momentum in the reaction plane $\langle p_x \rangle$ for protons and pions compared with RQMD predictions. The data (filled symbols) are for the centrality $20 - 40\,\%cs$, which is comparable to the impact parameter $b = 8 - 10\,\mathrm{fm}$ for the RQMD result (open symbols). The systematic errors are included in the data.

to calculations from the RQMD 2.3 model. The RQMD result is for the impact parameter range of $b = 8 - 10\,\mathrm{fm}$ [Agg98b], which corresponds approximately to the centrality class $20 - 40\,\%cs$ depicted in the figure. The estimated systematic error of $20\,\%$ on the data has been included. The simulations show the expected anti-symmetric behaviour around midrapidity ($y = 2.9$), but since all presented particles are measured backward of midrapidity, the result displayed in figure 5.5 is restricted to this range.

At AGS energies the RQMD model in cascade mode fails to describe the data, it underpredicts the $\langle p_x \rangle$. However, RQMD simulations including mean field effects describe the data rather well [Liu98]. For the present results the cascade mode was used, since the mean field effects are expected to be small at SPS energies. However, even cascade mode RQMD overpredicts the proton data by a factor of approximately three. For pions the same relation between the RQMD predictions and the data is observed. At AGS energies the $\langle p_x \rangle$ of pions is reproduced by the mean field mode RQMD, while in cascade mode RQMD underpredicts

the measured results [Bar97b]. For the studied 158 AGeV Pb + Pb collisions, however, even the cascade mode RQMD overpredicts the data.

Comparison with VENUS

In addition the measured $\langle p_x \rangle$ are compared to calculations with VENUS in version 4.12 [Wer93]. The generated VENUS events are analyzed in the same manner as real events, i.e. they are filtered through the Plastic Ball acceptance and all accepted protons were used to determine the reaction plane as described in chapter 4.1. Also a subevent analysis was performed to extract the resolution of the reaction plane for the simulated events. For all protons and pions the average transverse momentum was calculated for several rapidity bins with respect to the extracted reaction plane. The result is presented in figure 5.6. Since VENUS

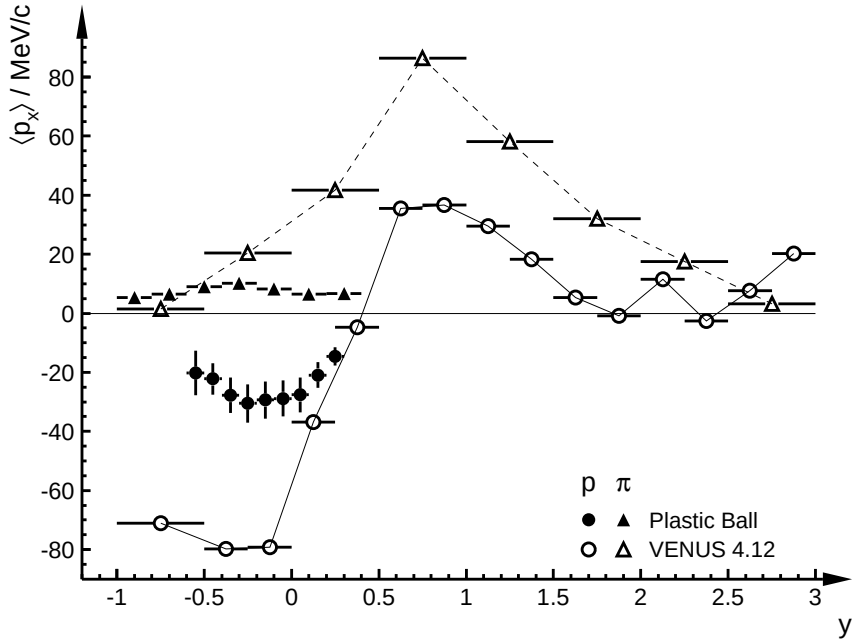

Figure 5.6: Plastic Ball data (filled symbols) for protons and pions in the centrality range $20 - 40\,\%cs$ compared with VENUS calculations for the impact parameter range $b = 8 - 10$ fm. The systematic errors are included in the data.

is a string model based calculation without the inclusion of pion absorption or resonances, it is expected to show no significant flow effects. The astonishing result however, is that at target rapidity the proton flow signal in terms of $\langle p_x \rangle$ exceeds the real data by a factor of approximately three and is thus comparable to the RQMD result presented above. The observed effect might be explained by the rescattering that is included in the VENUS model. In contrast to the RQMD predictions for protons, the VENUS results show a sharp increase of the average transverse momentum in the anti-flow direction and passes through zero at $y \approx 0.5$. This behaviour is seen in figure 5.6, where the $\langle p_x \rangle$ dependence on rapidity is shown for protons and also pions. The centrality region $20 - 40\,\%cs$ corresponds approximately to the impact parameter range

$b = 8 - 10$ fm of the VENUS calculations. The systematic error of $20\,\%$ is included in the given errors. The pion result from the VENUS simulation fails to describe the data.

5.2 Dependence of $\langle p_x \rangle$ on Centrality

Figure 5.4 b) indicated a significant difference of the pion average transverse momentum in the reaction plane for different collision centralities. The subevent analysis of chapter 4.2.2 revealed already the dependence of the flow effect on centrality for fragments and pions. A systematic study of the dependence of the flow signal on centrality for protons and pions in terms of $\langle p_x \rangle$ is displayed in figure 5.7. The average

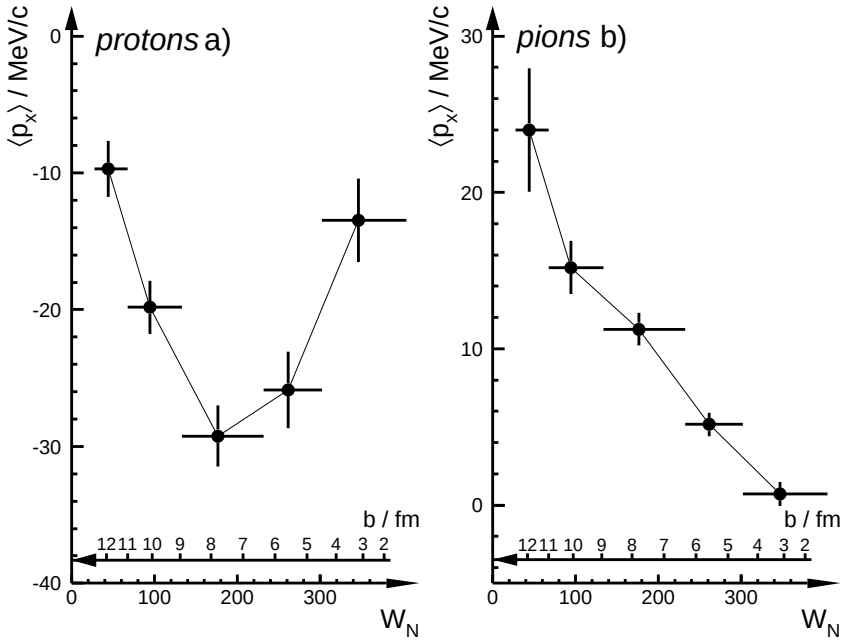

Figure 5.7: The average transverse momentum for protons a) and pions b) as function of W_N in the rapidity range $-0.4 \leq y \leq 0.1$ and $-0.6 \leq y \leq 0.0$ respectively.

transverse momentum in the reaction plane is obtained in the rapidity range $-0.4 \leq y \leq 0.1$ for protons and $-0.6 \leq y \leq 0.0$ for pions. The proton absolute momentum transfer in the reaction plane increases with the number of participants to a maximum $|\langle p_x \rangle|$ for semi-central collisions at $W_N \approx 180$. The corresponding impact parameter of $b \approx 8$ fm with maximum effect is twice as large as that found for Au + Au collisions at AGS energies [Rei97]. For more head-on collisions the $|\langle p_x \rangle|$ decreases again. In other words, the events with intermediate collision centrality show the largest flow effect, which is in agreement with the subevent analysis. In the limit of impact parameter zero the sideward flow must vanish, due to symmetry, as confirmed by the data. For the most peripheral collisions with $W_N < 25$, i.e. in terms of the impact parameter $b > 13$ fm, the reaction plane resolution is not sufficiently reliable (see figure 4.11) to extract any value with respect to the reaction plane.

In addition to the small flow effect of pions due to the thermal motion, pions are subject to absorption and rescattering mainly through the delta resonance which has large mass. Thus they should show flow effects comparable to that of protons [Bas95, Li 94]. Since the observed $\langle p_x \rangle$ of pions is positive it indicates that the pions are preferentially emitted away from the target spectators.

This leads to the interpretation of an absorption of the pions in the target remnant, which appears as preferred emission toward the other side. If the apparent anti-flow is due to absorption, central collisions with little or no spectator matter should show no flow effect [Fil96]. For central events the pion flow signal is compatible with zero. The effect in semi-central collisions is weak but grows with the impact parameter nearly linearly. The in-plane average transverse momentum of pions confirms for sufficiently high impact parameters, i.e. $b > 5$ fm, the above described anti-flow. At AGS energies the anti-flow of positively charged pions was also observed in Au + Au collisions [Hil96, Kin97], although there the effect was small and lacking in statistics.

5.3 Dependence of $\langle p_x \rangle$ on Beam Energy

As mentioned above the transverse flow has been measured at different energies by a number of experiments. Together these measurements provide a systematic study of the beam energy dependence of the directed flow. The WA98 flow result for 158 AGeV Pb + Pb collisions at the CERN SPS from WA98 is compared to Au + Au collisions from Bevalac to AGS energies, i.e. from 100 AMeV to 10 AGeV. In figure 5.8 the data for a variety of experiments are presented along with theoretical predictions from a hydrodynamic model [Ris96]. The decrease of the flow signal observed for incident energies E_{in} greater than approximately 2 AGeV, is due to the fact that faster spectator matter is less easily deflected by the expanding participants. The data indicated with Ball are from the Plastic Ball experiment at the Bevalac [Dos87, Gus88]. The FOPI experiment is located at the SIS[2] accelerator [Her96, Rei98]. E802 and E877 are AGS experiments, the data points are from the references [Ahl98] and [Bar97b], respectively. While the NA49 data point is from reference [Woo98], the WA98 data point is from the present analysis.

The hydrodynamic calculations are meant as qualitative comparison only, since there are several uncertainties, which affect the quantitative evaluation within the hydrodynamic fluid model. Moreover the theoretical calculation involves the integration of $p_x(y)$ and dN/dy, which indeed gives different quantitative results. However, the systematic tendency turns out to be described rather well [Ris96]. The solid line represents predictions for an EOS including only hadronic matter, while the dashed line includes a first order phase transition to a QGP. The latter one shows a significant drop in the flow excitation function near 6 AGeV, which is explained by the reduced pressure, and therefore reduced expansion of a QGP and therefore a reduced deflection of the spectators, or directed flow [Ris95]. Since the absolute values of the theoretical predictions are uncertain the absolute position of this drop cannot be firmly predicted yet. Thus there is great interest in the measurement of the flow at several AGeV incident energy and the investigation

[2] Schwerionensynchrotron

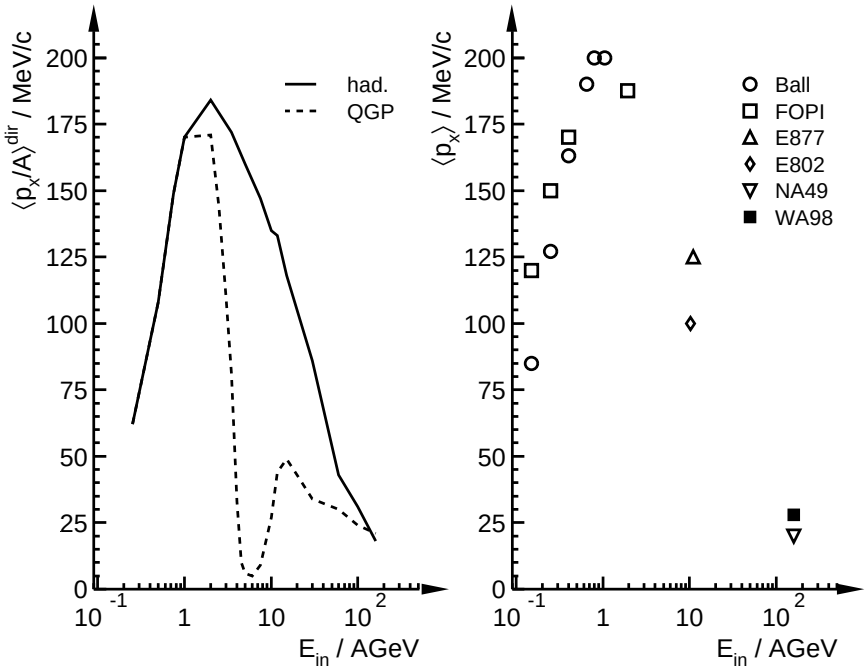

Figure 5.8: The transverse flow excitation function for symmetric heavy ion collisions. The curves (left panel) represent hydrodynamic calculations (see text). The data (right panel) are for Au + Au and Pb + Pb collisions. The references are given in the text.

of the E895 data at 2 – 8 AGeV is currently in progress [Liu98].

The WA98 data confirm rather well the decrease of the directed flow at high beam energies. The NA49 data point is slightly smaller than the WA98 point, but this could be explained by the fact that NA49 is not able to measure at target rapidity but closer to midrapidity, where the flow signal is smaller.

6. Azimuthal Correlation Analysis

In reference [Gut90] the flow effects were studied by means of Fourier expansion of the obtained azimuthal particle distributions. The Fourier expansion is defined in the following way:

$$\mathcal{O}(\phi) = \frac{x_0}{2\pi} + \frac{1}{\pi}\sum_{n=1}^{\infty}\left[x_n \cos(n\phi) + y_n \sin(n\phi)\right] \tag{6.1}$$

where $\mathcal{O}$ can be any observable as a function of the azimuthal angle ϕ, e.g. $dE_T(\phi)/d\phi$. The Fourier coefficients are denoted with x_n and y_n, respectively. Using the orthogonality of the Fourier series, these coefficients can be evaluated by:

$$\begin{aligned} x_n &= \int_0^{2\pi} \mathcal{O}(\phi)\cos(n\phi)\,d\phi = \sum_{i=1}^{N}\mathcal{O}_i\cos(n\phi_i) \\ y_n &= \int_0^{2\pi} \mathcal{O}(\phi)\sin(n\phi)\,d\phi = \sum_{i=1}^{N}\mathcal{O}_i\sin(n\phi_i) \end{aligned} \tag{6.2}$$

The sum runs over all particles N, and the azimuthal angle of the i-th particle is denoted with ϕ_i, which is measured with respect to the reaction plane angle Φ.

If the Fourier coefficients for the first harmonic (x_1, y_1) both are non-zero this is an indication of the presence of directed flow. The second harmonic would correspond to elliptic flow. The strength v_n of the flow effect of the n-th harmonic can be written as [Vol96]:

$$\begin{aligned} x_n &= v_n\cos(n\phi_n) \\ y_n &= v_n\sin(n\phi_n) \end{aligned} \tag{6.3}$$

where ϕ_n is the associated azimuthal angle. Thus one obtains:

$$v_n = \sqrt{x_n^2 + y_n^2} \tag{6.4}$$

This strength can be obtained from the measured Fourier coefficients v_n' by taking into account the finite reaction plane resolution analogous to the correction of the average transverse momentum (equation 5.2) as described in section 4.2.4:

$$v_n = v_n'/\sigma_{plane}(n) \tag{6.5}$$

Furthermore the transformation of the dipole moment for particles backward of midrapidity has, due to the anti-symmetry, to be applied as described in 5.1, thus $v_1 = -v_1'/\sigma_{plane}(n=1)$ is obtained.

In the following sections the rapidity, transverse momentum, and centrality dependence of the Fourier coefficients v_n for $n = 1, 2$ are studied for protons, deuterons, tritons, and positively charged pions measured with the Plastic Ball detector as well as for π^0 decay photons measured with the LEDA detector.

6.1 Dependence on Transverse Momentum

For all above mentioned particles the azimuthal particle distributions with respect to the reaction plane are calculated for several different transverse momenta.

Particles at Target Rapidity

Figure 6.1 shows the obtained $1/NdN/d\Delta\Phi$ distributions exemplary for protons and pions in five different

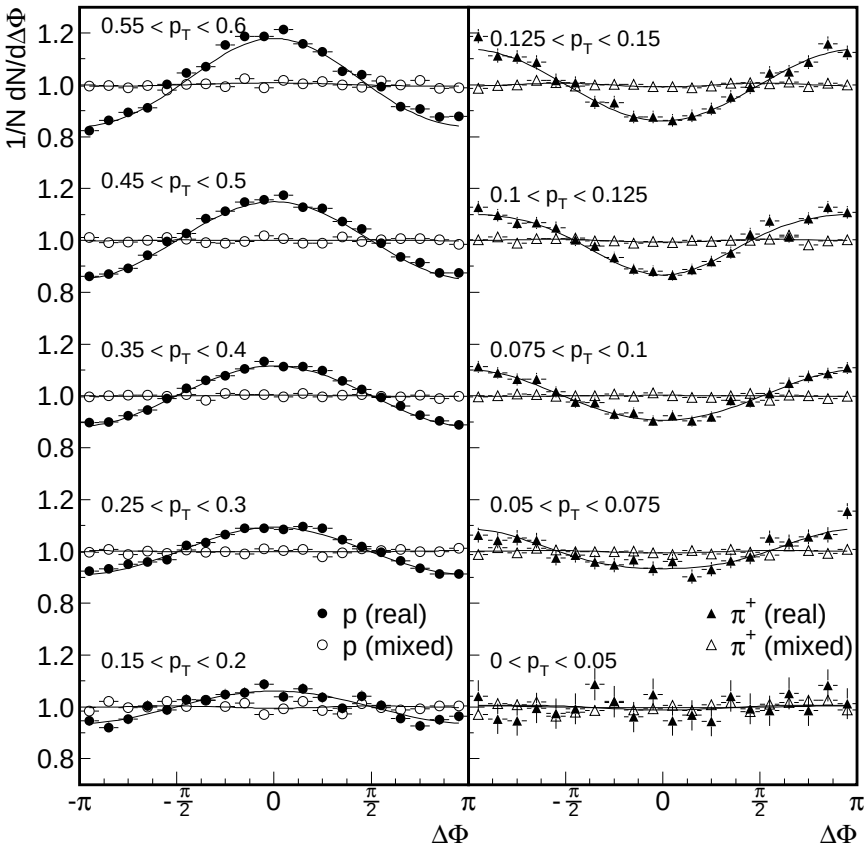

Figure 6.1: The azimuthal distributions of protons (left) at $20-40\,\%cs$ and pions (right) at $40-80\,\%cs$. The filled symbols are for real data, while the open symbols display the distributions of mixed events. The solid curves represent fits of equation 6.6 to the data. The rapidity range are $-0.4 < y < 0.1$ and $-0.6 < y < 0.0$ for protons and pions, respectively. The transverse momentum of the analyzed particles, given in GeV/c, is increasing from the bottom to the top.

p_T bins each. The angle $\Delta\Phi$ is the difference of the azimuthal angle of a particular measured particle and the reaction plane angle Φ.

Since in chapter 5 it was found that the flow effect of fragments is largest in the semi-central collisions, the proton distributions, presented in figure 6.1, are evaluated for the centrality $20-40\,\%cs$. The flow signal of pions however, was detected to be larger for more peripheral events, thus the $1/NdN/d\Delta\Phi$ distributions for pions are shown for the centrality $40-80\,\%cs$. All distributions are symmetric around zero and show

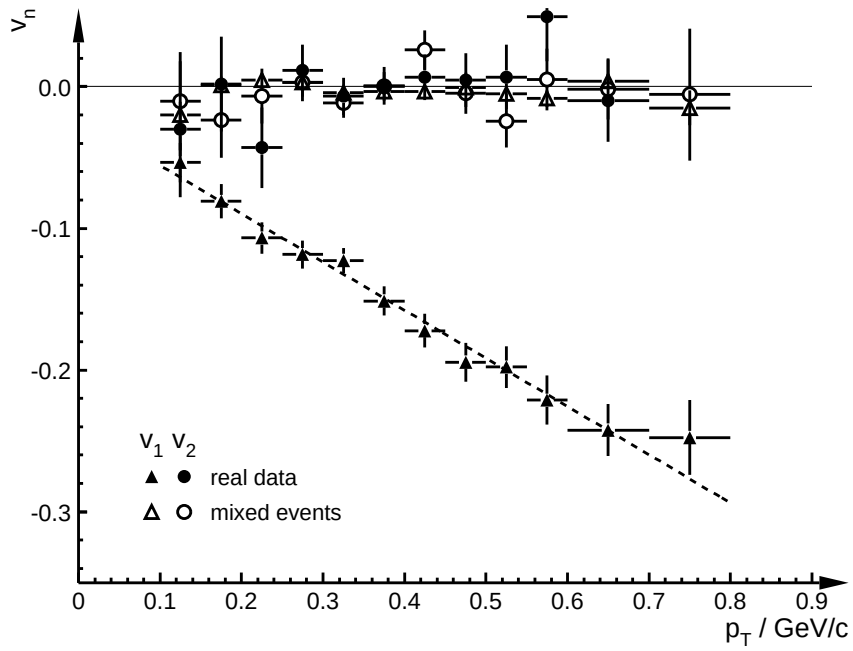

Figure 6.2: Transverse momentum dependence of the first (triangles) and second moment (circles), v_1 and v_2, of the proton azimuthal distributions. All particles are from the rapidity region $-0.4 < y < 0.1$ in the centrality bin $20-40\ \%cs$. The filled symbols represent real data and the open symbols mixed events. The dashed line indicates a linear fit to the v_1 values.

a strong correlation (protons) or anti-correlation (pions). Both types of correlations are of the same order of magnitude. The effect is increasing with the transverse momentum of the studied particles, i.e. from the bottom to the top in the figure 6.1. The distributions for mixed events do not give evidence for any correlation.

To extract the parameters of the correlation strength from these distributions a fit with the following function is applied:

$$\frac{1}{N}\frac{dN}{d\Delta\Phi} = 1 + 2v_1' \cos(\Delta\Phi) + 2v_2' \cos(2\Delta\Phi) \tag{6.6}$$

This provides the simultaneous determination of the strength of both, the dipole moment in terms of v_1' and the quadrupole moment v_2', though the quadrupole or second harmonic is not perceivable at this level. The dependence of the corrected values v_n for protons on the transverse momentum is presented in figure 6.2, where the same centrality and rapidity region is used as for figure 6.1. For the complete p_T range measured, the first harmonic v_1, or in other words the strength of the directed flow, turns out to be negative. This is in agreement with the result obtained from the average transverse momentum analysis, which in fact was integrating over the measured p_T. While the elliptic flow is within the error compatible with zero the directed flow reveals a linear dependence on the transverse momentum. The absolute flow signal increases with p_T and the slope can be parameterized by:

$$\frac{dv_1}{dp_T} = (-0.340 \pm 0.025)(\text{GeV}/c)^{-1}$$

This parameterization has been obtained from a straight line fit to the proton v_1 parameter as indicated by the dashed line in figure 6.2. This linear dependence can be understood if one assumes a thermal particle emission without radial expansion, which can be described by:

$$\frac{1}{p_T}\frac{d^3N}{dp_T dy d\phi} \propto Ee^{-E/T} \tag{6.7}$$

where E is the particle energy and T is the temperature. Assuming a velocity of β_x of the thermal source in x-direction, one has to take the Lorentz transformation into account and obtains for the Fourier coefficient [Bar97b]:

$$v_1 = \frac{I_1(\xi) - (\xi I_0(\xi) - I_1(\xi))T/E'}{I_0(\xi) - \xi I_1(\xi)T/E'} \tag{6.8}$$

where $\xi = p_T\beta_x\gamma_x/T$ with the commonly defined factor $\gamma_x = 1/\sqrt{1-\beta_x^2}$. $I_0(\xi)$ and $I_1(\xi)$ are the modified Bessel functions and E' is the particle energy evaluated in the system moving longitudinally together with the source. For $\beta_x \ll 1$, as expected for the transverse flow velocity, equation 6.8 can be approximated for $p_T < 1\,\mathrm{GeV}/c$ [Bra98]:

$$v_1 \approx \frac{I_1(\xi)}{I_0(\xi)} \approx \frac{p_T\beta_x}{2T} \tag{6.9}$$

In [Bar97b] actually deviations of the linearity have been observed for small values of p_T. The measured p_T region in this analysis however, confirms a linear behaviour of the transverse momentum dependence for the directed flow signal for protons rather well. In reference [App98] the dependence on p_T of the v_1 and v_2 parameter was studied closer to midrapidity. At the rapidity $4.0 < y < 5.0$ the component of the directed flow turned out to be rather small, $|v_1| < 0.1$, compared to the values obtained in this analysis. But this can be understood since the magnitude of the flow signal strongly depends on the rapidity, as it will be studied in section 6.2. Furthermore, in this reference a small but significant elliptic flow component was found near midrapidity, while at target rapidity it seems to vanish, or is at least not perceivable because of the dominating directed flow.

In figure 6.3 the dependence of the flow signal for the first harmonic on the transverse momentum is presented for positively charged pions. As expected the v_1 signal is positive and is increasing with p_T. The slope, determined by a linear fit, is larger than for protons:

$$\frac{dv_1}{dp_T} = (1.325 \pm 0.26)(\mathrm{GeV}/c)^{-1}$$

The distribution is fitted in the transverse momentum region $50\,\mathrm{MeV}/c < p_T < 180\,\mathrm{MeV}/c$ as indicated by the dashed line. The higher p_T bins are significantly lower than a linear increase would imply. It is expected that the flow of pions is due to rescattering and absorption mainly through the delta resonance. Due to the limited width of the delta resonance absorption of pions with higher p_T is suppressed compared to lower p_T pions. This might in part explain a flattening of the v_1 distribution for higher p_T. The $1/NdN/d\Delta\Phi$ distributions of pions for mixed events in figure 6.1 are flat for all p_T bins, thus the extracted v_1 signal is constantly zero (figure 6.3). Since the second harmonic does not show any significant deviations form

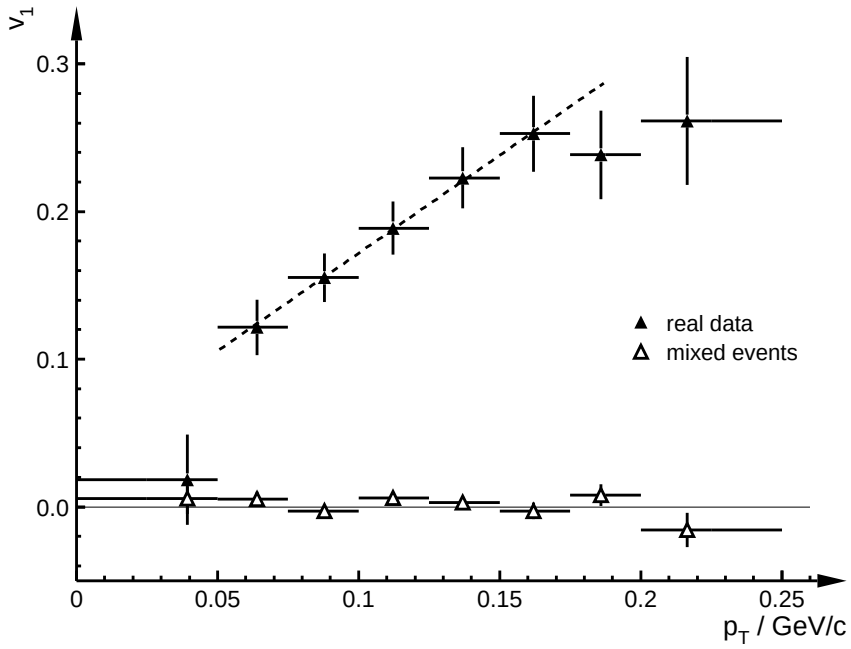

Figure 6.3: Transverse momentum dependence of the first harmonic for the π^+ azimuthal distributions. Pions from the rapidity region $-0.6 < y < 0.0$ in the centrality bin $40 - 80\,\%cs$ are shown. The filled symbols represent real data and the open symbols mixed events. The dashed line indicates a linear fit to the v_1 values.

zero it is for a better visibility not shown. Comparing this results with the flow signals measured near midrapidity reveals a very similar behaviour as for protons. The absolute magnitude of the directed flow is small ($|v_1| < 0.05$ [App98]) compared to the one obtained for the target rapidity region. And the absolute magnitude of the elliptic flow component is significantly different from zero. The reason again lies in the strong dependence of the flow effect on rapidity.

The same analysis was also performed for the heavier fragments. The $1/NdN/d\Delta\Phi$ distributions for deuterons and tritons are obtained for the p_T range $(0.17 - 1.08)\text{GeV}/c$ and $(0.22 - 1.26)\text{GeV}/c$, respectively. For semi-central collisions approximately a similar result was obtained as for protons. The directed flow parameter v_1 is presented in figure 6.4 for both, deuterons and tritons. Again the magnitude of the elliptic flow parameter was evaluated too, but it turned out to be compatible with zero and is therefore not shown in the figure. Since the v_1 of the fragments like the proton v_1 depends almost linearly on p_T the deuteron values are fitted with a straight line and the following slope has been obtained:

$$\frac{dv_1}{dp_T} = (-0.190 \pm 0.029)(\text{GeV}/c)^{-1}$$

This slope is slightly smaller than the one for protons. However, a direct comparison of the slope is not meaningful, since the fragments are measured at higher transverse momenta and in a smaller rapidity region. The astonishing fact about this result is that the absolute magnitude is about the same as for protons (figure 6.2), though measured in a different p_T region. From the average transverse momentum analysis in chapter

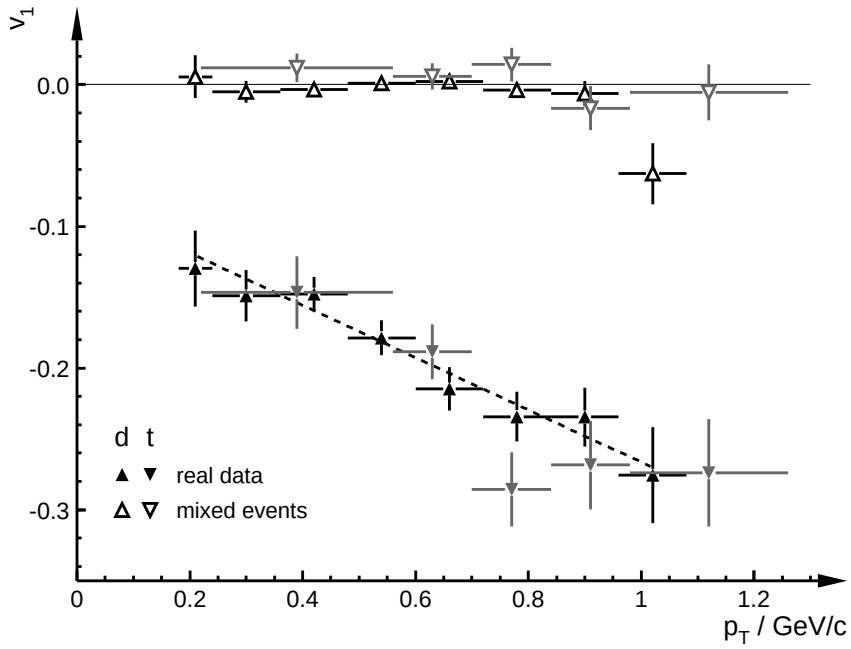

Figure 6.4: The transverse momentum dependence of the flow parameter v_1 for deuterons (triangle up) and tritons (triangle down) in the rapidity region $-0.3 < y < 0.1$. The filled symbols represent real data and the open symbols mixed events. The dashed line indicates a linear fit to the deuteron v_1 values. For a better visibility the triton data are plotted in grey.

5 as well as from results at lower energies a stronger dependence on the particle mass A was expected. In fact for 11 AGeV Au + Au collisions an increase of the flow effect from protons to deuterons was observed, while there is rather no increase from deuterons to tritons [Bar98b]. The latter fact is also confirmed in figure 6.4 showing that the tritons are very similar to the deuterons. The significant difference between protons and deuterons however, is not observed in the analysis of 158 AGeV Pb + Pb collisions. In part this can be explained by the smaller rapidity range in which the heavier fragments are detected, as described further on in section 6.2.

Particles Near Midrapidity

The LEDA detector measures decay photons mainly of the neutral pions directly below midrapidity. Since it does not, contrary to the Plastic Ball, provide full azimuthal coverage, this affects the azimuthal particle distributions measured in the lead glass detector. To take this detector effect into account, the real data distributions are normalized by the ones obtained for mixed events. The resulting azimuthal distributions of the photons are analyzed by fitting with the above described Fourier expansion, i.e. equation 6.6. For γ's qualitatively different distributions, compared to particles at target rapidity, are obtained as presented in figure 6.5.

First of all the photons show a much weaker flow effect than the particles measured at target rapidity.

This is not surprising considering on the one hand the rapidity dependence of the magnitude of the flow effect, this will be studied in section 6.2. And on the other hand it certainly plays a role that the photons are decay products and therefore the only reason exhibiting any flow, as they obviously do in figure 6.5, is that they still carry a part of the original pion flow velocity. The second important change from target to midrapidity is that the component of directed flow seems to vanish, while an elliptic flow component, not visible at target rapidity, can be observed. This can be extracted from figure 6.5 which clearly reveals the existence of the the second harmonic in the distributions. The surprising result is, that the elliptic flow turns out to be negative, i.e. it exhibits an out-of-plane flow. This is in contrast to the positively charged pions

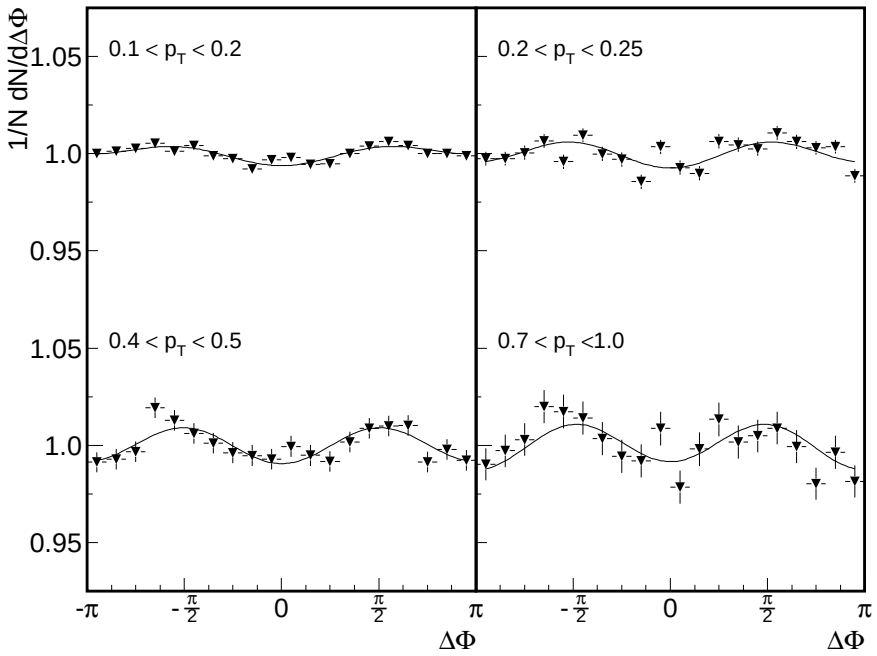

Figure 6.5: The azimuthal distributions for π^0 decay photons detected with LEDA for different transverse momenta in GeV/c. The solid curves represent a fit of equation 6.6 to the data, which have been corrected by mixed events. Shown are semi-central events.

[App98] and since neutral pions are expected to behave like the charged pions, the remaining photon signal is not yet understood (see appendix F). In agreement with the fragments and the positively charged pions however, is the fact that the absolute magnitude depends on the photon transverse momenta as displayed in figure 6.6.

A closer look at the lower p_T range reveals a very weak but significant positive v_1 signal for photons. This effect however, is only observable for photons below $400\,\mathrm{MeV}/c$ and is of the order of $0.5\,\% - 1\,\%$. Thus, this effect at the percentage level is a factor of approximately 15 - 25 smaller than obtained for target rapidity particles. The elliptic component v_2 however, is rather pronounced and its absolute magnitude increases for $p_T < 500\,\mathrm{MeV}/c$ almost linearly. For larger transverse momenta the effect tends to saturate and does not exceed values of $|v_2| \approx 0.1$.

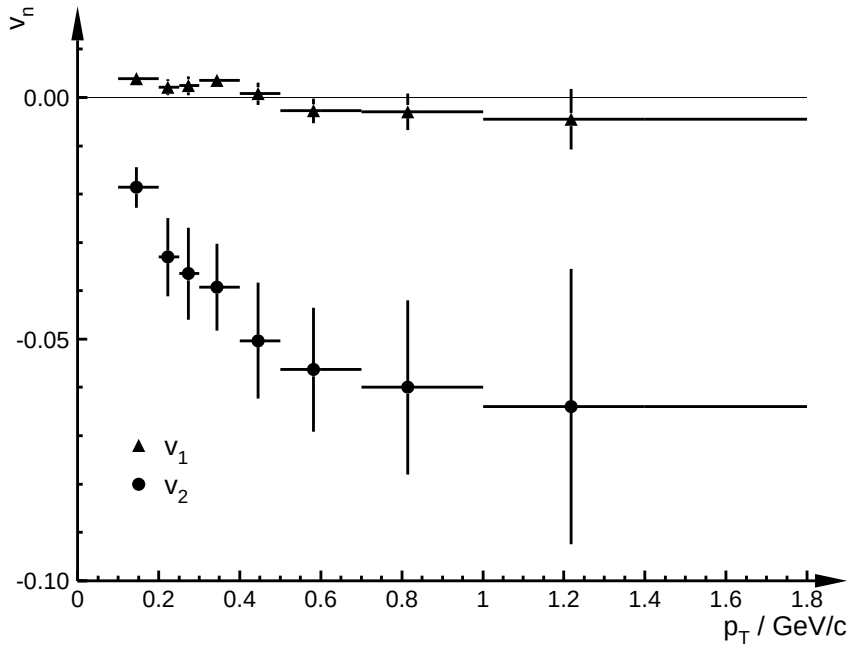

Figure 6.6: Transverse momentum dependence of the first (triangle) and second (circles) harmonic for the π^0 decay photons. Displayed are semi-central events for γ's at $2.3 < y < 2.9$.

6.2 Dependence on Rapidity

It has become evident, so far, that there are differences in the magnitude of the flow signal for particles at target and near midrapidity observable. In this section the systematic dependence of the flow parameters, in terms of the Fourier coefficients up to the second order, on rapidity is studied. Protons show a very weak elliptic flow component at target rapidity. Going to midrapidity ($y = 2.9$) this harmonic increases to the level of $\approx 10\,\%$, as displayed in figure 6.7. The figure shows data from this analysis and from [App98]. The elliptic flow is symmetric around midrapidity and has been reflected to the respective side. The WA98 proton data for semi-central events are measured in the backward and reflected to the forward hemisphere, and vice versa for the NA49 data. The fact that the elliptic flow turns out to be positive means it is aligned with the reaction plane. Thus it is in-plane flow and not out-of-plane flow as it was observed at lower energies, see e.g. [Gut90].

The directed flow is anti-symmetric around midrapidity and peaks typically at target and projectile rapidity. The shape of the distribution however, looks different to that observed in Au + Au collisions at $200\,A$MeV [Dos87] and $11\,A$GeV [Bar97a]. At lower beam energies the increase of the flow strength from zero at midrapidity is rather linear to the peaks at target and projectile rapidity. This is displayed in figure 6.8, where the strength of the directed flow is given in terms of $\langle p_x/p_T \rangle$, which can approximately be equated with v_1. Further away from this peak it falls off weakly, this rapidity dependence is often referred to as S-shape curve. In the studied $158\,A$GeV Pb + Pb collisions however, the peaks look more Gaussian

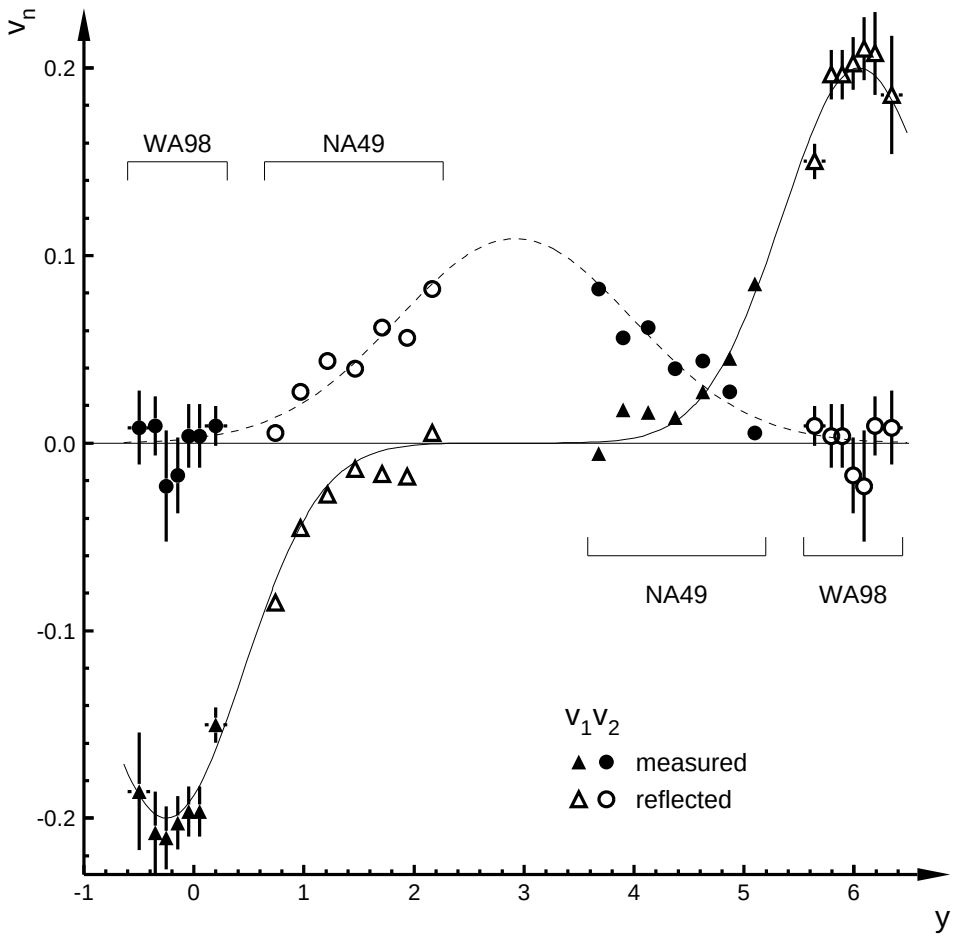

Figure 6.7: The Fourier coefficients v_1 (triangles) and v_2 (circles) for protons as a function of rapidity. The solid symbols represent the actually measured data points and the open symbols correspond to the same values reflected around midrapidity $y = 2.9$. The data from the NA49 experiment are from reference [App98] without error bars. The curves are to guide the eye.

and only the tails reach up to midrapidity, where the flow signal is small. Thus it is conceivable that the S-shape curve obtained at lower beam energies is also a combination of two Gaussian distributions. These distributions would have on the same normalized rapidity scale larger widths and the mean positions at target and projectile rapidity. This could actually be confirmed for the proton data from 200 AMeV Au + Au collisions provided by [Dos87, Kam86]. In figure 6.8 the superposition of two anti-symmetric Gaussian distributions is displayed. The dashed curve is provided by a fit to the data. The dotted curve is obtained by reflection around midrapidity and the solid curve is the superposition. The rapidity dependence and in particular the slope at midrapidity is rather well described, the forward-backward asymmetry of the data is an artifact of experimental biases [Dos87]. Both Gaussians are not separated and have a large overlap region.

Hence the peak position in figure 6.7 was also obtained by fitting the Plastic Ball v_1 data with a Gaussian

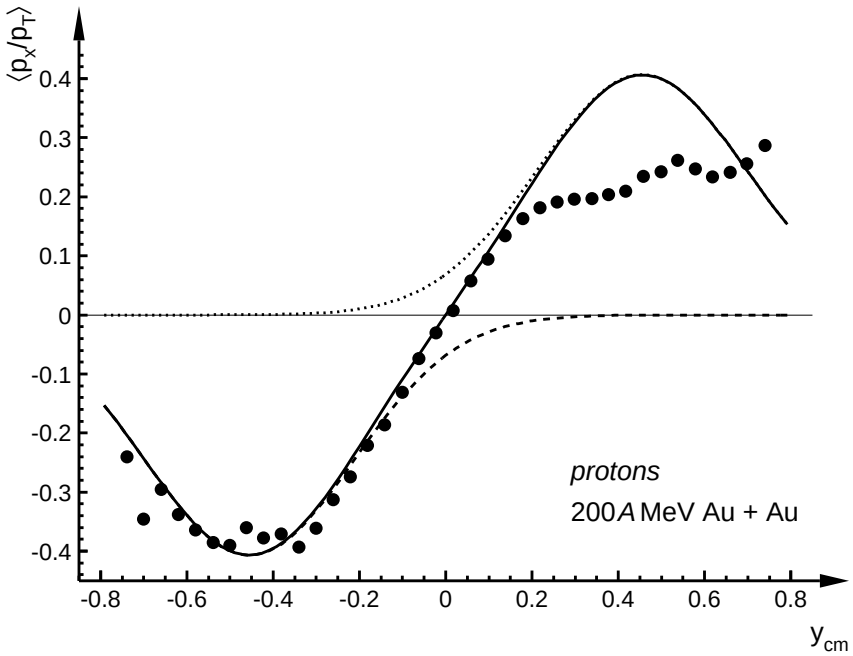

Figure 6.8: The strength of the directed flow of protons in $200\,A$MeV Au + Au collisions in dependence of centre-of-mass rapidity. The data backward of midrapidity is fitted by a Gaussian distribution (dashed curve). The fit result is reflected around $y_{cm} = 0$ (dotted curve) and both distributions are superimposed (solid curve). The data are from reference [Dos87].

distribution. This provides the value of the maximum directed flow $v_{1,max} \approx -0.2$ at $y \approx -0.25$. And in fact the solid line in figure 6.7 is a composition of two anti-symmetric Gaussian distributions with the above mentioned maximum and mean value. Therefore the WA98 Plastic Ball data permit the determination of the Gaussian shape and the NA49 data confirm the flattening near midrapidity. This shape implies that the slope near midrapidity, which is often referred to as flow value $F = dv_1/dy$, does not provide a reasonable description of the collective momentum transfer at high beam energies. To study the systematics of directed flow it is rather necessary to analyze the three parameters of the Gaussian-shaped rapidity distribution.

In the same manner the π^+ flow dependence on rapidity is presented in figure 6.9. The NA49 data values are again from reference [App98] for semi-central events, the midrapidity data points are provided by the second tracking arm spectrometer in the WA98 experiment [Eno98]. The data measured at target rapidity are the Plastic Ball result of this analysis in the centrality bin $40 - 80\,\%cs$, where the pion flow effect is largest. The first harmonic is positive at target rapidity, i.e. opposite to the fragment flow direction. It peaks at $y \approx -0.55$ with a maximum value of $v_1 \approx 0.24$. Closer to $y = 2.9$ it rapidly decreases and completely vanishes at midrapidity, to which it is defined to be anti-symmetric. The NA49 data confirm the weakness of the directed flow near midrapidity, though it shows some structure which is not reproduced by the smooth curve shown. This curve represents again a composition of two Gaussian distributions, with the above given maximum and mean value.

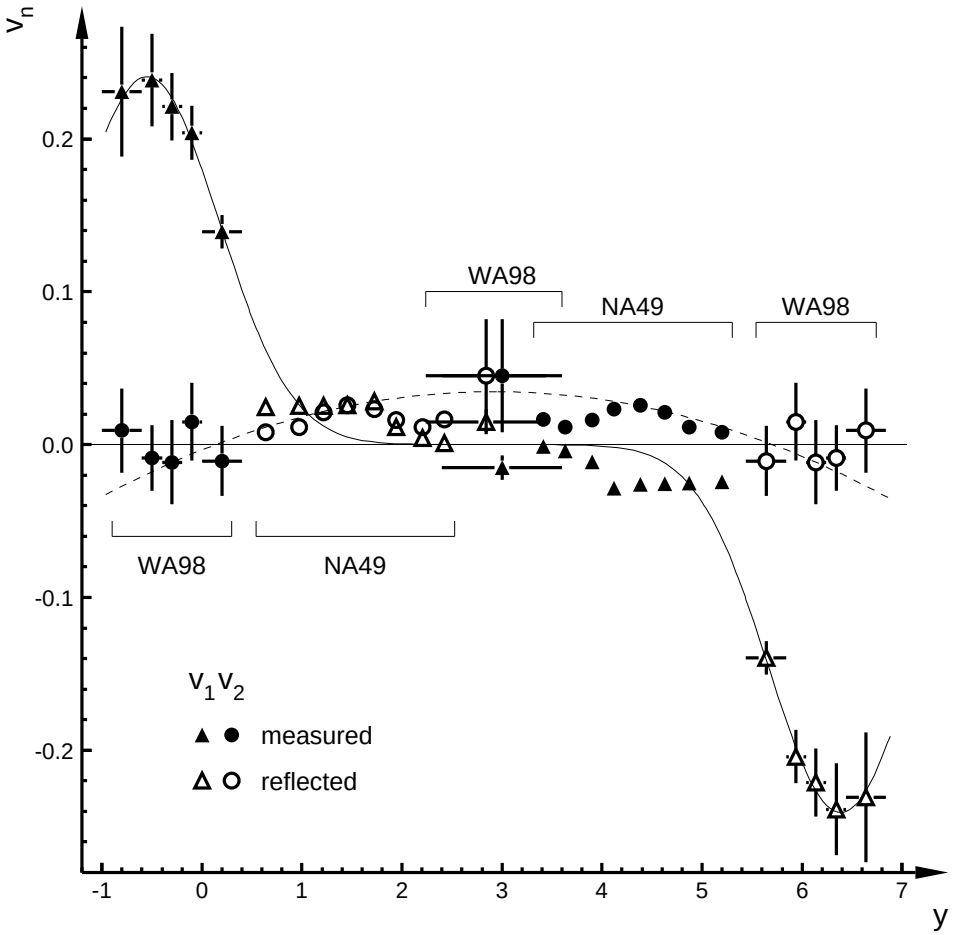

Figure 6.9: The strength of the directed (triangles) and elliptic (circles) flow effect of positively charged pions as function of rapidity. Solid symbols are measured data, while open symbols represent the data reflected around midrapidity. The NA49 data were obtained from [App98] and are given without errors. The WA98 data points at midrapidity are preliminary data from the tracking arm spectrometer ARM2 from [Eno98]. The curves are to guide the eye.

The strength of the elliptic flow at target rapidity is within the errors consistent with zero. It increases slightly to midrapidity, but does not exceed the $5\,\%$ level. This is contrary to the elliptic flow component v_2 of the protons, which reaches values of $v_2 \approx 0.1$ or $10\,\%$. Again the data from the NA49 experiment reveal some structure for the near midrapidity bins, which is below the $1\,\%$ level and considering the data point from ARM2 it is not reproduced by the smooth curve given as dashed line. The important point however, is the fact that v_2 for pions, like the proton result, is positive. This means the main axis of the flow ellipsoid is aligned with the reaction plane. In other words the pions show at midrapidity elliptic in-plane flow.

The heavier fragments exhibit a stronger directed flow effect than the protons, but in the same direction. The elliptic flow is consistent with zero, as can be seen in figure 6.10. So far the measurement of these Fourier coefficients for deuterons and tritons at SPS energies is limited to the backward rapidity region

covered by the Plastic Ball. Thus this result is not compared to the near midrapidity region. The fragments

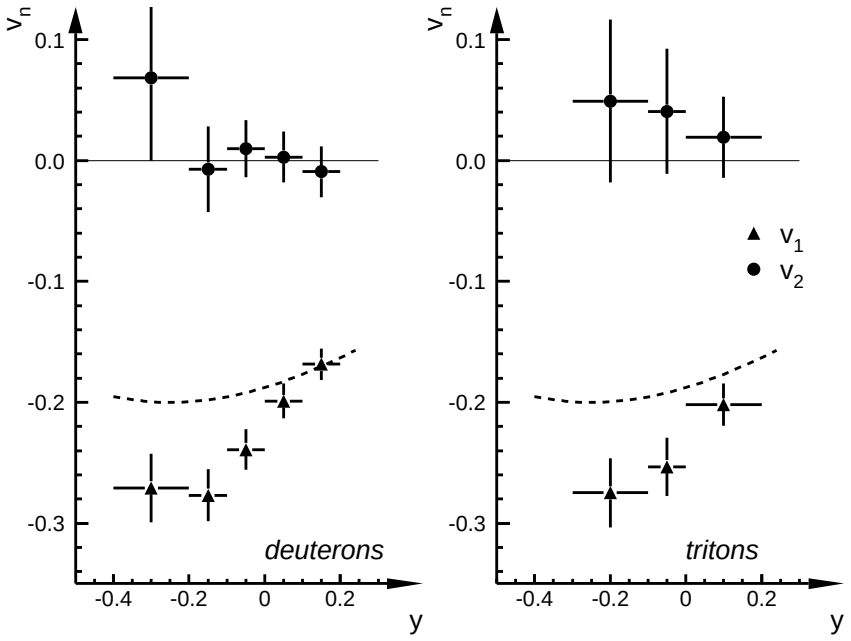

Figure 6.10: The strength of the directed (triangles) and elliptic (circles) flow effect of deuterons (left) and tritons (right). The dashed line indicates the strength of the proton directed flow according to figure 6.7.

show a stronger dependence on rapidity than the protons which are indicated by the dashed lines. The covered rapidity region does not allow to fix the peak position, the strong rise rather indicates that the peak is not yet reached. Nevertheless one can determine the maximum measured flow strength with $v_{1,max} \approx 0.28$ for both, deuterons and tritons.

The transverse flow of the measured photons is displayed in figure 6.11 as function of the rapidity. For photons with a transverse momentum $p_T > 400\,\mathrm{MeV}/c$ (left panel) the first harmonic is even consistent with zero. For low p_T photons (right panel) however, the directed flow turns out to be weak but significantly positive, i.e. opposite to the fragment flow. This is in good agreement with figure 6.9 and would at first sight indicate a simple relation between the flow of pions and their decay products. This might be true for the directed component, however, the elliptic component does behave contrary. Figure 6.11 illustrates the nearly linear dependence on rapidity of the elliptic flow component, which is negative for the whole rapidity region covered by the LEDA detector. In other words the photons exhibit elliptic out-of-plane flow, but the positively charged pions are observed to flow in-plane.

6.3 Dependence on Centrality

Exemplary for all fragments figure 6.12 reflects the strength of the flow effects as function of the number of participants W_N for protons. In addition the results obtained for mixed events (open symbols) are pre-

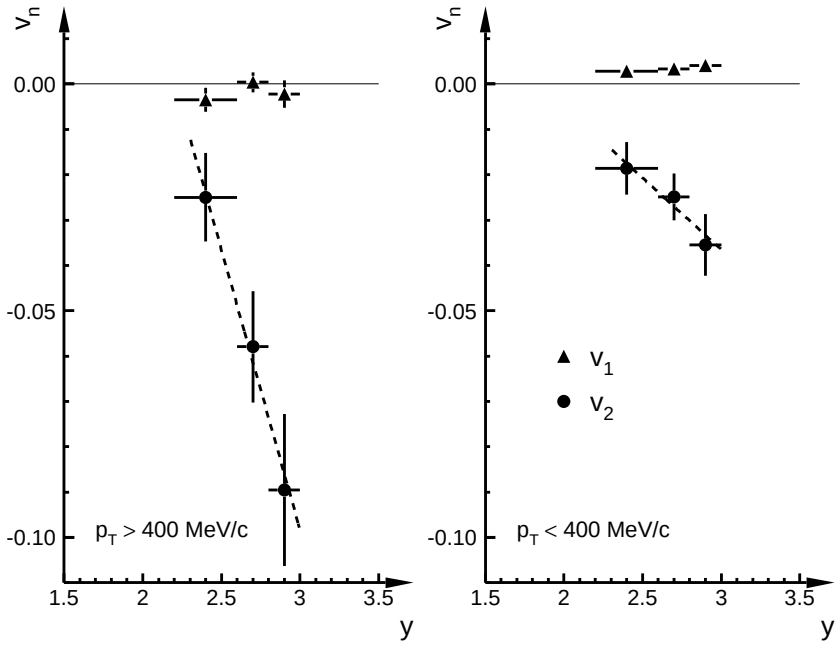

Figure 6.11: The Fourier coefficients v_1 (triangles) and v_2 (circles) obtained for π^0 decay photons near midrapidity. The left side represents the high p_T range, the right one the range $p_T < 400\,\mathrm{MeV}/c$. The dashed lines are to guide the eye.

sented to proof again the negligible detector effects. The shown data are integrated over the whole proton acceptance range of the Plastic Ball detector. The centrality dependence of the directed flow looks already familiar since it was analyzed with the transverse momentum method in terms of $\langle p_x \rangle$ (see figure 5.7a). The largest directed flow occurs in semi-central collisions with an impact parameter of $b \approx 8$ fm. The effect is of the order of $15\,\%$, which is the same number provided by the correlation of subevents for this centrality bin (see section 4.2.2).

With the Fourier expansion of the azimuthal particle distributions the elliptic flow is evaluated. For peripheral events there is a non-zero negative, or out-of-plane, elliptic flow of the order of $v_2 \approx -0.05$. For semi-central collisions this effect vanishes and for central collisions a weak positive, or in-plane, elliptic flow is observed. In other words in very peripheral events a weak out-of-plane flow, also referred to as squeeze-out [Gut89a], is observable for protons at target rapidity. For the heavier fragments the above described phenomena are as expected even more pronounced. The directed flow in semi-central events turns out to be an effect of $19\,\%$ and $23\,\%$ for deuterons and tritons, respectively. In peripheral events a squeeze-out effect of $v_2 = -0.07 \pm 0.04$ for deuterons and $v_2 = -0.12 \pm 0.10$ for tritons is obtained.

Not only the magnitude of the proton v_1, but also its peak position in rapidity is observed to vary with centrality. Therefore the peak position $y(v_{1,max})$ is determined by fitting the v_1 rapidity distribution by a Gaussian as described in section 6.2. The evolution of the peak position as a function of centrality is displayed in figure 6.13. It decreases with the number of participants W_N. This means $y(v_{1,max})$ is closer

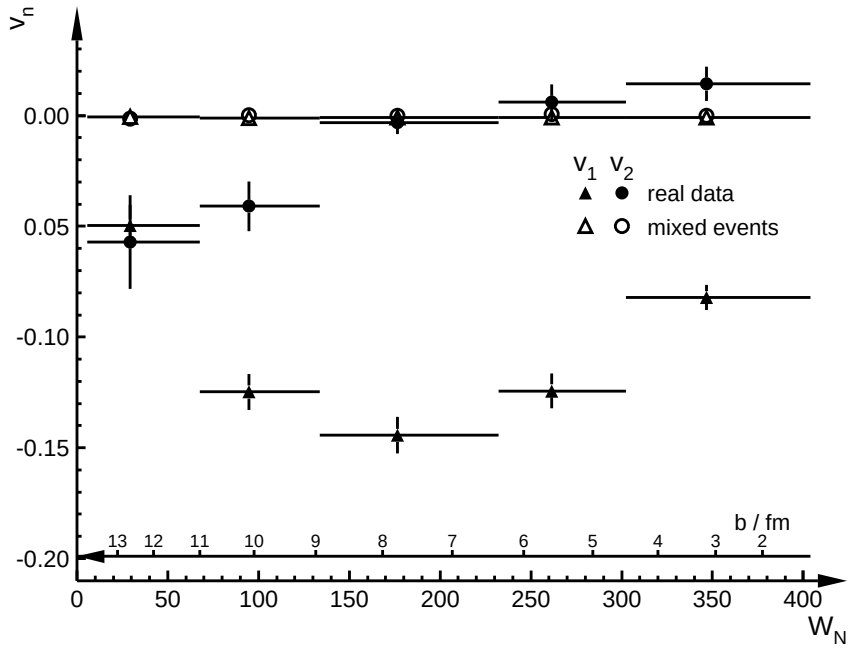

Figure 6.12: The centrality dependence of the strength of the directed (triangles) and the elliptic (circles) flow effect of protons. The solid symbols are for real data, while the open symbols are obtained from mixed events. Additionally the impact parameter axis is given.

to midrapidity in peripheral than in more central collisions. Though in very central collisions the directed flow effect vanishes due to the symmetry and thus for the bin of the most central collisions the evaluation of the peak position is rather difficult. This is reflected by the large fit error given in the figure. Also at lower beam momenta a variation with centrality of the peak position in the v_1 rapidity distribution has been observed [Bar97a]. Since the mean of the proton rapidity distribution does not change with the centrality the observed evolution of $y(v_{1,max})$ with centrality is apparently a property of the event asymmetry. However, the possible background of the identified protons depends also on centrality. For higher centrality, i.e. higher hit multiplicity, the number of double hits is larger and the particle identification is more difficult. This might influence the peak position in rapidity (see appendix E).

As for the protons the dependence of the directed flow strength of π^+ on the centrality is already provided in the subevent and the transverse momentum analysis. Figure 6.14 presents the directed and the elliptic flow in terms of v_1 and v_2 respectively, integrated over the whole Plastic Ball acceptance. The value of v_1 decreases with the number of participants. The largest effect is observed in more peripheral collisions ($\approx 17\,\%$). The elliptic flow component is weak or even consistent with zero for all collisions with $b > 6.5\,\mathrm{fm}$. For smaller impact parameters it exhibits a positive, i.e. in-plane, signal. The apparently large effect observed for central collisions is not yet understood and needs further studying.

As depicted in figure 6.6 the photon v_2 increases in magnitude for increasing p_T, v_1 though, exhibits

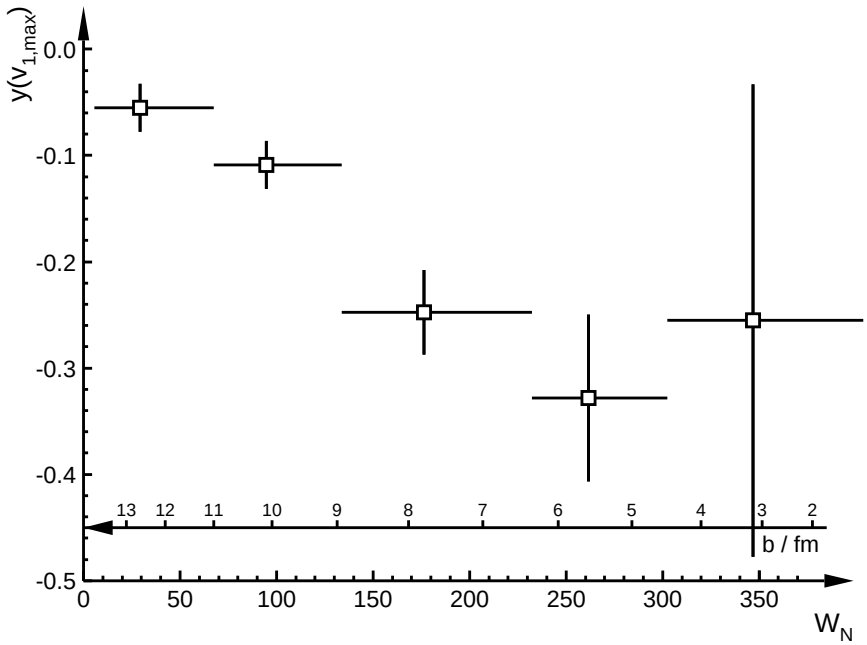

Figure 6.13: The centrality dependence of the peak position of the v_1 rapidity distributions for protons. The given errors are the errors of the Gaussian fit.

a qualitative change from anti-flow at low p_T to weak flow at higher p_T. Considering this p_T dependence of the flow effect for photons in the LEDA detector, two transverse momentum bins are chosen to present the flow strength as a function of centrality in figure 6.15. For both $p_T > 400\,\mathrm{MeV}/c$ (left panel) and $p_T < 400\,\mathrm{MeV}/c$ (right panel) the elliptic flow decreases with the number of participants. In peripheral collisions for lower p_T the strength of the elliptic flow is in maximum $v_2 \approx 0.03$, where for higher p_T it exceeds $v_2 \approx 0.08$. For the low transverse momentum region the photons in LEDA exhibit the same centrality dependence of v_1 as the π^+, though the absolute magnitude is smaller by a factor of approximately 20. In collisions with $b < 9\,\mathrm{fm}$ the photons with $p_T > 400\,\mathrm{MeV}/c$ show a very weak directed flow effect, for larger impact parameters v_1 is consistent with zero. Apparently the directed flow is carried by γ's with small transverse momentum, while the elliptic flow is dominant for the high p_T γ's.

6.4 Comparison with the $\langle p_x \rangle$ Method

The results obtained within the azimuthal correlation method confirm rather well the flow effects observed by the transverse momentum analysis. The Fourier expansion, though, provides even more information. In particular it allows the systematic analysis of the elliptic event shape deformation. Furthermore one can also evaluate the transverse momentum transfer in the reaction plane $\langle p_x \rangle$ by integrating the $v_1(p_T)$ distribution

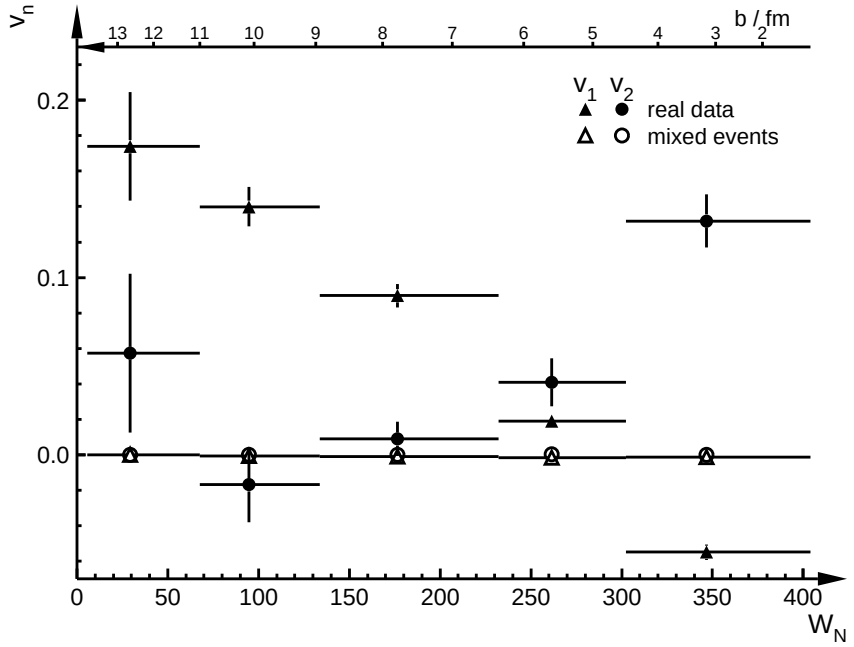

Figure 6.14: The centrality dependence of the strength of the directed (triangles) and the elliptic (circles) π^+ flow. The solid symbols are for real data, while the open symbols are obtained from mixed events. Additionally the impact parameter axis is given.

[Bra98]:

$$\langle p_x \rangle = \frac{1}{N} \int_0^\infty v_1(p_T)\, p_T\, \frac{dN}{dp_T}\, dp_T \tag{6.10}$$

where N is the number of observed particles and the $v_1(p_T)$ distributions are given for the different particle species in section 6.1. The respective proton distribution e.g. was presented in figure 6.2. The integration of equation 6.10 was applied to all obtained $v_1(p_T)$ distributions. The result is summarized in table 6.1.

particle	y	p_T/MeV/c	$\langle p_x \rangle$/MeV/c
p	-0.4 – 0.1	100 - 800	-64.0 ± 8.9
d	-0.3 – 0.1	180 - 1080	-114.5 ± 20.1
t	-0.3 – 0.1	220 - 1260	-167.5 ± 37.3
π^+	-0.6 – 0.0	50 - 250	22.9 ± 4.9

Table 6.1: The average transverse momentum $\langle p_x \rangle$ determined with the Fourier expansion method.

The quantitative result is apparently different from the one provided by the transverse momentum method presented in chapter 5. This discrepancy however, can be explained by the different p_T regions covered. Evaluating the integral according to equation 6.10 requires a complete measurement down to $p_T = 0$. This is important since the p_T particle spectra are approximately exponential. Thus the number of low p_T particles is much larger than the higher p_T particles and the latter ones contribute less to the transverse momentum transfer. But the transverse momentum can, as stated in table 6.1, not be measured down to zero. This acceptance hole, as it is visible in the $d^2N/dp_{x'}dp_{y'}$ distributions in figures 5.1 – 5.3,

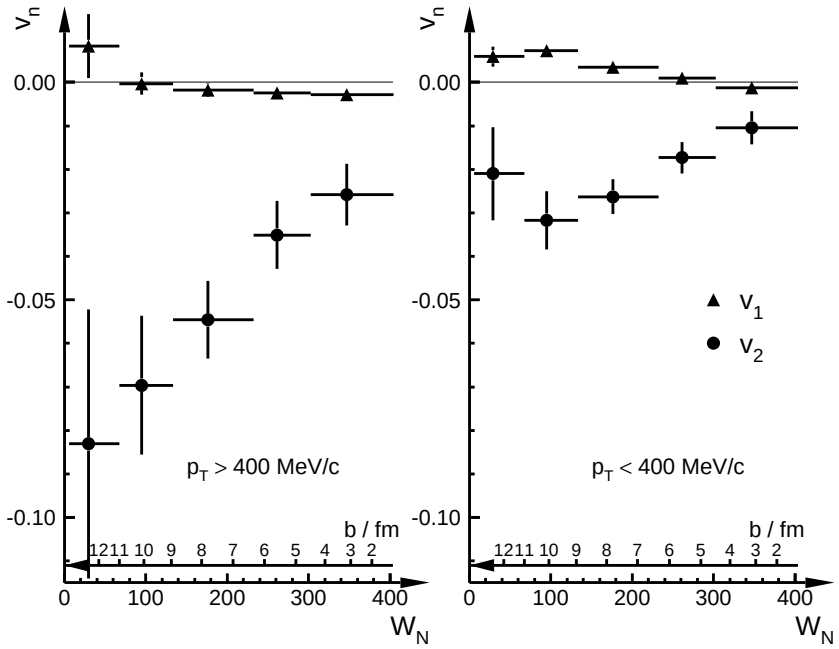

Figure 6.15: The centrality dependence of the strength of the directed (triangles) and the elliptic (circles) photon flow. Two different transverse momentum bins are presented, $p_T > 400\,\mathrm{MeV}/c$ on the left and $p_T < 400\,\mathrm{MeV}/c$ on the right.

could be evaded in the transverse momentum method by fitting a two dimensional Gaussian to the particle distribution, which extrapolates the transverse momenta down to zero. An extrapolation of the $v_1(p_T)$ distributions to $p_T = 0$ is conceivable, too. In reference [Bar97b] however, it was observed that especially in the low p_T region the data deviates from the linear behaviour. And since a parameterization for this region is in our case not known, it is not meaningful to evaluate the quantitative values with this method.

Nevertheless is the qualitative result in rather good agreement with the transverse momentum method. Again negative values are obtained for the average transverse momenta of fragments. The directed flow strength is a function of the fragment mass, i.e. the deuteron $\langle p_x \rangle$ is about twice and the triton $\langle p_x \rangle$ is approximately three times as large as the proton $\langle p_x \rangle$. The positively charged pions exhibit an positive transverse momentum transfer, which confirms again the anti-flow behaviour of the produced mesons.

It is conceivable that an elliptic event shape will also be observable with the average transverse momentum method. If particles are emitted in a preferred direction this could affect the width of the $d^2N/dp_x dp_y$ distribution. Elliptic in-plane flow would increase the width of the Gaussian distribution in x-direction, in y-direction the distribution would be smaller. This effect is studied for protons and pions by means of the ratio $\varepsilon \equiv \sigma_x/\sigma_y$, where σ_x and σ_y are the widths of the two dimensional Gaussian fit to the $d^2N/dp_x dp_y$ distribution. For symmetric distributions $\varepsilon = 1$ is expected. The dimensionless parameter ε is evaluated for all rapidity bins for protons and pions and turned in out to be consistent with 1 within the errors. The effect has a magnitude of $0.2\,\%$ ($0.3\,\%$) for protons (pions). Thus the transverse momentum distributions do not

exhibit an elliptic deformation. This is in good agreement with the azimuthal correlation method, where the elliptic flow in the target rapidity region was found to be consistent with zero for protons and pions.

7. Summary and Conclusions

In this thesis high energy heavy ion collisions are studied with attention to collective flow phenomena. The analyzed data are from Pb + Pb collisions at $33\,\mathrm{TeV}$, i.e. $158\,\mathrm{GeV}$ per nucleon, measured in the WA98 experiment at the CERN SPS accelerator.

The Plastic Ball spectrometer is successfully utilized to determine the reaction plane on an event-by-event basis. Different methods to evaluate the reaction plane from the measured data are described. In the present analysis the Fourier method is applied to extract the reaction plane. Based on the azimuthal distribution of the transverse energy E_T of protons and light target fragments the orientation of the reaction plane is determined. The resolution is obtained from the correlation strength of randomly arranged subevents. The correlation strength of fragments shows a strong dependence on centrality. It is largest for an impact parameter of $b \approx 8\,\mathrm{fm}$, i.e. for semi-central collisions and decreases for larger impact parameters and vanishes for central collisions. Pions turn out to be anti-correlated to the fragments and the anti-correlation increases with the impact parameter.

The average transverse momentum $\langle p_x \rangle$ in the reaction plane is a measure of the directed flow. $\langle p_x \rangle$ is evaluated as function of centrality and rapidity. Significant directed flow (anti-flow) is measured for fragments (pions) in the target rapidity region. Model calculations overestimate the measured transverse momentum transfer by a factor of 2 – 3. The centrality dependence reveals, as in the subevent analysis, for fragments the largest effect in semi-central collisions. The directed pion anti-flow tends to increase with increasing impact parameter. The analysis of the rapidity dependence allows to fix the peak position at $y \approx -0.2$ for protons. The average transverse momentum of deuterons and tritons apparently rises to smaller rapidities and the peak position cannot be fixed in the covered rapidity region. Pions, however, exhibit a clear peak at $y \approx -0.4$. In the same rapidity range the deuterons have approximately an average transverse momentum twice as large as the one of protons. The $\langle p_x \rangle$ of tritons is three times larger than the one of protons. This fact indicates that the fragments are emitted by a source of common collective motion.

The strength of the directed flow reveals a strong dependence on the beam energy. In a simple geometrical model this can be explained by the fact that at low incident energies the directed flow is mainly caused by the deflection of spectator matter by the expanding participants (bounce-off). This effect is suppressed at higher energies since faster spectator matter is expected to be less easily deflected and the directed flow is then mainly driven by the pressure gradient of the reaction zone. The flow excitation function increases with the incident energy up to $\approx 1A$GeV, for larger energies a decrease is observed. Hydrodynamic calculations qualitatively reproduce this behaviour and predict a significant difference between pure hadronic matter and a possible QGP. Therefore the analysis of the flow excitation function

provides information about a possible phase transition. In order to obtain a clear picture of the collision dynamics the flow excitation function has to be known as complete as possible for a large energy region. The present analysis shows that the WA98 experiment is able to cover the high energy part.

The event shape was also studied by a Fourier analysis of azimuthal particle correlations. This has the advantage that also higher moments can be analyzed. The strength of the flow effect is measured in terms of coefficient v_n for the n-th harmonic. The particles detected in the target rapidity region exhibit a significant directed flow effect, while the elliptic flow component is consistent with zero. However, photons from the π^0 decay measured near midrapidity show only weak directed, but significant elliptic flow.

The parameter v_1, i.e. the strength of the directed flow, depends nearly linearly on the transverse momentum in the p_T region covered. The centrality dependence of v_1 confirms rather well the result obtained with the transverse momentum method. The largest effect of $15\,\%$ is observed in semi-central collisions, i.e. for an impact parameter of $b \approx 8$ fm. This is the case for all target fragments p, d, and t. Positively charged pions, however, show an increase of v_1 with the impact parameter. In semi-central events a $10\,\%$ effect is observed, while in more peripheral events the directed flow effect is approximately $17\,\%$. The π^0 decay photons of small transverse momentum p_T exhibit a weak directed flow with the same dependence on centrality as the π^+. This indicates that the photons still carry a part of the original π^0 flow velocity. The absolute magnitude is smaller by a factor of approximately 20 which can be explained by the strong dependence on rapidity, since the photons are measured near midrapidity, while the π^+ are detected in the target fragmentation region.

The elliptic flow component also reveals a dependence on centrality. In semi-central events it is consistent with zero. However, for large impact parameters the protons at target rapidity have a negative v_2. In other words, in peripheral collisions with a large number of spectators (> 300) an out-of-plane elliptic flow, or squeeze-out, is observed. This effect is of the order of 6% and can be explained by the shadowing of protons by the spectator matter. In central collisions the v_2 parameter is positive, i.e. a $\approx 1.5\,\%$ elliptic in-plane flow effect of protons is observed. Here, the number of spectators is small and shadowing effects apparently vanish. Hence the elliptic flow can develop along the lines of the highest pressure gradient, i.e. in-plane. Positively charged pions also exhibit a significant elliptic in-plane flow in central collisions. The π^0 decay photons near midrapidity show negative v_2 for all centralities. The strength of the elliptic flow increases with the impact parameter. Neutral and charged pions are expected to exhibit the same flow phenomena. And the directed flow of the π^0 decay photons near midrapidity indicates the same flow as observed for charged pions near midrapidity in the NA49 experiment. However, the elliptic flow effect is found with different sign for photons and charged pions.

The study of the rapidity dependence of the flow strength v_n reveals some important features. The directed flow is large at target and projectile rapidity and vanishes at midrapidity. Due to momentum conservation v_1 is anti-symmetric around midrapidity. At relativistic energies it was found that the rapidity

dependence shows a typical S-shape curve and the slope at midrapidity was defined as *Flow*. However, at the present ultrarelativistic energies this shape has changed. The directed flow near midrapidity is much weaker and thus the slope is less steep. The data can be described by two superimposed Gaussians, which are anti-symmetric around midrapidity. The peak position and the maximum v_1 could be obtained by fitting the data with a Gaussian distribution. Thus, the description of the rapidity dependence of the directed flow by the slope near midrapidity is not sufficient. The superposition of two Gaussians is more generally applicable. It describes the complete rapidity range and has been proved to be also applicable to collisions at lower beam energies. In particular the typical S-shape curve can be reproduced by varying the peak position and the width of the Gaussian distributions. The parameters of the Gaussian distribution can be described as the contributions of spectators and participants to the directed flow signal. If the particles near midrapidity show a large directed flow signal the width of the Gaussian distribution is consequently large. In the studied 33 TeV Pb + Pb collisions, however, the width is smaller and the distributions are more separated than at relativistic energies, thus the particles near midrapidity exhibit only weak directed flow. While the superposition of the Gaussians could be applied to the proton and the pion rapidity distributions, the covered rapidity region is to small to prove this description for heavier fragments.

The strength of the elliptic flow by means of v_2 is consistent with zero at target rapidity. However, closer to midrapidity v_2 exhibits a clear signal. For positively charged pions this effect is of the order of $5\,\%$, the elliptic flow of protons increases to approximately $10\,\%$. Since the parameter v_2 is positive the direction of the elliptic flow is aligned with the directed flow, or in other words elliptic in-plane flow is observed. The tracking spectrometer arms in the WA98 experiment cover the midrapidity region and will provide a more complete picture of the elliptic flow component in this region.

Only a few years ago, it was believed that transverse flow would not exist at all at SPS energies, or if it did exist, be not large enough to measure. However, recent work including the present analysis has shown that not only the measurement is possible but that new and exciting results are being obtained. The difficult task to determine a reaction plane at SPS energies requires the precise particle measurement in the target or projectile fragmentation region. This thesis has shown that the Plastic Ball detector in the WA98 experiment is ideal to perform this measurement and to analyze azimuthal anisotropies. The very interesting observation of elliptic flow near midrapidity will become a topic in future investigations. Since the effect is weak and difficult to disentangle it is not yet resolved why pions show an in-plane and photons exhibit out-of-plane flow. This remains an open question and gives rise to further studies. Current models are only beginning to reasonably reproduce flow effects at AGS energies, and are still insufficient at SPS energies. New methods of measuring flow have been developed and recent insights into observables like elliptic flow have opened the opportunities for studying collective flow at SPS energies and beyond. Collective phenomena by means of directed and elliptic flow have been reexamined as a potential signal for a quark gluon plasma, and will be helpful in the understanding of the complex collision dynamics.

A. Kinematical Variables

The description of ultrarelativistic heavy ion collisions makes use of several kinematical variables. The definition of the most important ones used in this thesis are given here. The four-momentum is defined as:

$$p^{\mu} = \left(\frac{E}{c}, p_x, p_y, p_z\right) \tag{A.1}$$

The beam is considered to point into z-direction. Thus the transverse momentum p_T and the longitudinal momentum component $p_{\parallel}$ can be written as:

$$\begin{aligned} p_T &= p\sin\theta = \sqrt{p_x^2 + p_y^2} \\ p_{\parallel} &= p\cos\theta = p_z \end{aligned} \tag{A.2}$$

With the absolute magnitude of the momentum $p = \sqrt{p_x^2 + p_y^2 + p_z^2}$ and the polar angle θ relative to the beam axis.

The transverse momentum p_T is invariant under Lorentz transformation in z-direction, however, $p_{\parallel}$ is not invariant. Therefore the dimensionless rapidity is defined. It describes the velocity in z-direction and has the advantage to be additive under Lorentz transformation:

$$\begin{aligned} y &\equiv \frac{1}{2}\ln\left(\frac{E + p_{\parallel}}{E - p_{\parallel}}\right) \\ &= \text{atanh}\left(\frac{p_{\parallel}}{E}\right) \end{aligned} \tag{A.3}$$

The speed of light is defined as $c = 1$.

Experimentally, the determination of the rapidity might be difficult since it requires particle identification. For ultrarelativistic energies, i.e. for energies large compared to the rest mass of the particle, the rapidity turns into the so-called pseudorapidity η:

$$\begin{aligned} \eta &= -\ln\left(\frac{p + p_{\parallel}}{p - p_{\parallel}}\right) \\ &= -\ln\left(\tan\frac{\theta}{2}\right) \end{aligned} \tag{A.4}$$

For the particular case of mass-less photons the rapidity and pseudorapidity are equivalent.

B. Plastic Ball Mapping

In figure B.1 the Plastic Ball mapping is given. The arrangement for each detector module, represented by one triangle, is shown in the θ, ϕ - phase space. The two most forward rings $30^\circ \leq \theta \leq 50^\circ$ are used to reject downstream interactions. They correspond to the module numbers 576 to 655.

For the reaction plane determination the modules 1 to 520 are used, this corresponds to $160^\circ \leq \theta \leq 60^\circ$. The forward region is left out for the reaction plane determination because the high multiplicity does not allow a reasonable particle identification in these θ rings, the flow analysis, however, is based on identified particles.

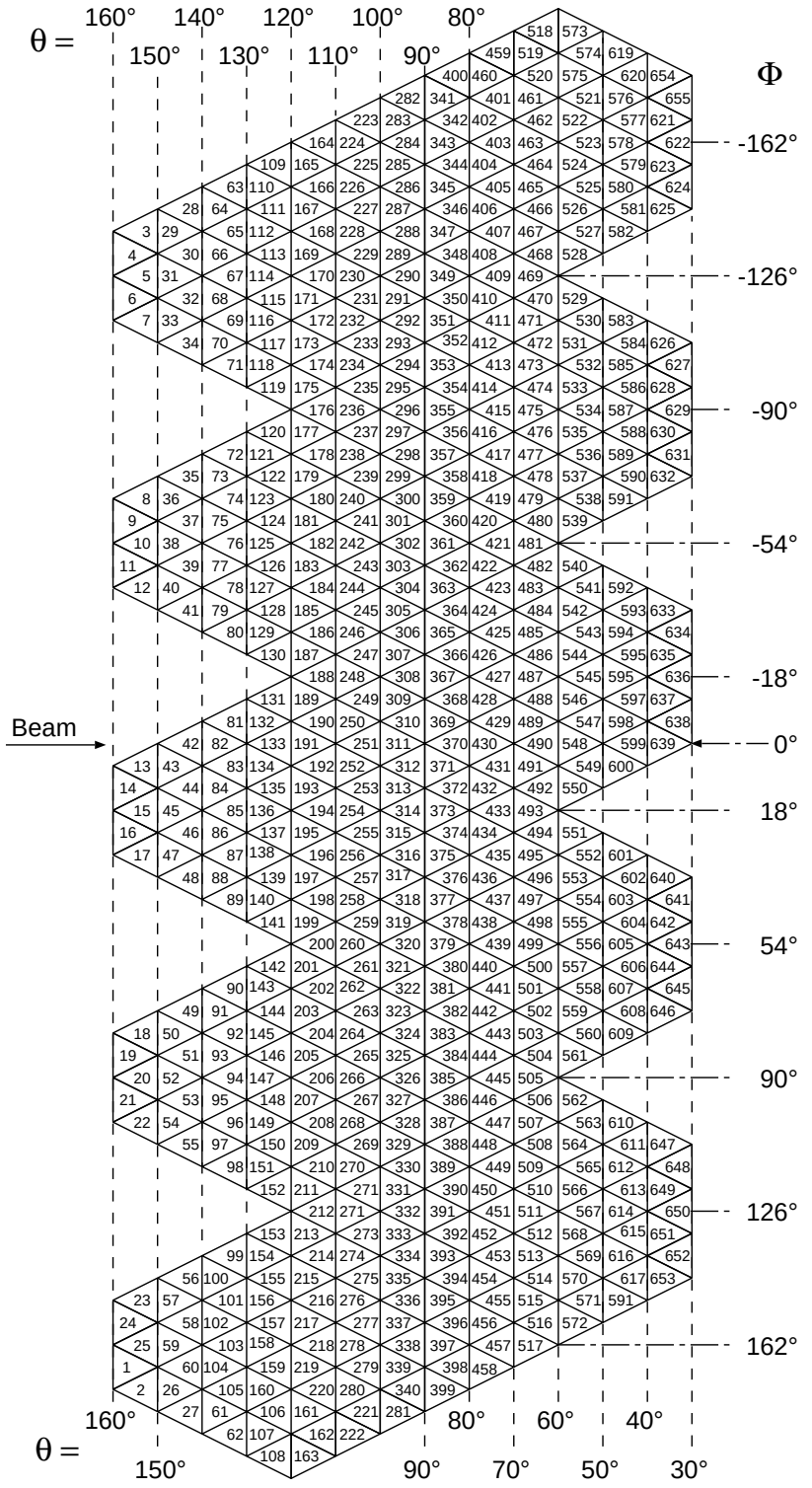

Figure B.1: The Plastic Ball mapping. For every module, represented by one triangle, the number, and the polar angle is given. The azimuthal angle Φ is only valid for $\Theta = 90°$.

C. Event Selection

To obtain a clean data set it is necessary to reject events where two beam particle hit the target in such a short time that the trigger cannot separate them into two single events. This can be done by studying the transverse energy E_T as a function of the forward energy E_{ZDC} (see section 3.1). In figure 3.1 the data shown have already been cleaned from such pile-up events. If a second beam particle traverses the target after a too short time difference, the ZDC measures the forward energy of both events.

In figure C.1 one can clearly see a band of pile-up events apart from the normal band, which can be selected by the cut:

$$25 - 0.08 \times (E_T/\text{GeV}) < (E_{ZDC}/\text{TeV}) < 45 - 0.07 \times (E_T/\text{GeV}) \tag{C.1}$$

If the beam particle does not interact with a target nucleus the transverse energy and the signals in forward modules of the Plastic Ball should be small. However, it might happen, that the beam particle interacts with material downstream of the target, the air, the detectors support structure, or the beam pipe. This will result in little or no signal in the Plastic Ball but the E_T will be comparable to a peripheral collision. To separate these events from true peripheral events a Plastic Ball cut is applied. Therefore the ADC sum s_f of the two most forward rings ($30^\circ \leq \theta \leq 50^\circ$ see figure B.1) is calculated and compared

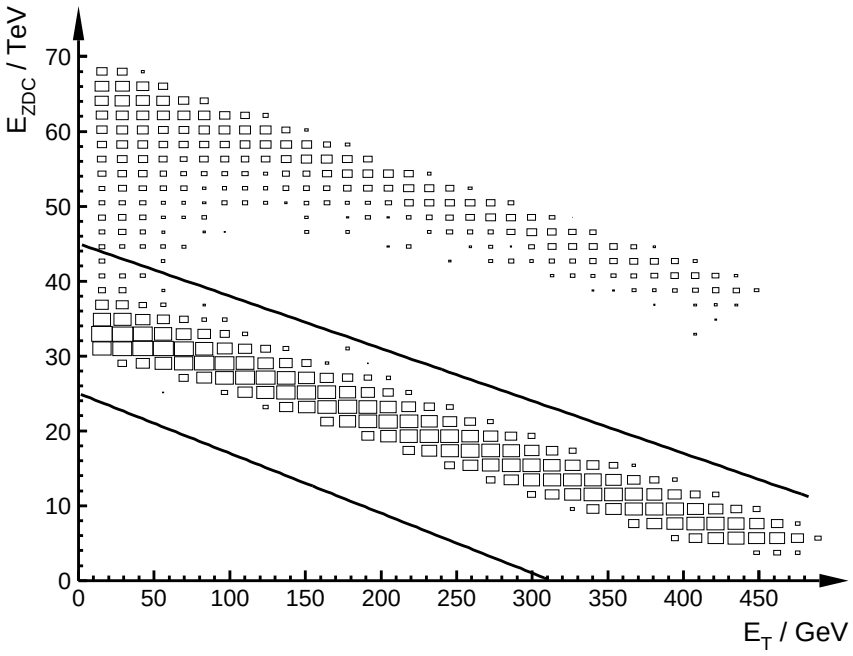

Figure C.1: The forward energy E_{ZDC} versus the transverse energy E_T. The solid lines correspond to the applied cut.

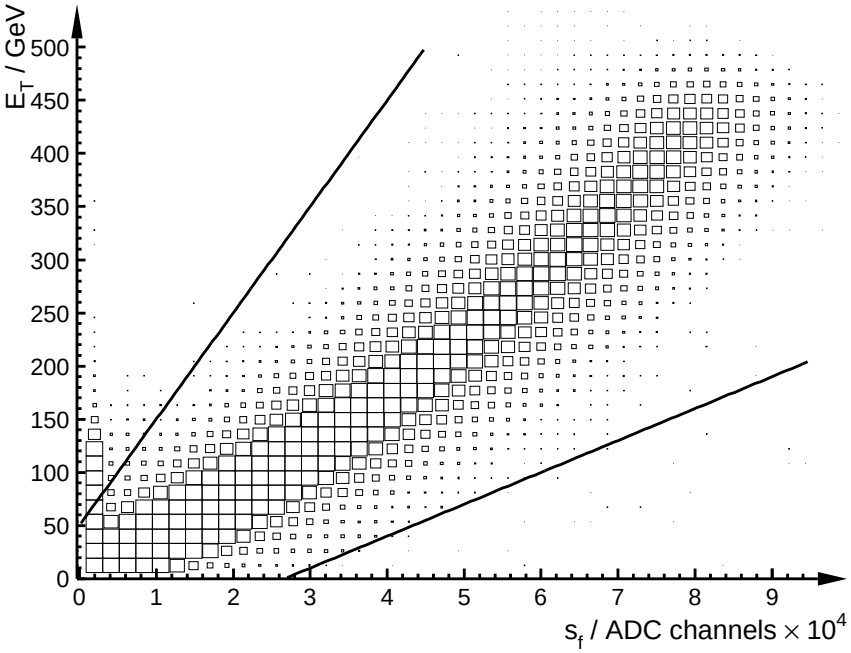

Figure C.2: The transverse energy E_T as function of s_f. The solid lines correspond to the applied cut.

with the transverse energy. In figure C.2 this comparison is studied and E_T is plotted versus s_f. The events with downstream interactions can be rejected by the following cut:

$$s_f = \sum_{i=576}^{655} ADC_i \tag{C.2}$$

$$-80 + 0.003 \times s_f < (E_T/\text{GeV}) < 50 + 0.010 \times s_f \tag{C.3}$$

D. Particle Identification

D.1 The Applied Cuts

particle	ξ_{min}	ξ_{max}	E_{min}	E_{max}
pions	-1.34	0.29	20 MeV	200 MeV
protons	0.44	1.05	40 MeV	240 MeV
deuterons	1.05	1.5	50 MeV	300 MeV
tritons	1.54	1.65	70 MeV	250 MeV

Table D.1: The cuts applied on the straightened ΔE - E distribution ξ (figure 3.5) to identify the given particle species. For the positively charged pions a TDC value $\geq 0.2\mu$s is additionally mandatory. The recommended energy range is given also.

D.2 Influence of cuts on $\langle p_x \rangle$

One physics observable in systematic flow studies is the average transverse momentum with respect to the reaction plane $\langle p_x \rangle$. See chapter 4.1 for the explanation of $\langle p_x \rangle$ as well as for the definition of the reaction plane. To check, whether this quantity is distorted by a background of misidentified Plastic Ball hits different strong cuts on the ξ distribution (figure 3.5) are tested. Table D.2 shows that within the errors there is no significant effect. For further details see appendix E.

cut width	$\langle p_x \rangle_{corr}$
1.0σ	24.75 ± 7.33MeV
1.5σ	28.18 ± 8.35MeV
2.0σ	27.70 ± 7.45MeV
3.0σ	34.25 ± 9.47MeV

Table D.2: The corrected average transverse momentum with respect to the reaction plane $\langle p_x \rangle_{corr}$ for different cuts on the ξ distribution (figure 3.5).

D.3 Linearization Method

Another method tested for straightening the ΔE-E plot is based on the analysis of the WA80 Plastic Ball data. Here the two dimensional distribution (figure 3.4) is projected onto the y-axis after straightening with

the following function:

$$\xi' = \frac{\sqrt{E^2 + \Delta E^2}}{R_a(\arctan(\Delta E/E))}$$

Where R_a is a fixed array of values only depending on the angle of every hit in the ΔE-E phase space. The projection ξ' is shown in figure D.1. The well defined peaks for π, p, d, and t hits are visible and a 3σ cut for protons is shown.

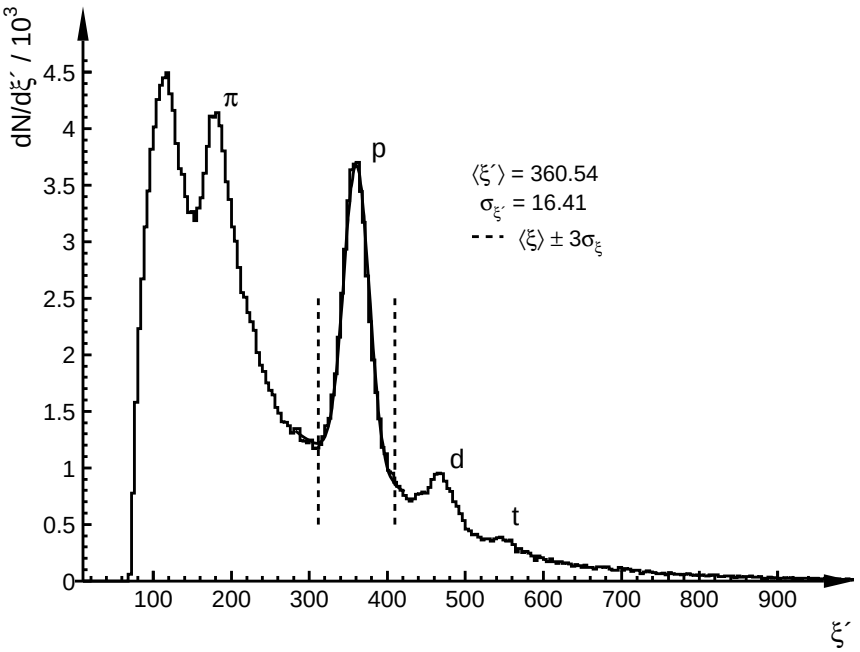

Figure D.1: The linearized ΔE-E distribution ξ'. Visible are the peaks for π, p, d, and t. The solid curve is a Gaussian fit on top of an exponential distribution. The dashed lines represent the proton cuts.

E. Background Contamination

If for example a pion-pion[1] double hit is misidentified as a proton this would affect the extracted proton flow strength since pions show an anti-flow behaviour. Thus it is important to check the possible contamination of the protons with non-protons. This has been taken into account by Monte Carlo simulations.

Input for this simulation are the parameterized rapidity, transverse momentum, and energy distributions of protons and pions. The distributions of the azimuthal and the polar angle are assumed to be flat. According to these distributions pions and protons are simulated and filtered through the Plastic Ball acceptance. The resulting $d^2N/dp_x dp_y$ distributions are like the measured ones (e.g. figure 5.2) except for the mean position which is zero, because there is no flow in the simulation.

Flow is introduced in the spectra by adding the typical transverse momentum transfer $\langle p_x \rangle$, i.e. $-30\,\mathrm{MeV}/c$ for protons and $+10\,\mathrm{MeV}/c$ for protons, to the simulated transverse momentum in the reaction plane. The simulated flow strength could be reproduced by a two dimensional Gaussian fit rather well. The systematic error turns out to be $\approx 11\,\%$.

Several possible contamination scenarios are considered and their influence on the extracted flow strength in terms of $\langle p_x \rangle$ is studied. If for example the protons are contaminated by $3\,\%$ pions then the simulated $d^2N/dp_x dp_y$ proton distribution is superimposed by the according pion distribution with a $3\,\%$ contribution. The possible contamination contributions are very small and all less than $5\,\%$, the considered scenarios are:

— not completely stopped protons

— not completely stopped deuterons

— misidentified neutrons

— punch through proton[2] on top of a proton

— punch through proton on top of a neutron

— punch through proton on top of a deuteron

— delta electron on top of a proton

— delta electron on top of a neutron

— delta electron on top of a deuteron

— proton-proton double hit

— proton-pion double hit

[1] By pion, the positively charged pion is meant, except for the case π^- is denoted in particular.

[2] Punch through protons are protons with high energy. They lose only a part of their energy when they traverse the Plastic Ball.

— pion-pion double hit

— pion-neutron double hit

— π^- on top of a proton

— π^- on top of a pion

The systematic error including these different contaminations turns out to be $8.5\,\%$. Thus in total the systematic error is less than $20\,\%$. Further studies will show whether this value might change for very central events, where the double hit probability increases.

F. Photon Flow Cross Checks

Since the collective flow of photons is a rather new field and the present result is apparently not yet understood there are several independent analyses in progress. One important cross check in the Fourier analysis of azimuthal particle correlations is to examine the collective flow perpendicular to the reaction plane.

Directed flow is by definition in-plane flow, thus in the perpendicular direction the directed flow must be zero. Such a coordinate transformation affects the elliptic flow differently. Elliptic flow out of the reaction plane looks naturally like in-plane flow in the plane perpendicular to the reaction plane. Thus the elliptic flow in terms of v_2 would change its sign.

The directed and elliptic flow perpendicular to the reaction plane has been studied by fitting equation F.1, which corresponds to a coordinate transformation of equation 6.6, to the azimuthal particle correlations like for example in figure 6.5.

$$\frac{1}{N}\frac{dN}{d\Delta\Phi} = 1 + 2v_1' \cos(\Delta\Phi + \frac{\pi}{2}) + 2v_2' \cos(2(\Delta\Phi + \frac{\pi}{2})) \tag{F.1}$$

It has been confirmed that the elliptic flow changes its sign under this transformation. The important question, however, is whether the directed flow vanishes. This is depicted in figure F.1. Shown is accordingly to figure 6.15 the strength of the directed flow for low p_T photons in dependence on centrality. The filled symbols represent the directed flow in the reaction plane. This is the same result as in the right panel of figure 6.15. The flow in the plane perpendicular to the reaction plane is given by the open symbols. Obviously the directed flow in this plane is consistent with zero. This indicates that the observed flow phenomena with respect to the reaction plane are apparently true effects, though it is still not completely understood.

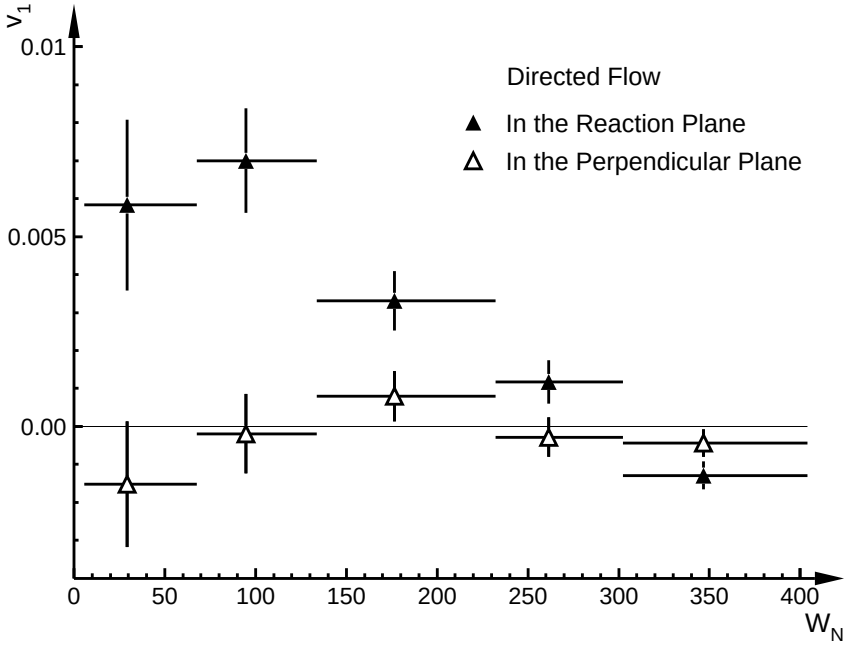

Figure F.1: The centrality dependence of the strength of the directed photon flow for $p_T < 400\,\mathrm{MeV}/c$. The filled symbols display the same result as in the right panel of figure 6.15 for the directed flow in the reaction plane. The open symbols represent the directed flow in the perpendicular plane obtained by equation F.1.

Bibliography

[Agg96] M. M. Aggarwal et al., Nucl. Instr. and Meth. **A 372** (1996) 143

[Agg97a] M. M. Aggarwal et al., Phys. Lett. **B 403** (1997) 390

[Agg97b] M. M. Aggarwal et al., *Systematics of Transverse Energy Production in Pb Induced Collisions at 158 GeV/nucleon*, UT/ORNL WA98 Preprint, 1997

[Agg98a] M. M. Aggarwal et al., Phys. Lett. **B 420** (1998) 169

[Agg98b] M. M. Aggarwal et al., *Directed Flow in 158 $AGeV$ ^{208}Pb + ^{208}Pb Collisions*, 1998, submitted to Phys. Rev. Lett.

[Agg98c] M. M. Aggarwal et al., *A Preshower Photon Multiplicity Detector for the WA98 Experiment*, 1997, submitted to Nucl. Instr. and Meth.

[Agg98d] M. M. Aggarwal et al., Phys. Rev. Lett. **81** (1998) 4087

[Agg98e] M. M. Aggarwal et al., *Freeze-Out Parameters in Central 158 $AGeV$ ^{208}Pb + ^{208}Pb Collisions*, CERN WA98 preprint, 1998

[Agg98f] M. M. Aggarwal et al., *Direct Photon Production in 158 $AGeV$ ^{208}Pb + ^{208}Pb Collisions*, CERN WA98 preprint, 1998

[Ahl98] L. Ahle et al., Phys. Rev. **C 57** (1998) 1416

[Ala92] J. P. Alard et al., Phys. Rev. Lett. **69** (1992) 890

[Alb87] R. Albrecht et al., Phys. Lett. **B 199** (1987) 297

[Alb91] R. Albrecht et al., Z. Phys. **C 51** (1991) 1

[Alb98] R. Albrecht et al., Eur. Phys. Jour. **C 5** (1998) 255

[All91] G. T. Alley et al., *Proposal to Construct Monolithic Readout Electronics for a 10,000 Element Lead-Glass Detector*, UT/ORNL WA98 Preprint, 1991

[App98] H. Appelshäuser et al., Phys. Rev. Lett. **80** (1998) 4136

[Awe89] T. C. Awes et al., Nucl. Instr. and Meth. **A 279** (1989) 479

[Awe93] T. C. Awes et al., *Monte Carlo Simulation of WA98 Calorimeter Performance*, WA98 Internal Report, UT/ORNL, Oak Ridge, 1993

[Awe95] T. C. Awes et al., Z. Phys. **C 69** (1995) 67

[Awe96] T. C. Awes et al., Phys. Rev. Lett. **B 381** (1996) 29

[Awe97] T. C. Awes et al., Nucl. Phys. **A 630** (1997) 499c

[Bad82] A. Baden et al., Nucl. Instr. and Meth. **203** (1982) 189

[Bar94] J. Barrette et al., Phys. Rev. Lett. **73** (1994) 2532

[Bar96] R. M. Barnett et al., Phys. Rev. **D 54** (1996) 1

[Bar97a] J. Barrette et al., Phys. Rev. **C 55** (1997) 1420

[Bar97b] J. Barrette et al., Phys. Rev. **C 56** (1997) 3254

[Bar98a] C. Barlag et al., Nucl. Instr. and Meth. **A 406** (1998) 299

[Bar98b] J. Barrette et al., *Directed Flow of Light Nuclei in Au + Au Collisions at AGS Energies*, preprint nucl-ex/9805006 (1998)

[Bas95] S. A. Bass et al., Phys. Rev. **C 51** (1995) 3343

[Bas98] S. A. Bass et al., *Signatures of Quark-Gluon-Plasma formation in high energy heavy-ion collisions: A critical review*, preprint hep-ph/9810281 (1998)

[Bat97] S. Bathe, *Untersuchungen zur Nachweiswahrscheinlichkeit eines Sreamer-Tube-Detektors*, diploma thesis, Universität Münster, 1997

[Bec87] P. Beckmann et al., Mod. Phys. Lett. **A 2** (1987) 163

[Ber92] F. Berger et al., Nucl. Instr. and Meth. **A 321** (1992) 152

[Boc88] R. Bock et al., Mod. Phys. Lett. **A 3** (1988) 237

[Bjø83] J. D. Bjørken, Phys. Rev. **D 27** (1983) 140

[Bjø92] J. D. Bjørken, Acta Phys. Pol. **B 23** (1992) 637

[Boh96] E. M. Bohne, *Einsatz eines Bleiglasdetektors zur Untersuchung der Produktion neutraler Pionen in ultrarelativistischen bleiinduzierten Schwerionenreaktionen*, doctoral thesis, Universität Münster, 1996

[Blu93] C. Blume, *Proton-Proton-Korrelationen in ultrarelativistischen Schwerionenreaktionen*, diploma thesis, Universität Münster, 1993

[Blu98] C. Blume, *Produktion neutraler Mesonen in heißer hadronischer Materie*, doctoral thesis, Universität Münster, 1998

[Bra98] P. Braun-Munzinger, in *Physics and Astrophysics of Quark-Gluon Plasma*, Narosa Publishing House, New Dehli, 1998

[Buc99] D. Bucher, doctoral thesis, Universität Münster, 1999, in preparation

[Büs97] H. Büsching, *Untersuchung nichtlinearer Effekte im Bleiglaskalorimeter LEDA - Eine Computersimulation* - , diploma thesis, Universität Münster, 1997

[Car98a] L. Carlén et al., Nucl. Instr. and Meth. **A 412** (1998) 361

[Car98b] L. Carlén et al., Nucl. Instr. and Meth. **A 413** (1998) 92

[Čer37] P. A. Čerenkov, Phys. Rev. **52** (1937) 378

[Cha97] J. Chance et al., Phys. Rev. Lett. **78** (1997) 2535

[Chu96] T. Chujo et al., Nucl. Instr. and Meth. **A 383** (1996) 409

[Cla96] A. Claussen, *Einsatz des Bleiglaskalorimeters LEDA zur Untersuchung ultrarelativistischer blei-induzierter Schwerionenreaktionen in Hinblick auf die Produktion inklusiver Photonen*, doctoral thesis, Universität Münster, 1996

[Cle93] G. Clewing, *Untersuchungen zur Produktion direkter Photonen in ultrarelativistischen Schwerionenreaktionen bei 200 AGeV*, doctoral thesis, Universität Münster, 1993

[Cro97] P. Crochet et al., Nucl. Phys. **A 627** (1997) 522

[Cse94] L. P. Csernai, *Introduction to Relativistic Heavy Ion Collisions*, John Wiley & Sons Ltd., Chichester, 1994

[Cug82] J. Cugnon et al., Phys. Lett. **B 109** (1982) 167

[Dan85] P. Danielewicz and G. Odyniec, Phys. Lett. **B 157** (1985) 146

[Dan98] P. Danielewicz et al., Phys. Rev. Lett. **81** (1998) 2438

[Dos87] K. G. R. Doss et al., Phys. Rev. Lett. **59** (1987) 2720

[Eno97] K. Enosawa et al., *Front-End Electronics of PHENIX Time-of-Flight System*, Poster on Quark Matter, Tsukuba, 1997

[Eno98] K. Enosawa, private communication, 1998

[Fab87] C. W. Fabjan, *Experimental Techniques in High Energy Physics*, Addison-Wesley Publishing Co., Menlo Park, 1987

[Fai87] G. Fai at al., Phys. Rev. **C 36** (1987) 597

[Fei76] E. L. Feinberg, Nuovo Cim. **A 34** (1976) 391

[Fey61] R. P. Feynmann, *Quantum Electrodynamics*, Benjamin Publishing Co., London, 1961

[Fil96] P. Filip, *Transversal Flow of Pions as a Consequence of Rescattering Process*, preprint hep-ex/9605001 (1996)

[Fra95] J. R. Fransens, *Pad readout project version 2*, Internal Report, Groningen, 1995

[Gav94] S. Gavin, Nucl. Phys. **A 566** (1994) 383c

[Gel73] M. Gell-Mann and H. Fritzsch, in proceedings of XI International Conference on High Energy Physics, Chicago, 1973

[Geu98] F. J. M. Geurts, *Neutral Meson Production in Hot Matter*, doctoral thesis, Universiteit Utrecht, 1998

[Gla70] R. J. Glauber and G. Matthiae, Nucl. Phys. **B 21** (1970) 135

[Gus84] H. Å. Gustafsson et al., Phys. Rev. Lett. **52** (1984) 1590

[Gus88] H. Å. Gustafsson et al., Mod. Phys. Lett. **A 3** (1988) 1323

[Gut89a] H. H. Gutbrod et al., Phys. Lett. **B 216** (1989) 267

[Gut89b] H. H. Gutbrod et al., Rep. Prog. Phys. **52** (1989) 1267

[Gut90] H. H. Gutbrod et al., Phys. Rev. **C 42** (1990) 640

[Gyu82] M. Gyulassy et al., Phys. Lett. **B 110** (1982) 185

[Han54] R. Hanbury-Braun and R. Q. Twiss, Philos. Mag. **45** (1954) 633

[Har96] J. W. Harris and B. Müller, Ann.Rev.Nucl.Part.Sci. **46** (1996) 71

[Hem96] T. K. Hemmick, Nucl. Phys. **A 610** (1996) 63c

[Hee96] W. H. van Heeringen, *Anisotropy in Ultra-Relativistic Heavy-Ion Collisions*, doctoral thesis, Universiteit Utrecht, 1996

[Her96] N. Herrmann et al., Nucl. Phys. **A 610** (1996)

[Hil96] K. D. Hildenbrand et al., Acta Phys. Pol. **B27** (1996) 243

[Hof76] J. Hoffman et al., Phys. Rev. Lett. **36** (1976) 88

[Höl93] G. Hölker, *Produktion inklusiver Photonen und neutraler Pionen in ultrarelativistischen Schwerionenreaktionen*, doctoral thesis, Universität Münster, 1993

[Höl95] G. Hölker, *Extraction of the π^0 Peak Content*, WA80 internal report, Universität Münster, 1995

[Hua97] I. Huang, *Global and Collective Phenomena in Pb + Pb Collisions at Projectile Energy of 158 GeV/nucleon*, doctoral thesis, University of California, Davis, 1997

[Hub92] L. Hubbeling, *Large Photomultiplier Systems - A New Approach*, CERN/ECP 92-10, CERN, Genève, 1992

[Hub93] L. Hubbeling, *HIVOC, A VME High Voltage Control Card for Large Photomultiplioer Systems*, CERN/ECP 93-2, CERN, Genève, 1993

[Idh93] J.Idh and E.Stenlund, *Concerning the optimal positioning of the MIRAC calorimeters in the WA98 experimental setup*, WA98 Internal Report, Memo 930415, Lund, 1993

[Iży91] M. Iżycki et al., Nucl. Instr. and Meth. **A 310** (1991) 98

[Iży94] M. Iżycki et al., Nucl. Phys. **A 566** (1994) 605c

[Jah94] A. Jahns et al., Phys. Rev. Lett **72** (1994) 3464

[Jel58] J .V. Jelly, *Cerenkov Radiation*, Pergamon Press, London, 1958

[Kam86] K. H. Kampert, *Kollektive Phänomene in relativistischen Schwerionenreaktionen*, doctoral thesis, Universität Münster, 1986

[Kam89] K. H. Kampert, J. Phys. **G15** (1989) 691

[Kam93] K. H. Kampert, *Hochenergetische Schwerionenreaktionen – Studium heißer dichter Kernmaterie*, Habilitationsschrift, Universität Münster, 1993

[Kap79] J. I. Kapusta, Nucl. Phys. **B 148** (1979) 461

[Kap93] J. I. Kapusta et al., Phys. Rev. **D 47** (1993) 4171

[Kin97] J. C. Kintner et al., Phys. Rev. Lett. **78** (1997) 4165

[Kiy97] A. Kiyomichi et al., *PHENIX Time-of-Flight System*, Poster on Quark Matter, Tsukuba, 1997

[Kle92] K. Kleinknecht, *Detektoren für Teilchenstrahlung*, Teubner Studienbücher, Stuttgart, 1992

[Kur96] M. Kurata and S. Nishiumura, *Analysis of Russian TOF data '95*, WA98 Internal Report, Tsukuba, 1996

[Kur98] M. Kurata et al., in *Physics and Astrophysics of Quark-Gluon Plasma*, Narosa Publishing House, New Dehli, 1998

[Lae96] E. Laermann, Nucl. Phys. **A 610** (1996) 1c

[Lat80] C. M. G. Lattes et al., Phys. Rep. **65** (1980) 151

[Leo87] W. R. Leo, *Techniques for Nuclear and Particle Physics Experiments*, Springer-Verlag, Berlin, 1987

[Lee94] Y. Y. Lee, *Trigger System for WA98*, WA98/94-01 Internal Report, Genève, 1994

[Li 94] B. A. Li et al., Nucl. Phys. **A 570** (1994) 797

[Lie91] R. Lietava, Z. Phys. **C 49** (1991) 546

[Lin97] W. Lin et al., Nucl. Instr. and Meth. **A 389** (1997) 415

[Lis94] T. Lister, *Azimutale Korrelationen von Pionen im Targetfragmentationsbereich ultrarelativistischer Kernreaktionen* , diploma thesis, Universität Münster, 1994

[Liu98] H. Liu et al., Nucl. Phys. **A 630** (1998) 549c

[McL85] L. D. McLerran and T. Toimela, Phys. Rev. **D 31** (1985) 545

[Mat86] T. Matsui and H. Satz, Phys. Lett. **B 178** (1986) 416

[Mor98] D. P. Morrison et al., *The PHENIX Experiment at RHIC*, preprint hep-ex/9804004 (1998)

[Nie94] G. J. van Nieuwenhuizen et al., *Proposal for the Mechanical Design of Two Si-Drift Detectors for the WA98 Experiment*, WA98 Internal Report, Groningen, 1994

[Neu95] S. Neumaier et al., Nucl. Instr. and Meth. **A 360** (1995) 593

[Nis97] S. Nishimura et al., Nucl. Phys. **A 638** (1998) 459c

[Oll92] J. Y. Ollitrault, Phys. Rev. **D 46** (1992) 229

[Oll93] J. Y. Ollitrault, Phys. Rev. **D 48** (1993) 1132

[Oll95] J. Y. Ollitrault, Nucl. Phys. **A 590** (1995) 561c

[Oll97] J. Y. Ollitrault, *Reconstructing Azimuthal Distributions in Nucleus-Nucleus Collisions*, preprint nucl-ex/9711003 (1997)

[Oll98] J. Y. Ollitrault, Nucl. Phys. **A 638** (1998) 195c

[Par95] M. D. Partlan et al., Phys. Rev. Lett. **75** (1995) 2100

[PHE93] PHENIX-Collaboration, *PHENIX Conceptual Design Report*, Brookhaven National Laboratory, 1993

[Pei96] T. Peitzmann et al., Nucl. Instr. and Meth. **A 376** (1996) 368

[Pei97] T. Peitzmann, *Kernmaterie unter extremen Bedingungen - Die experimentelle Suche nach dem Quark-Gluon-Plasma* -, Habilitationsschrift, Universität Münster, 1997

[Pei98] T. Peitzmann et al., *private communication*, 1998

[Per87] D. H. Perkins, *Introduction to High Energy Physics*, Addison-Wesley Publishing Co., Menlo Park, 1987

[Pos98] A. M. Poskanzer and S. A. Voloshin, *Methods for analyzing anisotropic flow in relativistic nuclear collisions*, preprint nucl-ex/9805001 (1998)

[Pra86] S. Pratt, Phys. Rev. **D 33** (1986) 1314

[Qui83] C.Quigg, *Gauge Theories of the Strong, Weak, and Electromagnetic Interactions*, Benjamin Cummings Publishing Co., London, 1983

[Raf82] J. Rafelski and B. Müller, Phys. Rev. Lett. **48** (1982) 1066

[Ras96] A. Rashevskii et al., Nuovo Cim. **A 109** (1996) 1261

[Reh90] P. Rehak and E. Gatti, Nucl. Instr. and Meth. **A 289** (1990) 410

[Rei97] W. Reisdorf and H. G. Ritter, Ann. Rev. Nucl. Part. Sci. **47** (1997) 663

[Rei98] W. Reisdorf, Nucl. Phys. **A 630** (1998) 15c

[Rey95] K. Reygers, *Aufbau eines Streamer-Tube Detektors mit Pad-Auslese durch einen integrierten Schaltkreis*, diploma thesis, Universität Münster, 1995

[Rey99] K. Reygers, doctoral thesis, Universität Münster, 1999, in preparation

[Ris95] D. H. Rischke et al., *The Phase Transition to the Quark-Gluon Plasma and Its Effect on Hydrodynamic Flow*, preprint nucl-th/9505014 (1995)

[Ris96] D. H. Rischke, Nucl. Phys. **A 610** (1996) 88c

[Rub95] J. M. Rubio et al., Nucl. Instr. and Meth. **A 367** (1995) 358

[Sat98] H. Satz, in *Physics and Astrophysics of Quark-Gluon Plasma*, Narosa Publishing House, New Dehli, 1998

[Sch68] W. Scheid et al., Phys. Rev. Lett. **21** (1968) 1479

[Sch69] W. Scheid and W. Greiner, Z. Phys. **226** (1969) 365

[Sch93] E. Schnedermann et al., Phys. Rev. **C 48** (1993) 2462

[Sch94a] G. Schepers, *Entwicklung und Erprobung eines LED-gestützten Monitorsystems für ein modulares Bleiglasspektrometer*, diploma thesis, Universität Münster, 1994

[Sch94b] H. Schlagheck, *Konstruktion und Kalibration eines Bleiglaskalorimeters für ultrarelativistische Schwerionenreaktionen* , diploma thesis, Universität Münster, 1994

[Shu95] E. V. Shuryak, Z. Phys. **C 38** (1988) 141

[Sol92] N. Solomey, *Development and Utilization of a Light Chamber Tracking System in a Heavy Ion Experiment Performing two Pion Interferometry*, doctoral thesis, Université de Genève, 1992

[Sor90] H. Sorge et al., Phys. Lett. **B 243** (1990) 7

[Sor95] H. Sorge et al., Phys. Rev. **C 52** (1995) 3291

[Sri92] D. K. Srivastava et al., Phys. Lett. **B 276** (1992) 285

[Ste94] P. Steinhaeuser, *Der Siliziumdriftdetektor im WA93-Experiment*, doctoral thesis, Universität Frankfurt am Main, 1994

[Ste98] P. Steinberg, *Search for Disoriented Chiral Condensates in 158 AGeV ^{208}Pb + ^{208}Pb Collisions*, doctoral thesis, Massachusetts Institute of Technology, 1998

[Sto86] H. Stöcker and W. Greiner, Phys. Rep. **137** (1986) 277

[Stü99] D. Stüken, doctoral thesis, Universität Münster, 1999, in preparation

[Tsa93] M. B. Tsang et al., Phys. Rev. **C 47** (1993) 2717

[Vod93a] A. S. Vodopianov, *ZDC Status Report*, WA98 Internal Report, GSI, Darmstadt, 1993

[Vod93b] A. S. Vodopianov, *TOF Status Report*, WA98 Internal Report, GSI, Darmstadt, 1993

[Vol96] S. Voloshin and Y. Zhang, Z. Phys. **C 70** (1996) 665

[WA98a] WA98 Collaboration, *Proposal for a large Acceptance Hadron and Photon Spectrometer*, CERN/SPSLC 91-17, SPSLC/P260, CERN, Genève, 1991

[WA98b] WA98 Collaboration, *Status Report on P260*, WA98 Internal Report, CERN, Genève, 1992

[WA98c] WA98 Collaboration, *Status Report for WA98*, CERN/SPSLC 94-32, SPSLC/M539, CERN, Genève, 1994

[WA98d] WA98 Collaboration, *Physics Capabilities and Considerations for Experiment WA98*, WA98 Internal Report, CERN, Genève, 1995

[Wer93] K. Werner, Phys. Rep. **232** (1993) 87

[Wie96] T. Wienold et al., Nucl. Phys. **A 610** (1996) 76c

[Wil92] W. K. Wilson et al., Phys. Rev. **C 45** (1992) 738

[Won94] C. Y. Wong, *Introduction to High-Energy Heavy-Ion Collisions*, World Scientific Publishing Co., Singapore, 1994

[Woo98] L. S. Wood, *Transverse flow in 158 AGeV/c Pb + Pb at the CERN SPS*, doctoral thesis, University of California, Davis, 1998

[Wys98] B. Wysłouch et al., Nucl. Phys. **A 638** (1998) 147c

[You94] G. R. Young et al., *Monolitic circuits for Lead-Glass Calorimetry*, in proceedings of Electronics for Future Colliders Conference, Montevale, 1994

[Zha95] Y. Zhang et al., Nucl. Phys. **A 590** (1995) 557c

Acknowledgements

I am indebted to many people for having been able to write this thesis, and I would like to express my gratitude to all of them. In particular I wish to thank:

My supervisor, Professor Dr. R. Santo, for his constant support and the outstandingly good working conditions at the Institut für Kernphysik. Also for the opportunity to write my thesis within an international collaboration. And for making the research sojourns at CERN, and ORNL as well as the participation in international conferences possible.

Dr. T. Peitzmann for his open door, his ideas, his constructive criticism, and many discussions about collective flow phenomena and the difficulties to determine and describe them.

Dr. T. C. Awes for his enormous efforts for the WA98 collaboration, especially as driving force in getting the papers published and for his patient co-ordination of the different movements in the flow related analysis.

The present and former members of the Münster WA98 crew, C. Barlag, S. Bathe, E. M. Bohne, Z. Böröcz, D. Bucher, H. Büsching, A. Claussen, U. Denningmann, N. Heine, K. H. Kampert, S. Kees, T. Krümpel, G. Schepers, D. Stüken, W. Verhoeven, and in particular C. Blume, T. Lister, and K. Reygers for their help at various stages of research and writing.

R. Glasow, M. Purschke, P. Stankus, P. Steinberg, Y. Schutz, and S. Nishimura for the computer power in Münster, at CERN, at ORNL, at MIT, in Lyon, and in Tsukuba, without, this thesis had been inconceivable.

All remaining collaborators in WA98 for their help and their efforts for the experiment. In particular H. H. Gutbrod, H. Kalechofsky, M. Kurata, D. Morrison, T. K. Nayak, S. Neumaier, F. Plasil, A. Przybyla, and G. R. Young.

T. C. Awes, C. Blume, T. Peitzmann, and K. Reygers I wish to thank for carefully reading the manuscript.

The Deutscher Akademischer Austauschdienst, DAAD, for partial financial support of the abroad research studies.

Finally, my parents and my extended 'family' Bernhard, Sandra, Michael, Franz, Ullrich, Heiko, Stefan, Ulrike, Sabine, Thomas, Melanie, Julia, and Heike for their lasting love, support and patience.

Curriculum Vitae

General:

Name:	Hubertus Schlagheck
Date of birth:	2 January 1969 in Seppenrade
Marital Status:	Unmarried

Education:

1975 – 1979	Mariengrundschule in Seppenrade
1979 – 1988	St.Antonius Gymnasium in Lüdinghausen
10.06.1988	Abitur
1988 – 1994	Westfälischen Wilhelms–Universität Münster
04.06.1994	Diploma in Physics
7/94 – present	PhD. Student in Physics
	Institut für Kernphysik
	Supervisor Prof. Dr. R. Santo

Employment:

7/91 – 6/94	Staff member of the Germanistische Institut of
	the Westfälischen Wilhelms–Universität Münster
7/94 – present	Research employee of the Institut für Kernphysik of
	the Westfälischen Wilhelms–Universität Münster
1995	Scholarship of the Deutscher Akademischer
	Austauschdienst DAAD, program HSP II/AUFE